Investigating climate dynamics in CA: A multi-proxy approach to stalagmite paleoclimate reconstruction

By

BARBARA ELAINE WORTHAM
DISSERTATION

Submitted in partial satisfaction of the requirements for the degree of

DOCTOR OF PHILOSOPHY
in

EARTH AND PLANETARY SCIENCES

in the

OFFICE OF GRADUATE STUDIES

of the

UNIVERSITY OF CALIFORNIA

DAVIS

Approved:

Isabel P. Montañez, Chair

Sujoy Mukhopadhyay

Kari Cooper

Monica Arienzo

Committee in Charge

2021

Acknowledgements

I would like to thank my advisor, Isabel Montañez, for being a role model and a wonderful advisor. I would also like to thank my committee, especially Sujoy Mukhopadhyay who went above and beyond in his duties to me as a student. To my friends and family, this couldn't have happened without you being there to keep me sane. A big thank you to my husband, Chad Trexler, and our dog, Kit, for making this whole journey enjoyable. This dissertation is dedicated to the loving memory of my grandfather, John Provine, he was my inspiration to be in graduate school, my northern star, and my moral compass.

Abstract

Stalagmite records of stable isotope ($\delta^{18}O_{cc}$) variability from across the Southwestern United States change in-step with Northern Hemisphere temperature over the last deglaciation. The interpretations of $\delta^{18}O_{cc}$ records, however, is complicated due to the multiple influences on $\delta^{18}O_{cc}$. These influences include seasonality of precipitation, regional temperature change, and variability in precipitation source, among others. To isolate the influence of temperature in $\delta^{18}O_{cc}$ records, we must develop quantitative and independent records of temperature. Here, I use a multi-proxy approach in a previously studied stalagmite, ML-1, from western Sierra Nevada. We employ high-resolution 3-dimensional neutron computed tomography and x-ray computed tomography to map fluid inclusion distribution in the stalagmite. Water-rich regions in ML-1 occur contemporaneously with the lowest values of $\delta^{18}O_{cc}$. We also use ML-1 fluid inclusions to determine a noble gas temperature for the Last Glacial Maximum (18.8 ± 0.3 ka), indicating a 5.2 ± 1.7 (2σ) °C cooling relative to today. Noble gas concentrations were measured using a progressive step-crushing technique originally developed for understanding noble gas abundances in basalt. The progressive step-crushing technique and a robust water calibration reduces uncertainty in the resulting NGT relative to previous studies that utilize pre-crushing techniques. The temperature from the Last Glacial Maximum is used to correct for temperature variability in $\delta^{18}O_{cc}$. Variability in $\delta^{18}O_{cc}$ is ~2.0 ‰ on the centennial scale originally interpreted to reflect temperature and precipitation source shifts. Finally, a record of 45 stable isotope measurements from the stalagmite fluid inclusions reveal periods of increased kinetic fractionation at 18, 15.2, and 13.2 ka. The results of the stable isotope analysis reveal that these periods are times of lower effective moisture locally. The combined results from these three approaches illustrate that, in the western Sierra Nevada, temperature variability only accounts for a fraction of total $\delta^{18}O_{cc}$ changes

on the centennial scale and points to variability in precipitation source region and effective moisture as major influences on stalagmite paleoclimate records. Additionally, I conclude that the central Sierra Nevada is sensitive to changing precipitation dynamics in the western U.S. that are teleconnected to circulation and temperature variability in the Pacific and the Atlantic.

Dissertation Introduction

The southwestern U.S. is one of the world's most climatically sensitive regions as it is drought-prone, characterized by highly seasonal precipitation, and subject to large-magnitude climate modulation over a range of time-scales (Barnett et al., 2008; Seager et al., 2013; Griffin and Anchukaitis, 2014). Climate variability in this region is a major influence on water resources and ecosystems (Seager and Vecchi, 2010; Cook et al., 2011). The 2015-2016 protracted drought throughout much of this region highlights this vulnerability including the sustainability of future water resources and ecologic wealth (Hatchett et al., 2015). Notably, climate models predict that with rising atmospheric pCO_2 and warming, poleward expansion of the subtropical dry zones and large-scale shifts in mid-latitude winter storm tracks will cause much of the western U.S. to become increasingly drier with large changes in precipitation patterns (Sewall and Sloan, 2004; Salathe, 2006; Seager et al., 2007, 2015; Barnett et al., 2008; Seager and Vecchi, 2010; Chiang and Friedman, 2012; Swain et al., 2014). The Sierra Nevada is centrally located in this region of projected drying. Despite the record rainfall of winter 2016-2017, the severity of this prediction is reflected in recent Sierra snowpack levels that were the lowest of the past 500 years (Belmecheri et al., 2015). A necessary component of robust predictions of future hydroclimate in this region is a refined understanding of how the dynamics that drive natural climate variability evolve over longer time scales including under past warm periods and changing pCO_2 (Dettinger et al., 1998; Cook et al., 2011; Seager and Vecchi, 2010). A period of changing pCO_2 and temperature has occurred in the recent past, termed the last deglaciation (20-11 ka) and provides a natural experiment to better understand how the southwestern U.S. will respond to future climate change.

Speleothems, or cave calcite deposits, have traditionally been used to gain an

understanding of how terrestrial systems have been impacted locally and regionally by global climate changes (McDermott, 2004; Wong and Breecker, 2015). Speleothems exhibit high temporal resolution and are often continuously deposited (Richards and Dorale, 2003). Additionally, the calcite in speleothems archives the chemical variability in $\delta^{18}O$, $\delta^{13}C$, U-series isotopes, and trace elements making speleothems easy to date with climatically interpretable chemical variability (Kaufman, 2003; McDermott, 2004; Wong and Breecker, 2015; Cheng et al., 2019).

The stable isotope values in speleothems, however, are influenced by multiple processes (McDermott, 2004; Lachniet, 2009). In the southwestern U.S., speleothem $\delta^{18}O$ values have been interpreted to reflect changing temperature, precipitation source (high latitude vs. low latitude Pacific sources mainly) (Oster et al., 2012; 2014; 2015), changing seasonality of precipitation (Asmerom et al., 2010; Wagner et al., 2010), and changing precipitation amount (Feng et al., 2014). The potential of multiple processes limits the ability of speleothem $\delta^{18}O$ to provide quantitative information on local and regional climate. Further, disequilibrium fractionation between speleothem $\delta^{18}O$ and water $\delta^{18}O$ occurs when there is rapid CO2 degassing in caves and/or low humidity (Mickler et al., 2004), both of which are observed when there is variability in vegetation, temperature, and precipitation amount (Banner et al., 2007; Wong et al., 2010; 2011; Oster et al., 2012). This suggests that disequilibrium fractionation, when observed, could additionally be used as a climatic indicator, but it is often difficult to observe it.

In this dissertation, I address these challenges by developing new methods to understand the isotopic and elemental variability of waters that are trapped in the calcite structure of a stalagmite from the central Sierra Nevada. These waters are often referred to as "included" waters or fluids (herein referred to as fluid inclusions; Meckler et al., 2015). The stalagmite, ML-

1, was previously studied and the stalagmite $\delta^{18}O$ values, as well as stalagmite $\delta^{13}C$, ages, and trace elements were already published (Oster et al., 2015).

In chapter 1, I develop a novel method to map the fluid inclusion density in stalagmite ML-1. I use a combination of x-ray and neutron computed tomography to develop 3-dimensional maps of where fluids were trapped along stalagmite growth layers. Additionally, this method reveals where they were trapped in large quantities in stalagmite macro-voids (Wortham et al., 2019). Further, I created a record of the stalagmite petrography in ML-1. I correlated the fluid inclusion distribution and petrography with the previously studied isotopic and elemental variability in the calcite of stalagmite ML-1. The primary finding of this chapter is that the distribution of fluid inclusions may be a proxy for water excess, as fluid inclusion distribution is correlated with stalagmite $\delta^{18}O$.

In chapter 2, I adapt a progressive step-crushing method for calculating the noble gas temperatures from stalagmite fluid inclusions and apply this method to a sub-sample from ML-1 (Wortham et al., in revision). In this chapter, I apply previously developed methods for multi-step-crushing sub-samples to stalagmite samples. I use the methodology of Parai et al. (2019) and develop a new stalagmite crushing line for use on a Nu Noblesse Mass Spectrometer. We use the abundances of Kr, Xe, and Ar from a sub-sample that is 18.8 ka in stalagmite ML-1 to calculate a noble gas temperature. The primary finding from this chapter is that the central Sierra Nevada was 7.1 ± 1.7 °C cooler at 18.8 ka than it is today.

In chapter 3, I adapt a previously published method (Arienzo et al., 2013) to analyze the stable isotope ($\delta^{18}O$ / $\delta^{2}H$) values in fluid inclusions from stalagmite ML-1. Using this method, I create a record of $\delta^{18}O$ and $\delta^{2}H$ variability from 20 to 12 ka in the central Sierra Nevada. The primary finding of this chapter is that there are periods in this record that are influenced by

kinetic fractionation. I conclude that this kinetic fractionation is likely due to variability in effective moisture above the cave, as lower relative humidity and recharge can cause kinetic fractionation in stalagmite calcite. The record correlates with regional records of effective moisture and demonstrates that the central Sierra Nevada went through periods of severe drying during the deglaciation.

Overall, this dissertation represents a large advancement in the methods used to study stalagmite paleoclimate records and a better understanding of the impacts on precipitation variability that occur in California due to warming temperatures.

Citations

Asmerom, Y., Polyak, V. and Burns, S.J., 2010, Variable moisture in the southwestern United States linked to rapid glacial climate shifts. *Nature Geosci.* 3, 114-117.

Arienzo, M.M., Swart, P.K. and Vonhof, H.B., 2013, Measurement of $\delta^{18}O$ and $\delta^{2}H$ values of fluid inclusion water in speleothems using cavity ring-down spectroscopy compared with isotope ratio mass spectrometry. *Rapid Comm. Mass Spectrom.* 27, 2616-2624.

Belmecheri, S., Babst, F., Wahl, E.R., Stahle, D.W. and Trouet, V. 2016, Multi-century evaluation of Sierra Nevada snowpack. *Nature Climate Change* 6, 2-3.

Cheng, H., Zhang, H., Zhao, J., Li, H., Ning, Y., Kathayat, G. 2019. Chinese stalagmite paleoclimate researches: A review and perspective. *Science China Earth Sciences*. 62: 1489-1513.

Cook, B. I., Cook, E. R., Anchukaitis, K. J., Seager, R. and Miller, R. L., 2011, Forced and unforced variability of twentieth century North American droughts and pluvials. *Clim. Dyn*. 37, 1097–1110.

Dettinger, M. D., Cayan, D. R., Diaz, H. F. and Meko, D. M., 1998, North–south precipitation

patterns in western North America on interannual-to-decadal timescales. *J. Clim*. 11, 3095–3111

Griffin, D. and Anchukaitis, K.J., 2014, How unusual is the 2012-2014 California drought? *Geophy*. *Res. Lett.* 41, 9017-9023.

Hatchett, B.J., Boyle, D.P, Putnam, A.E. and Bassett, S.D., 2015, Placing the 2012-2015 California-Nevada drought in to a paleoclimatic context: Insights from Walker Lake, California-Nevada, USA. *Geophy. Res. Lett.* 43, 8632-8640.

Kaufmann, G. 2003. Stalagmite growth and paleoclimate: the numerical perspective. *Earth and Planetary Sciences*. 214(1-2): 251-266.

Richards, D.A., Dorale, J.A. 2003. Uranium-series chronology and environmental applications of speleothems. *Reviews in Mineralogy and Geochemistry*. 52(1): 407-460.

McDermott, F. 2004. Paleo-climate reconstruction from stable isotope variations in speleothems: a review. *Quaternary Science Reviews*. 23(7-8): 901-918.

Meckler, A.N., Affolter, S., Dublyansky, Y.V., Kruger, Y., Vogel, N., Bernasconi, S.M., Frenz, M., Kipfer, R., Leuenberger, M., Spotl, C., Carolin, S., Cobb, K.M., Moerman, J., Adkins, J.F., Fleitmann, D. 2015. Glacial-interglacial temperature change in the tropical West Pacific: A comparison of stalagmite-base paleo-thermometers. *Quaternary Science Reviews*. 127: 90-116.

Oster, J.L., Montañez, I.P. and Kelly, N.P., 2012, Response of a modern cave system to large seasonal precipitation variability. *Geochim. Cosmochim. Acta* 91, 92-108.

Oster, J., Montañez, I.P., Mertz-Kraus, R., Sharp, W.D., Stock, G.M., Spero, H.J., Tinsely, J. and Zachos, J.C., 2014, Millenial-scale variations in western Sierra Nevada precipitation during

the last glacial cycle MIS 3-4 transition. *Quat. Res*. 82, 236-248.

Oster, J.L., Montañez, I.P., Wong, C.I., Santare, L., Sharp, W. and Cooper, K., 2015a, A multi-proxy stalagmite reconstruction of climate in the Sierra Nevada during the last deglaciation. *Quat. Sci. Rev.* 127, 199-214.

Parai, R., Mukhopadhyay, S., Tucker, J. M., Peto, M.K. 2019. The emerging portrait of an ancient, heterogeneous, and continuously evolving mantle plume source. *Lithos*. 105153; 345-347. doi.org/10.1016/j.lithos.2019.105153

Salathe, E.P., 2006, Influences of a shift in North Pacific storm tracks on western North American precipitation under global warming. *Geophys. Res. Lett*. 33, L19820.

Seager, R. and Vecchi, G. A., 2010, Greenhouse warming and the 21st century hydroclimate of southwestern North America. *Proc. Natl. Acad. Sci. USA* 107, 21277–21282.

Seager, R., Ting, M., Held, I., Kushnir, Y., Lu, J., Vecchi, G., Huang, H.-P., Harnik, N., Leetmaa, A., Lau, N.-C., Li, C., Velez, J. and Naik, N., 2007, Model projections of an imminent transition to a more arid climate in southwestern North America. *Science* 316, 1181–1184.

Seager, R., Ting, M., Li, C., Naik, N., Cook, B., Nakamura, J. and Liu, H., 2013, Projections of declining surface-water availability for the southwestern United States. *Nat. Clim. Change* 3, 482-486.

Seager, R., M. Hoerling, S. Schubert, H. Wang, B. Lyon, A. Kumar, J. Nakamura and N. Henderson, 2015, Causes of the 2011 to 2014 California drought*, J. Clim*. doi:10.1175/JCLI-D-14-00860.1,

Sewall, J.O., 2005, Precipitation Shifts over Western North America as a Result of Declining

Artic Sea Ice Cover: The Coupled System Response. *Earth Interactions* 9, 1-23.

Street, J.H., Anderson, R.S. and Paytan, A., 2012, An organic geochemical record of Sierra Nevada climate since the LGM from Swamp Lake, Yosemite. *Quat. Sci. Rev*. 40, 89-106.

Wagner, J.D.M., Cole, J.E., Beck, J.W., Patchett, P.J., Henderson, G.M. and Barnett, H.R., 2010, Moisture variability in the southwestern United States linked to abrupt glacial climate change. *Nat. Geosci.* 3, 110–113.

Wong, C.I., Breecker, D.O. 2015. Advancements in the use of speleothems as climate archives. *Quaternary Science Reviews*. 127: 1-8.

Wortham, B.E., Montañez, I.P., Rowland, D.J., Lerche, M., Browning, A. 2019. Mapping fluid-filled inclusions in stalagmites using coupled X-ray and neutron computed tomography: potential as a water-excess proxy. Geochemistry, Geophysics, Geosystems. 20(6): 2647-2656.

Wortham, B.E., Mukhopadhyay, S., Montañez, I.P., Middleton, J., Tyra, A. *In revision*. Western Sierra Nevada Temperature During the Last Glacial Maximum from stalagmite noble gas concentrations. Earth and Planetary Science Letters.

Chapter 1: Mapping fluid-filled inclusions in stalagmites using coupled X-ray and neutron computed tomography: potential as a water-excess proxy

This chapter is reproduced from the original publication: Wortham, B.E., Montañez, I.P., Rowland, D.J., Lerche, M., Browning, A. 2019. Mapping fluid-filled inclusions in stalagmites using coupled X-ray and neutron computed tomography: potential as a water-excess proxy. Geochemistry, Geophysics, Geosystems. 20(6): 2647-2656.

Abstract

Application of novel proxies, such as the stable isotope compositions and noble gas concentrations of fossil drip water trapped as inclusions in stalagmites, have the potential to provide unique constraints on past hydroclimate states and surface temperatures. Geochemical analysis of inclusion waters, however, requires an understanding of the three-dimensional spatial distribution of dominantly liquid- versus air-filled inclusions in a given stalagmite. Here we couple neutron computed tomography and medium- to high-resolution X-ray computed tomography to map out the three-dimensional calcite density and distribution of liquid- versus air-filled inclusions within a Sierra Nevada stalagmite (ML-1), which formed during the last deglaciation (18.5 to 11.7 ka). Comparison of coupled neutron computed tomography-X-ray computed tomography results with a time series of stalagmite calcite fabrics indicates that although highest density calcite contains abundant liquid (fluid)-filled inclusions, calcite density and fabric overall were secondary controls on the liquid inclusion distribution (LID). Furthermore, a multistatistical evaluation of the stalagmite time series indicates a significant relationship at the multicentury- to millennial-scale between LID and calcite $\delta^{18}O$ and $\delta^{13}C$ that

suggests a potential link between LID and water availability to the cave.

1. Introduction

X-ray computed tomography (XCT) scanning has been increasingly used in speleothem studies over the past decade to visualize the internal structure of stalagmites (Chawchai et al., 2018; Mickler et al., 2004; Munoz- Garcia et al., 2012; Shtober-Zisu et al., 2012, 2014), to develop a calcite density-based water excess proxy (Walczak et al., 2015), and to determine U-loss pathways (Bajo et al., 2016). Although XCT scanning is useful for reconstructing speleothem structure given the sensitivity of X-rays to the mineral calcite, X-rays are not sensitive to hydrogen (Schwarz et al., 2005; Tumlison et al., 2007; Wilding et al., 2005). Thus, XCT scanning can delineate inclusion void spaces, but it cannot delineate whether an inclusion is dominantly liquid- or air- filled in speleothems. Conversely, neutron computed tomography (NCT) scanning, with a resolution as high as 10 μm, has the potential to distinguish in a stalagmite between regions of dominantly liquid- versus air- filled inclusions given the high thermal neutron attenuation by hydrogen and the ability of neutrons to pene- trate through denser materials (Kim et al., 2013; Schwarz et al., 2005; Tumlison et al., 2007; Wilding et al., 2005). The high-resolution scale of NCT scanning can also distinguish between inclusions that are confined to stalagmite lamina (herein referred to as microinclusions; 10 to ~100 μm) and those inclusions that are con- sidered macropores (>100 μm). Therefore, coupling of these two techniques provides information on calcite density and fabric while also documenting the distribution of liquid- versus air-filled inclusions and macro- pores. Coupled XCT-NCT scanning has application to the interpretation of mineral or inclusion proxy records of speleothems as well as for further development of potential calcite density and fabric proxies of climate (e.g.,

Shtober-Zisu et al., 2012; Walczak et al., 2015; Zhang et al., 2010).

The coupled XCT-NCT scanning holds promise for developing new, or refining, environmental proxies for stalagmites. For example, stalagmite-based reconstructions of climate in the southwestern United States over the Pleistocene and Holocene are largely based on calcite $\delta^{18}O$ ($\delta^{18}O_{cc}$) time series (e.g., McDermott, 2004; McDermott et al., 2006; Vacco et al., 2005; Oster et al., 2009, 2015; Asmerom et al., 2010; Wagner et al., 2010; Ersek et al., 2012; Lachniet et al., 2014, 2017; Wong & Breecker, 2015). Inferring paleotemperatures andpaleoprecipitation patterns from $\delta^{18}O_{cc}$, however, is limited by the fact that $\delta^{18}O_{cc}$ values integrate the collective influence of surface and cave air temperatures, precipitation source, the evolution of water vapor $\delta^{18}O$ along the storm trajectory, rainfall amount, modifications to soil and drip water $\delta^{18}O$ through the epikarst, and kinetic fractionation during calcite precipitation (Mickler et al., 2004; McDermott, 2004; McDermott et al., 2006; Lachniet, 2009; Tremaine et al., 2011; Wong & Breecker, 2015). Stalagmite records of $\delta^{13}C$ and trace elements have been used to further constrain climate interpretations as these proxies are sensitive to precipitation amount and cave ventilation, which in turn are typically climate driven (Mickler et al., 2004; Oster et al., 2015). Stalagmite $\delta^{13}C$, however, is confounded by the presence of old sources of carbon (Noronha et al., 2015; Oster et al., 2010), variability in surface vegetation (Dorale et al., 1998; Frumkin et al., 2000), and soil respiration (Cruz et al., 2006; Denniston et al., 2013). Greater understanding of effective moisture, through the development of additional hydroclimate sensitive proxies, is essential to fully under- stand regional climate history. Calcite density has been proposed as a proxy for water excess driven by precipitation differences during stalagmite growth (Walczak et al., 2015; Zhang et al., 2010). This proxy has the potential to provide high-resolution information to compliment calcite geochemistry proxies if calcite denSity time series are developed using

nondestructive XCT scanning technique. The applicability of the water excess proxy to other stalagmites (Walczak et al., 2015), however, has not yet been tested to the best of our knowledge.

Here we apply coupled XCT-NCT scanning to a previously studied stalagmite (ML-1) from the western foothills of the central Sierra Nevada (supporting information; Oster et al., 2014, 2015) that spans the late glacial to early Holocene (18.5 to 11.7 ka). Application of coupled CT scanning to ML-1, an approach not previously used in speleothem studies, documents the ability to three-dimensionally map out on a 100-μm scale the distribution of liquid- versus air-filled inclusions in stalagmites within a calcite deNsity—internal structure framework of the stalagmite. Quantitative comparison of the time series of liquid-filled inclusion distribution (herein referred to as LID), calcite density, calcite fabric, and δ18Occ or δ13Ccc indicates that calcite density and fabric were secondary controls on LID. In addition to a lack of a temporally consistent relationship between calcite density, fabric, and LID, there is a moderate but significant relationship between LID and δ18Occ, at the multicentennial- to millennial-scale. Together, these findings suggest that the primary control on LID in the Sierran ML-1 stalagmite was water avail- ability and that LID may have potential as a nondestructive proxy of water excess (precipitation) in other stalagmites.

2. *Methodology*

The coupled NCT-XCT scanning used in this study provides a refined understanding of stalagmite internal structure as each of the two scanning technique is sensitive to different parameters.

2.1 XCT scanning

Stalagmite ML-1 is 22.5 cm long and was a cylindrical stalagmite that was cut in half and

polished for initial proxy development (Oster et al., 2014, 2015). To prepare stalagmite ML-1 for scanning, half of the stalagmite was cut to preserve the growth axis and make the stalagmite 9 cm wide and 5.5 cm deep so that it might fit in the scanning chamber at the Center for Molecular and Genomic Imaging at University of California Davis (UCD). Stalagmite ML-1 was XCT scanned at a medium resolution (193 μm) at the Center for Molecular and Genomic Imaging at UCD, and a portion (~5- to 13-cm depth) of the stalagmite was scanned at higher resolution (48.6 μm) by the ZEISS Microscopy Customer Center —Pleasanton, CA (Figure 1). Scanning at a medium resolution allowed for the entire stalagmite to be scanned, whereas the amount of stalagmite that could be scanned at a high resolution was limited due to scanning chamber dimensions. X-ray tomographic images were obtained on a Siemens InveonMM (Siemens Preclinical Inc.) and Zeiss Xradia 520 Versa (Carl Zeiss Microscopy, Inc.) with a Flat Panel extension, respectively. For the medium-resolution scan on the InveonMM, the stalagmite was imaged in three sections that were subsequently digitally stitched together. Additional information on scanning settings and process is provided in the supporting information. The tomographic image was reconstructed with a center shift (−0.67 pixels) and beam-hardening parameter value of 0.05 in order to obtain optimized images. A 2-D Gaussian smoothing filter of kernel size 0.7 was applied during reconstruction, and the images were reconstructed into 16-bit values.

2.2 NCT scanning

NCT scanning was performed on the upper 20 cm of stalagmite ML-1 using a 2MW TRIGA reactor at the McClellan Nuclear Research Center, UCD. The detector setup is equipped with a 100-μm-thick ^{6}LiF-ZnS scintillator and an Apogee Alta charge-coupled device camera system. The stalagmite was placed on a rota- tion stage, and the initial NCT imaging was carried out by

collecting a series of radiographs while rotating the sample in 1° increments from 0° to 180°. Two frames-per-angular position were acquired with 45-s expo- sure time per frame, and an image of the average of the two frames was recorded. Radiographic images were dark field and flat field corrected. *Octopus* reconstruction software was used for the reconstruction of the tomography data (Vlassenbroeck et al., 2007). The neutron tomography data were saved as 16-bit tiff files; the resulting voxel size is 116 μm, whereas the overall image resolution is ~350 μm. Although NCT scanning is sensitive for other elements and isotopes in addition to hydrogen (Kim et al., 2013; Tumlison et al., 2007; Wilding et al., 2005) that occur typically in very low concentrations in stalagmites and thus do not attenuate neutrons as highly as hydrogen (Figure S1; Kim et al., 2013). The NCT scan images were overlain upon the XCT-scanned images for positioning (Figure 1). To assess the concentration of layers with air-filled versus liquid-filled macropores in stalagmite ML-1, Amira software (FEI-SAS, 2018) was used to segment the three-dimensional (3-D) NCT scans (Figure 1) and render the scans in three dimensions (Figure S1). The resulting images are based on voxel color intensity where the brightest regions are interpreted as liquid-filled macropores and the darkest regions are interpreted as air-filled macropores (Figure S1). The image scans were converted to time series of LID and calcite density (supporting information; Figure 1) and analyzed sta- tistically using general additive modeling (GAM; Everitt & Horton, 2010), cross-wavelet analysis (Grinsted et al., 2004), and Spearman's rank correlation (supporting information).

3. Results

The XCT and NCT scanning of ML-1 (Figure 1) verify the 3-D distribution of calcite fabrics, which were previously identified using petrographic thick sections (200 μm) distributed along a 2-D plane parallel to the growth axis (Oster et al., 2015). Three fabrics are observed in ML-1: (1)

inclusion-poor columnar compact calcite (C), (2) inclusion-rich columnar open calcite (Co), and (3) columnar open with random c-axis orientation (Co-r) calcite (Frisia et al., 2000; Frisia, 2015; Figure 2). XCT scanning reveals that the banding, delineated by calcite fabrics, extends off of the growth axis in all directions with thinning of the bands toward the stalag- mite edges (Figure 1). Coupled NCT-XCT scanning further confirms the interlaminated banding between the inclusion-rich Co fabric and inclusion-poor C fabric in the lower half of ML-1 (lower 13.5 cm) and relates the banding to LID (Figure 1B). The inclusion-rich banding in the upper portion of ML-1 (upper 10 cm), not previously identified by pet- rographic study, is consistently traceable off of the growth axis and includes abundant macropores in distinct regions (Figures 1B and S1).

The coupled NCT-XCT scanning of ML-1 further reveals a complex rela- tionship between calcite density and fabric and the LID and stable isotopic proxy time series (Figure 2 and Table 1). A significant inverse relationship exists between calcite fabric and density ($r_s = -0.25$, $p < 0.05$; Table 1), a relationship that has been previously documented (Chawchai et al., 2018; Walczak et al., 2015). Although calcite density shows a significant rela- tionship to LID ($r_s = 0.27$, $p < 0.05$; Table 1), calcite fabric does not ($r_s = 0.02$, $p > 0.05$). Visually, calcite density varies on a short (100-year) timescale but is mostly invariant on longer (i.e., 1,000 years) timescales up to the interval of transition (14.5 ka) from alternating C and Co fabric to Co and Co-r fabric that corresponds to sustained and amplified shifts in calcite density (Figure 2). GAM results provide insight into the origin of the complex relationship between calcite density and fabric and LID in the ML-1 stalagmite. First, on a higher spatial resolution-scale, GAM indi- cates the relationship between calcite fabric and density is associated with large uncertainty (low predictability; Figure S2A). Second, a statistically predictable relationship between LID and calcite density or fabric is lim- ited to (a) high-density stalagmite intervals (Figure S2B) or (b)

the densest fabric, inclusion-poor columnar compact calcite (Figure S2C). Thus, the statistically significant relationship between calcite fabric and calcite den- sity is not consistent throughout the stalagmite.

Visually, on a first-order scale (millennia), the LID and $\delta^{18}O_{cc}$ time series for ML-1 are inversely related (Figure 3A). This qualitative relationship is reflected in a statistically significant but weak negative correlation between LID and $\delta^{18}O_{cc}$ ($r_s = -0.22$; $p < 0.05$; Table 1) and the pre- dictable relationship between the two parameters defined by GAM (Figure S2D). Specifically, the strongest predictable relationship between stalagmite $\delta^{18}O_{cc}$ and LID exists for intervals dominated by $\delta^{18}O_{cc}$ values ≤−9.7‰ (Figure S2D). Cross-wavelet analysis of LID and $\delta^{18}O_{cc}$ further reveals a slight inverse phasing (~135° lag) on a millennial timescale (periodicity of 32) that is strongest during the Allerod (12.7 to 13.8 ka) and LGM (17.2 to 18 ka) intervals; deli- neated by bright yellow areas on Figure 3B. LID and $\delta^{18}O_{cc}$ for the other intervals of the time series have an out-of-phase relationship on the centennial scale when analyzed visually (100–300 years; Figure 2). This apparent centennial-scale relationship between LID and δ18Occ, however, cannot be further tested by cross-wavelet analysis or GAM given that the phasing of the time series changes throughout the record leading to insignificant relationships with these statistical tests. Notably, calcite density has no statistically significant relationship to δ18Occ (rs = −0.03, p > 0.05; Table 1).

A significant but very weak inverse relationship exists between δ13Ccc and LID (rs = −0.19, p < 0.05; Table 1), whereas a stronger positive relationship exists between δ13Ccc and calcite density (rs = 0.29, p < 0.05; Table 1) and δ13Ccc and calcite fabric (rs = −0.68, p < 0.05; Table 1). This relationship between δ13Ccc and LID is observed visually on the short-term (100–300 years; Figure 3A), with the same two exceptions for the LGM and first half of the Allerod

intervals that were observed between LID and δ18Occ. GAM and cross-wavelet analysis, however, do not indicate high predictability or significant phasing between δ13Ccc and LID (Figure 3C).

4. Discussion

NCT further contributes to previous stalagmite studies that have successfully applied XCT scanning to assess 3-D variability in stalagmite growth (growth fabrics and structure, internal porosity; e.g., Mickler et al., 2004; Martinez-Martinez et al., 2010; Shtober-Zisu et al., 2012; Walczak et al., 2015; Chawchai et al., 2018), and the distribution of liquid- versus air-filled inclusions are compared to traditional stalagmite proxies to evaluate the use of scanning techniques as a water excess proxy in stalagmites.

4.1 Evaluating diagenetic alteration

The coupled XCT-NCT scanning confirms that the macropores in ML-1 are primary features, an interpreta- tion that for ML-1 was difficult to establish unequivocally by petrographic study of samples collected for thin sectioning from a 2-D plane that followed the stalagmite growth axis (Oster et al., 2015). Macropores in the upper half of the ML-1 stalagmite were previously noted as spatially associated with Co-r fabric (Oster et al., 2015), but whether the macroporosity was primary or was postformation created by interaction with under- saturated liquids, subsequently introduced into the cave, remained equivocal in ML-1. The coupled scanning approach, including high-resolution XCT scanning, documents that the macropores in ML-1 occur in discrete bands delineated by the calcite fabrics (Figures 1A and 1B) and are air-filled (Figure S1A) or liquid-filled (Figure S1B). Individual calcite crystals nucleating from the internal walls of macropores exhibit a c-axis orientation parallel with the growth direction of the calcite crystals that define the calcite fabric bands (Figure 1C). These features argue for a primary

crystallization origin for the macropores in stalagmite ML-1. Secondary dissolution macropores, in contrast, would be expected to cross-cut growth bands (e.g., Bajo et al., 2016) and calcite crystal growth in these macropores would be randomly orientated relative to calcite crystals in the adjacent laminae/banding that host the macropore. Thus, coupled XCT-NCT scanning of stalagmites opens up the possibility of targeting and isolating for sampling liquid-filled macropores, which may contain volumes (μl) of trapped fossil drip water that can be successfully extracted for analysis.

4.2 Fluid inclusion mapping

Application of coupled XCT-NCT scanning will improve fluid inclusions studies in stalagmites that have been hindered by an inability to a priori know whether a sample will have inclusions that contain a high volume of trapped liquid or will be primarily air filled. As previously noted by other stalagmite inclusion stu- dies, large liquid-filled inclusions in stalagmites are limited despite significant internal porosity (Shtober- Zisu et al., 2012). Similarly, there is a limited number of large liquid-filled inclusions in stalagmite ML-1. All regions in stalagmite ML-1 with sealed microinclusions, however, are liquid-filled dominated. The 3-D distribution map of liquid-filled inclusions and size analysis of liquid-filled inclusions offered by the coupled scanning approach offers three distinct advantages for speleothem sampling. First, the potential to isolate regions dense in liquid-filled micropores that are ideal samples for crushing techniques, which release all of the fluid in one sample through physical destruction of the calcite lattice (e.g., Arienzo et al., 2013, 2015; Ghadiri et al., 2018). Second, the potential to isolate larger liquid-filled macropores, ideally suited for laser paleofluid temperatures analysis, can be estimated (Kruger et al., 2011). And third, the 3-D images produced by the scanning methods allow for each pore to be segmented virtually based on ranges of density (Schillinger et

al., 2000). The virtual segmentation of the stalagmite allows for a 3-D assessment of whether pore spaces are connected or are surrounded on all sides by calcite, which appears denser (supporting infor- mation Figure S2). Virtually segmented stalagmites provides insight into the potential impact of leakage on the distribution of fossil liquids and the possibility of reequilibration of the liquid to the modern atmosphere and alteration of noble gas concentrations (e.g., Kluge et al., 2008) and stable isotopic signatures (Mickler et al., 2004).

4.3 Potential of FID as an environmental proxy

Temporal variability in calcite density of stalagmites (Walczak et al., 2015; Zhang et al., 2010) has been inter- preted as a proxy of change in cave system environmental conditions (water flow dynamics, drip water saturation state, cave pCO2), which in turn have been shown by cave monitoring studies to be controlled by above-cave climate (precipitation and temperature), soil conditions, and vegetation density and type. The mechanistic linkage of variability in calcite density to environmental change has been further related to calcite fabrics in stalagmites (Chiarini et al., 2017; Frisia, 2015; Frisia et al., 2000). For cave systems char- acterized by limited seasonal variability in pCO2, calcite density has been proposed as a proxy of water excess (i.e., drip rate) and precipitation amount above the cave (Walczak et al., 2015; Zhang et al., 2010). Denser calcite is interpreted to record higher and less seasonally distributed precipitation and vice versa. To what degree calcite density can serve as a proxy of climate-driven water dynamics in a cave characterized by sea- sonal variability in pCO2 has not been evaluated to date despite the documented strong influence of variability in cave pCO2 on rates of CO2 degassing, degree of supersaturation of drip water, and calcite pre- cipitation mode (Boch et al., 2011; Mattey et al., 2010; Wong & Banner, 2010). For the ML-1 stalagmite, the lack of a clear or strong relationship between calcite density and δ18Occ, which is interpreted to be the

pri- mary proxy of air surface temperature and precipitation patterns above the Sierra Nevada foothill caves (Oster et al., 2012, 2015), indicates that calcite density is not straightforwardly related to water availability.

For stalagmite ML-1, there is a positive significant relationship (+0.29; Table 1) between calcite density and δ13Ccc that provides further insight into the influence of environmental processes, other than water avail- ability, on calcite density and fabric in the McLean's Cave system. Variability in the ML-1 δ13Ccc time series has been previously interpreted as archiving long-term variability in cave air pCO2 and CO2-degassing rate of drip water (Oster et al., 2010). Periods of overall greater but highly variable CO2-degassing rates and degrees of supersaturation of drip waters are inferred from intervals of higher ML-1 δ13Ccc values. Conversely, periods of overall lower but more stable supersaturation state of drip waters are inferred from intervals of lower δ13Ccc values (Oster et al., 2015). Notably, a mechanistic linkage has been proposed between inferred variability in cave pCO2 and degassing rates of drip waters in the Sierran cave systems and precipitation patterns over the region (Oster et al., 2009, 2014, 2015). This linkage between δ13Ccc and rainfall indicates that inferred intervals of overall lower precipitation are associated with higher δ13Ccc values, whereas periods of lower precipitation are characterized by lower δ13Ccc values. Therefore, the observed positive relationship between δ13Ccc and calcite density in stalagmite ML-1 indicates that intervals of higher calcite density are inferred periods of overall lower precipitation, a finding that is contradictory to the calcite density-water excess relationship proposed by Walczak et al. (2015). This suggests that the calcite- density proxy of water excess (Walczak et al., 2015) cannot be straightforwardly applied to the stalagmite ML-1 from a cave system characterized by strong seasonal variability. Rather, the relationship between δ13Ccc, calcite density, and regional precipitation reflects the complex

interplay of pCO2, temperature, and water flow dynamics in McLean's Cave and their influence on stalagmite density and stable isotopic compositions.

A significant and predictable inverse relationship between LID and δ18Occ according to the Spearman's rank correlation test and GAM (−0.22 and $p < 0.05$; Figures S2D and 3) in the ML-1 stalagmite suggests that water availability above McLean's Cave may have been the primary influence on the amount of liquid that was trapped and preserved in inclusions. Such a link between volume of liquid-filled inclusions and δ18Occ has been previously noted for a stalagmite from Yemen (Vogel et al., 2013). For stalagmite ML-1, higher LID in intervals of lower δ18Occ, at the multicentennial- to millennial-scale (Figure 3), suggests that liquid inclusion distribution may be a more applicable proxy for water excess (availability) in seasonally ventilated (or climatic) cave systems. In particular, the strong relationship between LID and δ18Occ, when the latter values are <−9.7‰ argues for greater LID during periods of overall greater precipitation. For the Sierran caves, variability in stalagmite δ18Occ coincides with fluctuations in air surface temperature over Greenland during the last deglaciation (Oster et al., 2009; Oster & Kelley, 2016). Although temperature and moisture source (i.e., North Pacific- vs. subtropical-sourced storms) influence precipitation δ18O in California, precipitation intensity during individual storms and/or over the winter wet season also imparts a signature on δ18Oprecip with more negative δ18O values associated with greater precipitation (e.g., Oster et al., 2012; Wortham et al., 2017). A slightly weaker inverse correlation between LID and δ13Ccc (−0.19, $p < 0.05$) corroborates this interpretation of LID as a proxy of water availability as lower δ13Ccc values in ML-1 have been associated with greater effective moisture and soil respiration in the Sierran cave systems (Oster et al., 2009, 2012).

Given that calcite density and fabric are significantly correlated in the ML-1 stalagmite (0.27, $p \leq 0.05$) and liquid-filled inclusions are variable across all three fabric types (Figure 2) raises a caveat to the calcite density proxy of water (excess) availability (Walczak et al., 2015; Zhang et al., 2010). That is, one can expect from the aforementioned proposed relationship between calcite density-fabric-water availability that intervals of higher calcite density in a given stalagmite would have greater potential for trapping and preserving liquid-filled inclusions in the denser, more compact calcite hypothesized to precipitate under steady, high drip rates of overall low supersaturation state (Frisia et al., 2000). This anticipated relationship, however, breaks down in stalagmite ML-1 as intervals of high LID occur in both more porous calcite fabric (Co-r = columnar open random) and the most dense calcite of columnar compact fabric (C on Figure 2).

Changing precipitation sources across the Pacific impacted stalagmite δ18Occ over the past 20 ka in the wes- tern Sierra Nevada (Oster et al., 2009, 2012, 2014, 2015) and may provide additional constraints on the inferred variability in water excess. A 5-year monitoring effort at Black Chasm Cavern (Oster et al., 2012) suggests that the predominant precipitation source for these cave systems is a North Pacific source (−15.5 ± 0.4‰ δ18O) with a secondary subtropical source from which atmospheric river events are initiated (−6.4 ± 2.5‰ δ18O). The modern framework has been used to infer from the Sierran stalagmite δ18Occ records primarily millennial-scale shifts in precipitation source and temperature over the last deglaciation (Oster et al., 2015) that were related to changing synoptic atmospheric dynamics (Wong et al., 2016; Lora et al., 2016). We further hypothesize that based on the significant and predictable relationship between LID and δ18Occ that is visually supported (Figure 3A) and statistically supported on millennial timescales (Figure 3B) that the millennial- and centennial-scale shifts in precipitation

source also involved changes in precipitation amount above the cave and degree of water infiltration. Intervals characterized by δ18Occ values <9.7‰ and higher LID are associated with inferred cooler periods with a predominant North Pacific precipitation source, whereas intervals of overall higher δ18Occ and lower LID are associated with warmer periods with a likely shift to increased contribution to mean precipitation from subtropical storms. The potential of LID as a proxy of water availability evaluated in this study for a cave system characterized by geochemical variability reflecting seasonality (Oster et al., 2012) requires further evaluation in stalagmites from cave systems of differing environmental conditions, including in stalagmites for which total volume of water released from liquid inclusions per unit volume of calcite can be accurately measured (cf. Vogel et al., 2013).

5. *Conclusions*

We present a coupled neutron and XCT approach that provides a robust visualization of the internal struc- ture and spatial distribution of liquid- and air-filled inclusions in stalagmites. The application of NCT, in combination with XCT, may be further applicable to other paleoclimate archives including sediment cores and corals. The approach outlined in this study permits quantitative assessment of the spatial relationship of liquid trapped in mineral frameworks as inclusions to other proxy indicators or to improve methodology for geochemical analysis. Imaging the structure and the distribution of both air- versus liquid-filled inclu- sions in a stalagmite is important for liquid inclusion proxy and geochemical studies by reducing the poten- tial for contamination and water loss during sample preparation as well as for mapping out their 3-D distribution for analysis. In this study of a stalagmite from a Sierra Nevada foothill cave, the observed rela- tionship between δ18Occ and LID indicates a significant influence of water availability (excess) on the distri- bution of liquid-filled inclusions suggesting that LID is a

potential proxy for water excess. Figures

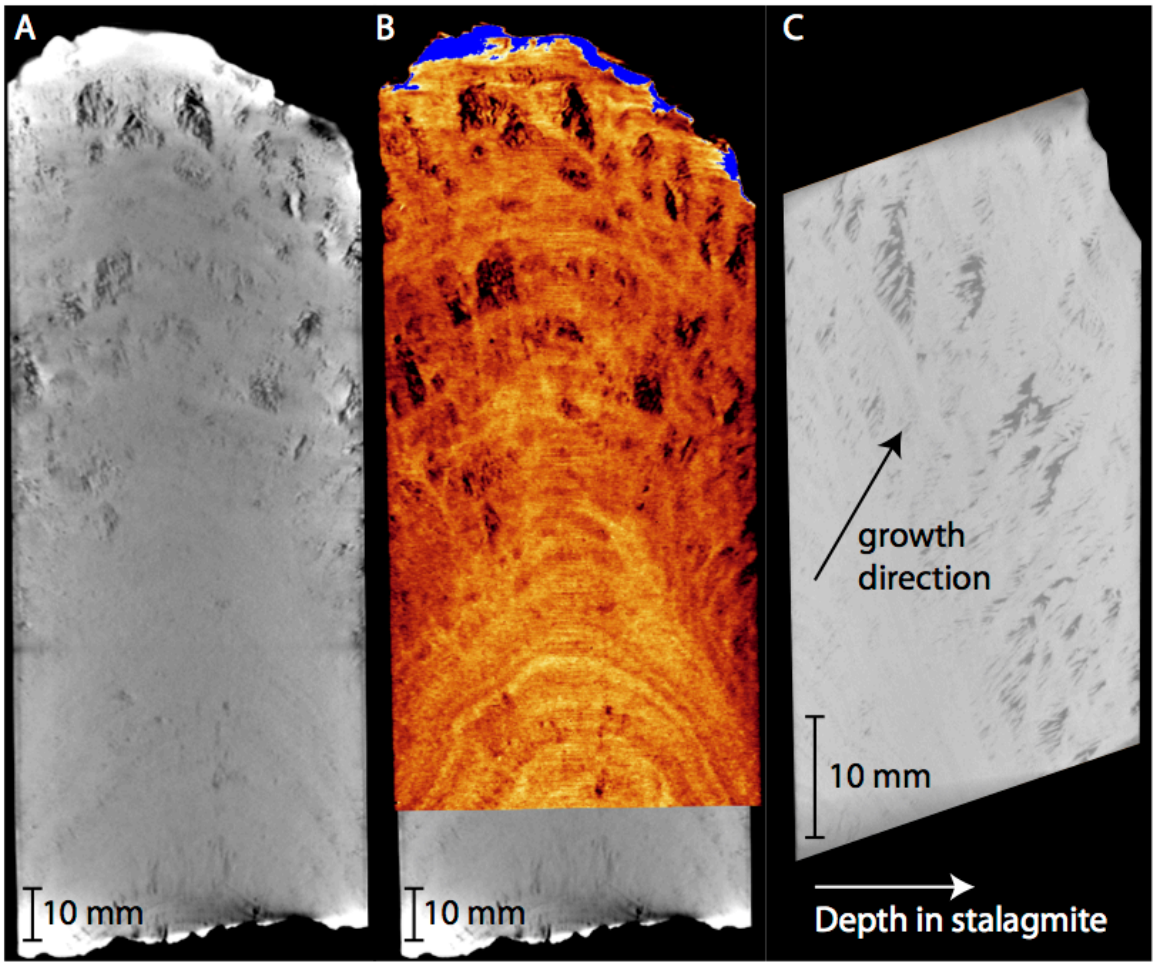

Figure 1*:* XCT and NCT scans of stalagmite ML-1. (A) Medium-resolution XCT scan with interval (middle) of high-resolution imaging superimposed. Darker regions indicate less dense calcite and/or porosity. (B) Superposition of the NCT scan (orange-red) on the medium-resolution XCT scan. Regions of brighter voxel intensity indicate greater hydrogen concentrations (water). Blue regions have the highest voxel intensity and are interpreted in this image as edge artifacts. (C) Slice of high-resolution XCT scan illustrating depth of stalagmite

ML-1. Arrow indicates inferred growth direction.

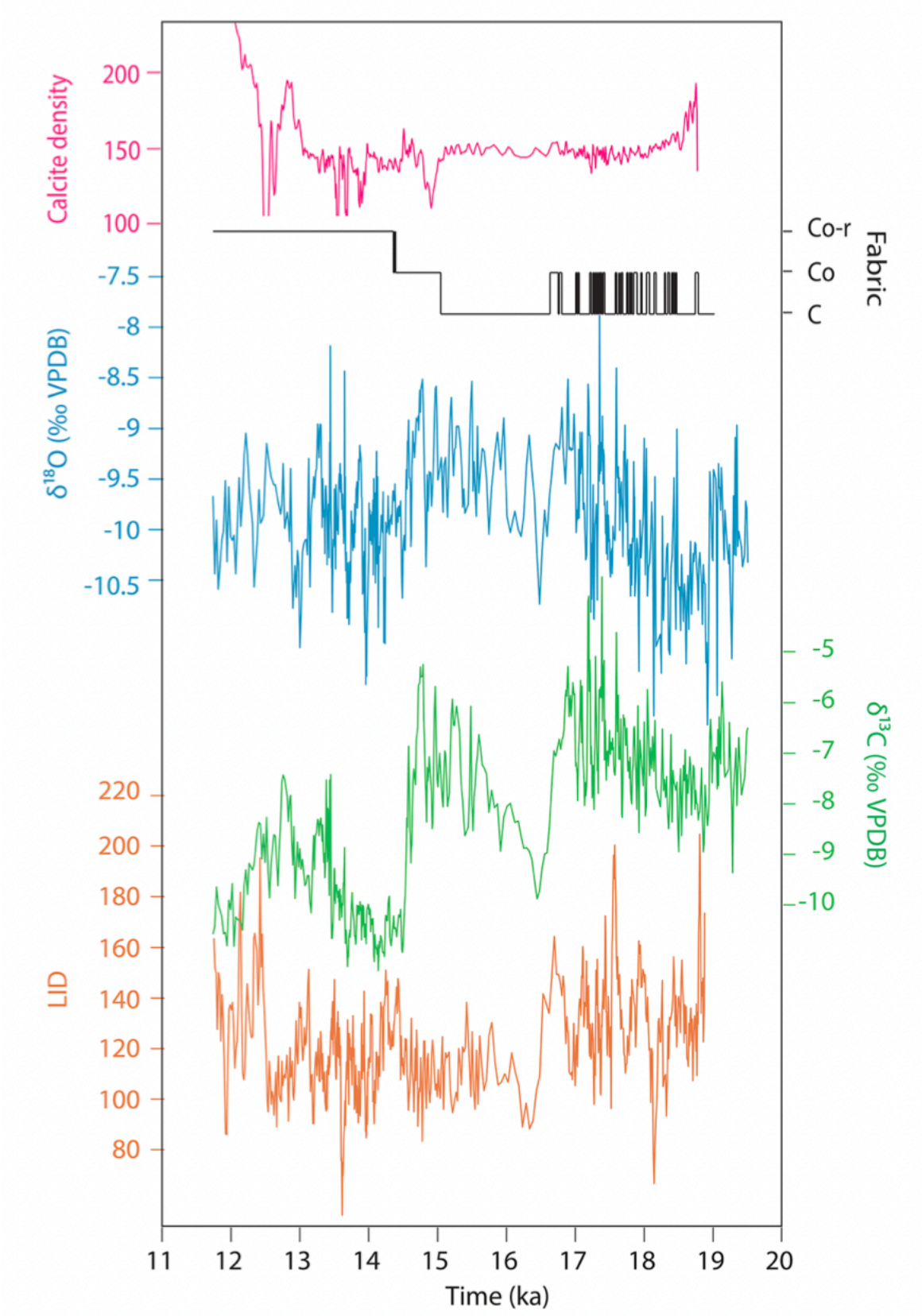
Calcite density
200
150
100
Fabric
Co-r
Co
C
-7.5
-8
-8.5
-9
-9.5
-10
-10.5
δ18O (‰ VPDB)
-5
-6
-7
-8
-9
-10
δ13C (‰ VPDB)
220
200
180
160
140
120
100
80
LID
11
12
13
14
15
16
17
18
19
20
Time (ka)

Figure 2: Time series of scanning proxies, calcite fabric, and stalagmite growth rate. Time series of distribution of density of fluid inclusions (FID; red) and calcite density (pink) defined using ImageJ analysis of the relative voxel intensity in the NCT scan and XCT scan, respectively. (C) Calcite fabrics petrographically determined (black line): columnar closed (C), columnar open (Co), and columnar open with random c-axis orientation (Co-r). Stable isotopes series previously developed in Oster et al. (2015) are the $\delta^{18}O_{cc}$ (blue) and $\delta^{13}C_{cc}$ LGM = Last Glacial Maximum (>17.5 ka), BD = Big Dry (16.2 to 17.5 ka, citation), BW= Big Wet (15 to 16.2 ka, citation), BO=Bolling (14.5 to 15 ka), OD = Older Dryas (13.5 to 14.5 ka), AL = Allerod (12.7 to 13.5 ka), YD = Younger Dryas (< 12.7 ka).

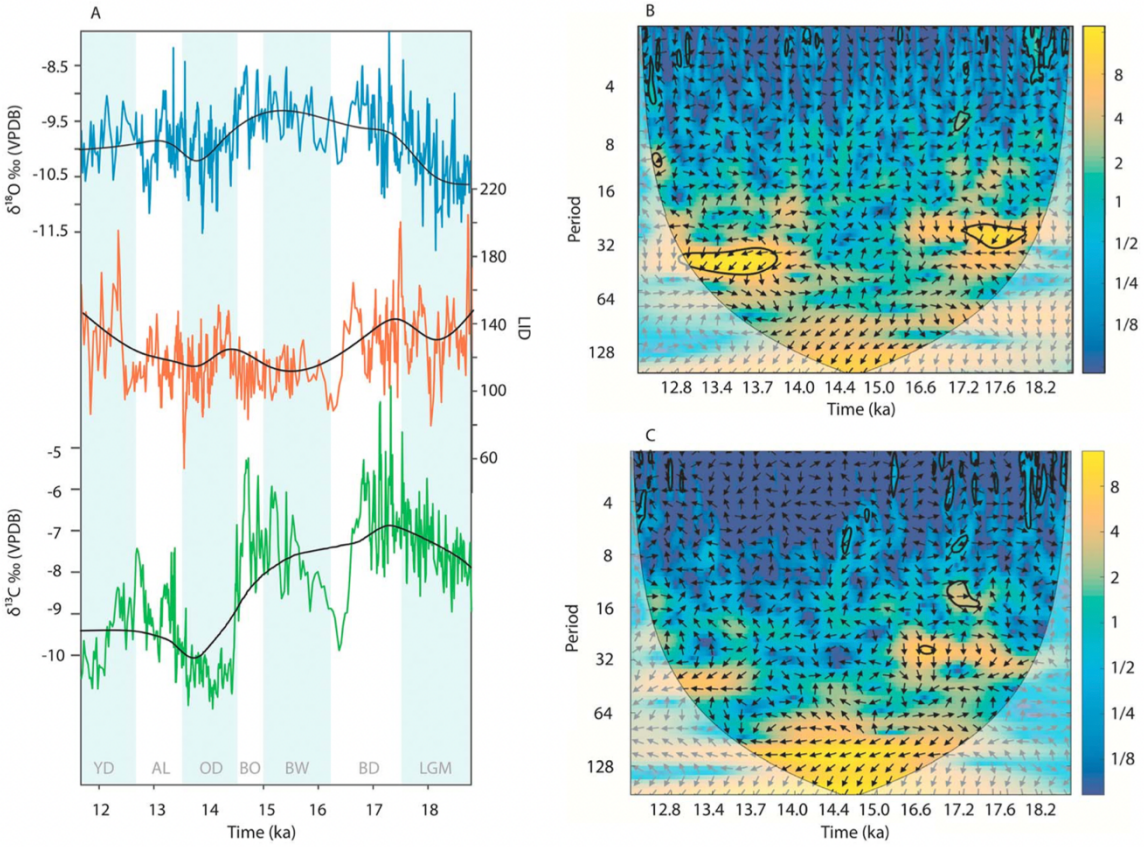

Figure 3: Cross-wavelet analysis for the FID, $\delta^{18}O_{cc}$, $\delta^{13}C_{cc}$ time series. (A) The wavelet analyses were based on the time series of $\delta^{18}O_{cc}$ (blue), FID (red), and $\delta^{13}C_{cc}$ (green) shown with cubic

spline smoothing (black) on each time series. Wavelet analysis transforms time-series into time-frequency space and assesses the correlation between those frequencies at variable periods (B). (B) The cross wavelet analysis of $\delta^{18}O_{cc}$ and FID. (C) the cross-wavelet analysis of $\delta^{13}C_{cc}$ and FID. The highest power of correlation is indicated by a brighter yellow color and the most significant areas of correlation are outlined in black. Phasing of the two time-series is assessed and indicated by black arrows where a right pointing arrow would indicate perfectly in-phase. The time-series (bottom) are visually out of phase at the short-term scale (100-300 years) and at the long-term scale (1000 years). The black line indicates a LOESS smoothing of the $\delta^{18}O_{cc}$ (blue) and the FID (red). The blue bars (bottom) are consistent with Fig. 2.

6. *Citations*

Abramoff, M.D., Magalhaes, P., Ram, S.J. (2004) Image processing with ImageJ. Biophotonics international. 11(7): 36-42.

Arienzo, M.M., Swart, P.K., Vonhof, H.B. (2013) Measurement of δ18O and δ2H values of fluid inclusion water in speleothems using cavity ring-down spectroscopy compared with isotope ratio mass spectrometry. Rapid communications in mass spectrometry. 27(23): 2616-2624.

Arienzo, M.M., Swart, P.K., Pourmand, A., Broad, K., Clement, A.C., Murphy, L.N., Vonhof, H.B., Kakuk, B. (2015) Bahamian speleothem reveals temperature decrease associated with Heinrich stadials. Earth and Planetary Science Letters. 430: 377-386.

Asmerom, Y., Polyak, V.J., Burns, S.J. (2010) Variable winter moisture in the southwestern United States linked to rapid glacial climate shifts. Nature geoscience. 3: 114-117.

Bajo, P., Hellstrom, J., Frisia, S., Drysdale, R., Black, J., Woodhead, J., et al. (2016) Cryptic diagenesis and its implications for speleothem geochronologies. Quaternary Science Reviews.

148: 17-28.

Boch, R., Spotl, C., Frisia, S. (2011) Origin and palaeoenvironmental significance of lamination in stalagmites from Katerloch Cave, Austria. Sedimentology. 508-531.

Brietenbach, S.F.M., Rehfeld, K., Goswami, B., Baldini, J.U.L., Ridley, H.E., Kennett, D.J., et al. (2012) Constructing Proxy Records from Age models (COPRA). Clim. Past. 8: 1765-1779.

Chawchai, S., Liu, G., Bissen, R., Jankham, K., Paisonjumlongsri, W., Kanjanapayont, et al. (2018) Stalagmite from western Thailand: preliminary investigations and challenges for palaeoenvironmental research. Boreas. 47(1): 367-376.

Chiarini, V., Chouchoud, I., Drysdale, R., Bajo, P., Milanolo, S., Frisia, S., et al. (2017) Petrographical and geochemical changes in Bosnian stalagmites and their paleo-environmental significance. International Journal of Speleology. 46(1): 33-49.

Cruz, F.W.Jr., Burns, S.J., Karmann, I., Sharp, W.D., Vuille, M., Ferrari, J.A. (2006) A stalagmite record of changes in atmospheric circulation and soil processes in the Brazilian subtropics during the Late Pleistocene. Quaternary Science Reviews. 25(21-22): 2749-2761.

Denniston. R.F., Asmerom, Y., Lachniet, M., Polyak, V.J., Hope, P., An, N., et al. (2013) A Last Glacial Maximum through middle Holocene stalagmite record of coastal Western Australia climate. Quaternary Science Reviews. 77: 101-112.

Dorale, J.A., Edwards, R.L., Ito, E., Gonzalez, L.A. (1998) Climate and vegetation history of the midcontinent from 75 to 25 ka: A speleothem record from Crevice Cave, Missouri, USA. Science. 282: 1871-1874.

Ersek, V., Clark, P.U., Mix, A.C., Cheng, H., Edwards, R.L., (2012) Holocene winter climate variability in mid-latitude western North America. Nat. Comm. 3: 1219.

Everitt, B., Hothorn, T. (2009) A handbook of statistical analyses using R. Chapman &

Hall/CRC.

Frisia, S., Borasato, A., Fairchild, I.J., McDermott, F. (2000) Calcite fabrics, growth mechanisms, and environments of formation ins speleothems from the Italian Alps and Southwestern Ireland. 70(5): 1183-1196.

Frisia, S. (2015) Microstratigraphic logging of calcite fabrics in speleothems as tool for paleoclimate studies. International Journal of Speleogy. 44(1): 1-16.

Frumkin, A., Ford, D.C., Schwarcz, H.P. (2000) Paleoclimate and vegetation of the last glacial cycles in Jerusalem from a speleothem record. Global Biogeochemical Cycles. 14(3): 863-870.

Ghadiri, E., Vogel, N., Brennwald, M.S., Maden, C., Hauselmann, A.D., Fleitmann, D., et al. (2018) Noble gas based temperature reconstruction on a Swiss stalagmite from the last glacial-interglacial transition and its comparison with other climate records. Earth and Planetary Science Letters. 495: 192-201.

Grinsted, A., Moore, J. C., Jevrejeva. S. (2004) Application of the cross wavelet transform and wavelet coherence to geophysical time series. Nonlinear Processes in Geophysics, European Geosciences Union (EGU). 11 (5/6): 561-566.

Kim, F.H., Penumadu, D., Gregor, J., Kardjilov, N., Manke, I. (2013) High-resolution neutron and X-ray imaging of granular materials. Journal of Geotechnical and Geoenvironmental Engineering. 139(5): 715-723.

Kluge, T. Marx, T., Scholz, D., Niggemann, S., Mangini, A., Aeschbach-Hertig, W. (2008) A new tool for paleoclimate reconstruction: noble gas temperatures from fluid inclusion in speleothems. Earth and Planetary Science Letters. 269 (3-4): 408-415.

Kruger, Y., Marti, D., Staub, R.H., Fleitmann, D., Frenz, M. (2011) Liquid-vapour homogenization of fluid inclusions in stalagmites: evaluation of a new thermometer for

palaeoclimate research. Chemical Geology. 289: 39-47.

Lachniet, M.S. (2009) Climatic and environmental controls on speleothem oxygen-isotope values. Quaternary Science Reviews. 28: 412-432.

Lachniet, M.S., Denniston, R.F., Asmerom, Y., Polyak, V.J. (2014) Orbital control of western North America atmospheric circulation and climate over two glacial cycles. Nature Comm. 5: 3805

Lachniet, M.S., Asmerom, Y., Polyak, V., Denniston, R. (2017) Arctic cryosphere and Milankovitch forcing of Great Basin paleoclimate. Scientific Reports. 7(1): 12955.

Mattey, D.P., Fairchild, I.J., Atkinson, T.C., Latin, J.-P., Ainsowrth, M., Durell, R. (2010) Seasonal microclimate control of calcite fabrics, stable isotopes, and trace elements in modern speleothem from St. Michaels Cave, Gibraltar. Geological Society, London, Special Publications. 336: 323- 344.

McDermott, F. (2004) Palaeo-climate reconstruction from stable isotope variations in speleothems: a review. Quaternary Science Reviews. 23(7-8): 908-918.

McDermott, F., Schwarcz, H., Rowe, P.J. (2006) Isotopes in speleothems. Isotopes in Palaeoenvironmental Research. Developments in Paleoenvironemtnal Research. Pp 185-225.

Mehterian, S., Pourmand, A., Sharifi, A., Lahijani, H.A.K., Naderi, M., Swart, P.K. (2017) Speleothem Records of Glacial/Interglacial Climate from Iran Forewarn of Future Water Availability in the Interior of the Middle East. Quat. Sci. Rev. 164: 187-198.

Mickler, P., Ketcham, R., Colbert, M. and Banner, J. L., (2004) Application of high-resolution X-ray computed tomography in determining the suitability of speleothems for use in paleoclimatic and paleohydrologic reconstructions. J. Cave Karst Studies 66, 4-8.

Munoz-Garcia, M.B., Lopez-Arce, P., Fernandez-Valle, M.E., Dwanckele, J., Martin-Chivelet,

J., Fort, R., Cnudde, V. (2012) Weathering of speleothems: study of diagenesis with non-destructive techniques. Geophysical Research Abstracts. Vol. 14.

Noronha, A.L., Johnson, K.R., Southon, J.R., Hu, C., Ruan, J., McCabe-Glynn, S. (2015) Radiocarbon evidence for decomposition of aged organic matter in the vadose zone as the main source of speleothem carbon. Quaternary Science Reviews. 127: 37-47.

Oster, J.L., Montanez, I.P., Sharp, W.D., Cooper, K.M. (2009) Late Pleistocene California droughts during deglaciation and Arctic warming. Earth and Planetary Science Letters. 288(3-4): 434-443.

Oster, J.L., Montanez, I.P., Guilderson, T.P., Sharp, W.D., Banner, J.L. (2010) Modeling speleothem δ13C variability in a central Sierra Nevada cave using 14C and 87Sr/86Sr. Geochimica et Cosmochimca Acta. 74: 5228-5242.

Oster, J.L., Montanez, I.P., Kelley, N.P. (2012) Response of a modern cave system to large seasonal precipitation variability. Geochimica et Cosmochimica Acta. 91: 92-108.

Oster, J.L., Montanez, I.P., Mertz-Kraus, R., Sharp, W.D., Stock, G.M., Spero, H.J., et al. (2014) Millennial-scale variations in western Sierra Nevada precipitation during the last glacial cycle MIS 4/3 transition. Quaternary Research. 82(1): 236-248.

Oster, J.L., Montanez, I.P., Santare, L.R., Sharp, W.D., Wong, C., Cooper, K.M. (2015) Stalagmite records of hydroclimate in central California during termination 1. Quaternary Science Reviews. 127: 199-214.

Oster, J.L., Kelley, N.P. (2016) Tracking regional and global teleconnections recorded by western North American speleothem records. Quaternary Science Reviews. 149: 18-33.

Schwarz, D., Vontobel, P., Lehmann, E.H., Meyer, C.A., Bongartz, G. (2005) Neutron tomography of internal structures of vertebrate remains: a comparison with X-ray computed

tomography. Palaeontologia Electornica. 8(2): 11p.

Shtober-Zisu, N., Schwarcz, H.P., Konyer, N., Chow, T., Noseworthy, M.D. (2012) Macroholes in stalagmites and the search for lost water. Journal of Geophysical Research. 117: F03020.

Shtober-Zisu, N., Schwarcz, H.P., Chow, T., Omelon, C.R., Southam, G. (2014) Caves in caves: evolution of post-depositional macroholes in stalagmites. International Journal of Speleology. 43(3): 323-334.

Tremaine, D.M., Froelich, P.N., Wang, Y. (2011) Speleothem calcite farmed in situ: modern calibration of δ18O and δ13C paleoclimate proxies in a continuously-monitored natural cave system. Geochimica et Cosmochimica Acta. 75(17): 4929-4950.

Tumlison, L. G., Liu, H., Silk, W.K., Hopmans, J.W. (2007) Thermal neutron computed tomography of soil water and plant roots. Soil Physics. 72(5): 1234-1242.

Vacco, D.A., Clark, P.U., Mix, A.C., Cheng, H., Edwards, R.L. (2005) A speleothem record of Younger Dryas cooling, Klamath Mountains, Oregon, USA. Quaternary Research. 64(2): 249-256.

Vogel, N., Brennwald, M.S., Fleitmann, D., Wieler, R., Maden, C., Susli, A., Kipfer, R. (2013) A combined vacuum crushing and sieving (CVCS) system designed to determine noble gas paleotemperatures from stalagmite samples. Geochemistry, Geophysics, Geosystems. 14:2432-2444.

Vlassenbroeck, J., Dierick, M., Masschaele, B., Cnudde, V., Van Hoorebeke, L., Jacobs, P. (2007) Software tools for quantification of X-ray microtomography at the UGCT. Nuclear Inst. Meth. Physics Res. Section A: Accelerators, Spectrometers, Detectors Assoc. Equip. 580(1): 442–445.

Walczak, I.W., Baldini, J.U.L., Baldini, L., McDermott, F., Marsden, S., Standish, C.D., et al.

(2015) Reconstructing high-resolution climate using CT scanning of unsectioned stalagmites: A case study identifying the mid-Holocene onset of the Mediterranean climate in southern Iberia. Quaternary Science Reviews. 127: 117-128.

Wagner, J.D.M., Cole, J.E., Beck, J.W., Patchett, P.J., Henderson, G.M., Barnet, H.R. (2010) Moisture variability in the southwestern United States linked to abrupt glacial climate change. Nature geoscience. 3:110-113.

Wilding, M., Lesher, C.E., Shields, K. (2005) Application of neutron computed tomography in the geosciences. Nuclear Instruments and Methods in Physics Research. 542(1-3): 290-295.

Wong, C.I., Banner, J.L. (2010) Response of cave air CO2 and drip water to brush clearing in central Texas: implications for recharge and soil CO2 dynamics. Journal of Geophysical Research: Biogeosciences. 115: G4.

Wong, C.I. and Breecker, D.O. (2015) Advancements in the use of speleothems as climate archives. Quaternary Science Reviews. 127: 1-18.

Wortham, B.E., Montañez, I.P., Swart, P.K. (2017) Fossilized drip-water from a Sierra Nevada Cave reveals changing conditions over the North Pacific during the last deglaciation. GSA Annual Meeting, Seattle, WA. Abstract ID: 196-4.

Zhang, D., Zhang, P., Sang, W., Cheng, H., Wu, X, Yuan, Y., et al. (2010) Implications of stalagmite density for past climate change: an example from stalagmite growth during the last deglaciation from Wanxiang Cave, western Loess Plateau. Chinese Science Bulletin. 55(34):

3936-3943.

7. *Supplemental Material*

Introduction

The supplementary material introduced here provides additional information on data visualization techniques (Supp. Fig. 1) and statistical testing (Supp. Fig. 2) that may be helpful for the community.

Text S1. *Details of XCT scanning*

For the medium-resolution scan on the InveonMM the stalagmite was imaged in three sections that were subsequently stitched together. X-ray voltage was set to 80kV and the anode current was 425 μAmp. To filter the soft x-rays, a 1.5mm aluminum filter was used. The CT source to center distance was 267.34cm and the source to detector was 344.24cm. 720 projections were obtained by rotating the gantry through 360 degrees with each projection taking 1.3s. Each bed position resulted in a reconstructed image with a matrix of 512x512x512 and an isotropic voxel size of 193 μm. The stalagmite was mounted on the sample stage positioned upright by florist foam in a plastic bin, which does not affect x-ray or neutron attenuation. Scan parameters were adjusted based on the manufacturers recommended guidelines for using the Flat Panel Detector in order to achieve the best spatial resolution. The source and detector distances were set at 215.5 mm and 116 mm, respectively. Optimal x-ray filtration was determined by selecting among one of 13 proprietary filters. In this study, a HE16 filter was used given the dense nature of the sample. Optimal voltage and power settings were determined for contrast and throughput considerations (140kV and 10W or 71mAmp). A total of 4201 projections over 360

degrees were obtained with 9 seconds per projection.

Text S2. ***Uncertainty in NCT and XCT scanning***

Uncertainty exists in coupled NCT—XCT reconstructions based on the corrections inherent in the reconstruction software. One source of uncertainty in NCT scanning is multiple scattering due to high-water content (Tumlison et al., 2007). The water content in ML-1 was below the threshold for scattering effects (> 1 cm^3 of pure water), thus minimizing this influence (Schwarz et al., 2005; Tumlison et al., 2007). Systematic uncertainty in the detectors for NCT and XCT scanning are corrected for by using a standard flat-field correction that corrects for the different amounts of signal from a detector for a given input. A beam-hardening correction was used in XCT scanning to account for attenuation of the beams due to density changes. Artifacts due to density change (i.e. from pore space to solid calcite) along the path of attenuation can occur when scanning objects that have large differences in density. The lack of anomalous bright spots and distortions in the XCT image (Fig. 1) suggest that these artifacts are not present. A bright region in the NCT scan, proximal to the top of ML-1 (Fig. 2) that is inconsistent with our ability to find water in this region is interpreted to be a scanning artifact, likely an edge effect. Such artifacts were not included in the analysis of FID.

Text S3. ***Data Visualization***

The XCT and NCT scans were converted to gray-scale time series of (1) X-ray and (2) neutron attenuation as proxies of calcite density and FID, respectively using the ImageJ software package (Abramoff et al., 2004) and assigning a value based on the relative intensity of each voxel. Higher voxel intensity corresponds to brighter voxels in the image. The voxel intensity was converted to a time-series using the depths of each voxel in the scan and the initial 10 U/Th dates from ML-1 (Oster et al., 2015). An age-depth model for each proxy considered here was

determined using the COPRA algorithm (Brietenbach et al, 2004) and the 10 U/Th dates previously published for ML-1. When calibrated to the age-depth model for ML-1, made using the COPRA algorithm (Brietenbach et al, 2004), the medium-resolution XCT and NCT scans have an average temporal resolution of ~10 years.

Text S4. ***Statistical testing***

Spearman's rank coefficients were calculated for the proxy time series to evaluate temporal relationships and the degree of correlation between FID, calcite density and fabric, and $\delta^{18}O_{cc}$ and $\delta^{13}C_{cc}$ (Table 1). Spearman's rank coefficients are a nonparametric calculation of the monotonic, but not necessarily linear, relationship between variables that is used to determine the strength and direction of a relationship between two parameters.

General additive modeling (GAM) was used to describe the statistical dependency of FID on the independent parameters of calcite density, fabric, and $\delta^{18}O_{cc}$ and to determine the dependence of calcite density on calcite fabric. GAM is useful when the relationship between two variables is complex and non-linear (Everitt and Hothorn, 2010) as is the case between the scanning proxies and the other geochemical and physical properties of ML-1.

Cross-wavelet analysis was used to assess the period of maximum relationship between FID and $\delta^{18}O_{cc}$. Cross-wavelet analysis transforms time series into time-frequency space and cross-correlates the transformed times series. We used the Matlab package XWT (Grinsted et al., 2004) to perform the cross-wavelet analysis on FID and $\delta^{18}O_{cc}$ timeseries and assessed the significance and phasing of the relationship between FID and $\delta^{18}O_{cc}$ at a range of periods from

the sub-annual to centennial scale.

8. *Supplementary Figures*

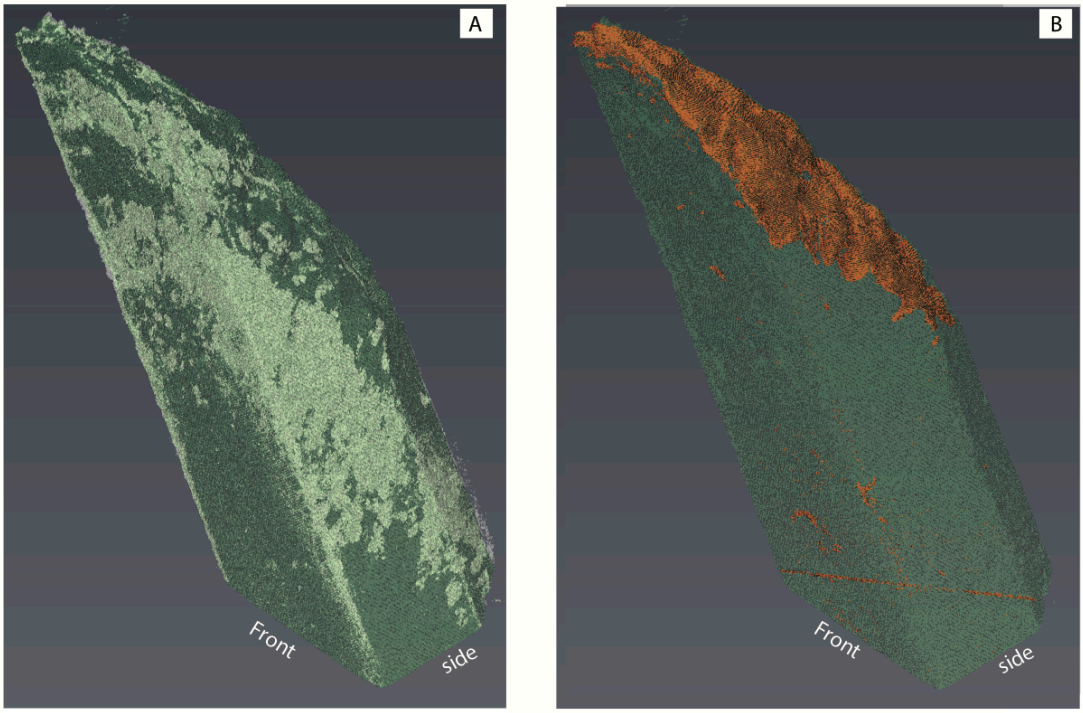

Figure S1. Three-dimensional rendering of NCT scans of stalagmite ML-1. (a) Air-filled macro-pores (gray) are concentrated along two bands in the center and top portion of the stalagmite. (b) Highest intensity voxels (orange) concentrated near the upper surface of the stalagmite are interpreted as edge effects and voxels proximal to the growth axis are interpreted as water filled

macro-pores.

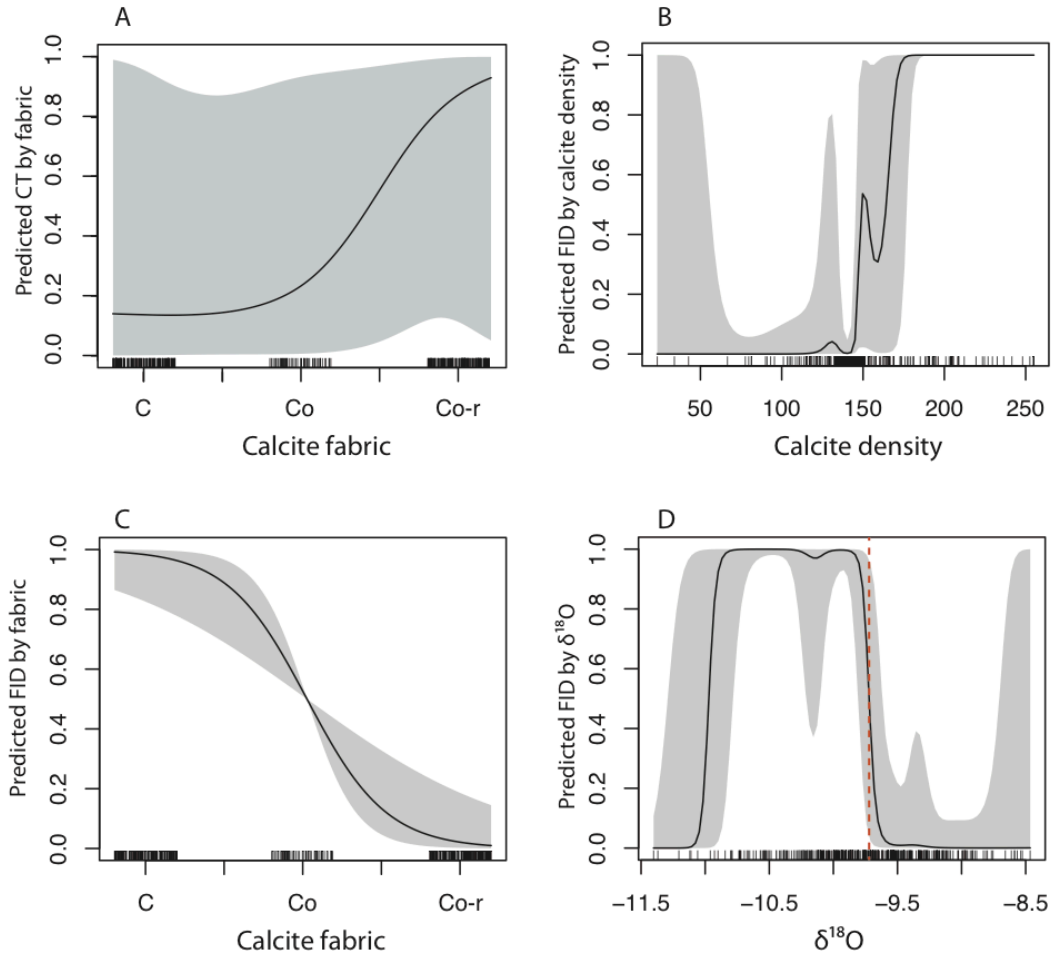

Figure S2*:* Predictability models for the ML-1 stalagmite proxy time series. These models assess the ability of the variability observed in one proxy record represented by the x-axis to predict the variability in the second proxy record (y-axis). Predictability is indicated as a fraction on the y-axis. Ability of calcite fabric to predict calcite density (A), and the ability of calcite density (B), calcite fabric (C), and $\delta^{18}O_{cc}$ (D) to predict the inferred variability in FID. Gray shading indicates confidence intervals based on the data denisty (black ticks on x-axis). Predictabilty is highest for high density, compact calcite and for calcite with $\delta^{18}O \leq -9.7$.

Chapter 2. A 5 °C cooling in Western Sierra Nevada, California, recorded in stalagmite noble gas concentrations during the Last Glacial Maximum

This chapter was reproduced from a manuscript in revision: Wortham, B.E., Mukhopadhyay, S.,

Montañez, I.P., Middleton, J., Tyra, A. In revision. Western Sierra Nevada Temperature During the Last Glacial Maximum from stalagmite noble gas concentrations. *Earth and Planetary Science Letters.*

Abstract

The climate of California, which is a drought-prone region in the southwestern U.S., is likely sensitive to future anthropogenic warming. The development of high-fidelity records of climate variability during periods of changing Northern Hemisphere temperature is essential to understand how California's climate will respond to future temperature changes. The record of deglacial warming in California over the past 20 ka is preserved in stalagmite calcite $\delta^{18}O$ time series. Accurately reading the $\delta^{18}O$ time series has proven to be challenging as, in addition to temperature, calcite $\delta^{18}O$ records from California are also influenced by precipitation source region. Noble gases dissolved in water hosted within inclusions in stalagmites can provide an independent estimate of temperature, which in turn permits correction for the influence of temperature on calcite $\delta^{18}O$ values and thus, isolation of the precipitation signal. Here we present noble gas concentrations of water hosted inclusions within a stalagmite from a western Sierra Nevada foothill cave. We obtain a noble gas temperature from the Last Glacial period of 7.0 ± 1.7 °C (2σ), 5.2 ± 1.7 °C cooler than the modern mean annual air temperature in these cave systems. The temperature estimated in our study agrees with the reconstructed 5-7 °C terrestrial temperature variability from the Last Glacial to the present in the southwest U.S. The temperature change of 5.1°C accounts for 50% of the sub-centennial scale variability in stalagmite calcite $\delta^{18}O$ from California indicating that the range in calcite $\delta^{18}O$ in this stalagmite records the influence of major shifts in both temperature and precipitation source. Consequently, at least half of the sub-centennial $\delta^{18}O$ variability is recording precipitation source changes to

Californian hydroclimate through the last deglaciation.

1. Introduction

Many regional precipitation proxy records, such as lake highstand levels, glacier expansion, and lake sedimentological records, document a wetter and colder southwestern U.S. during Northern Hemisphere cool stadials (Allen and Anderson, 2000; Owen et al., 2003; Quade and Broecker, 2009; McGee et al., 2012; Street et al., 2012; Broecker and Putnam, 2013; Munroe and Laabs, 2013). High-resolution stalagmite records from the southwestern U.S. and the central Sierra Nevada further support a wetter hydroclimate during cool periods through the last deglaciation (e.g. Oster et al., 2009; 2012; 2014; 2015; Wagner et al., 2010; Asmerom et al., 2010; Kirby et al., 2013; Lachniet et al., 2014). Conversely, some lake highstands indicate a drier climate during cool periods over the last 20 ka (Bacon et al., 2006; Benson et al., 2013). Understanding the drivers of millennial-scale hydroclimate variability from the oxygen isotopic composition ($\delta^{18}O$) of stalagmites, a proxy widely used for terrestrial paleoclimate reconstructions, is challenging due to multiple climatic factors influencing stalagmite $\delta^{18}O$ (e.g. McDermott, 2004). Temporal shifts in stalagmite $\delta^{18}O$ from the southwestern U.S. have been previously inferred to record variability in temperature (Vacco et al., 2005; Ersek et al., 2012), a combination of temperature and precipitation source (e.g. Oster et al., 2012; 2015; Lachniet et al., 2014), both temperature and seasonality of precipitation (Asmerom et al., 2010), and aridity (Wagner et al., 2010). An independent co-located temperature record is required in order to deconvolve the influence of precipitation and/or moisture source(s) from temperature on stalagmite $\delta^{18}O$.

Noble gas measurements of fluids entombed in stalagmites as inclusions provide an

opportunity for obtaining independent temperature records (Kluge et al., 2008; Scheidegger et al., 2010; 2011; Vogel et al., 2013; Brennwald et al., 2013; Ghadiri et al, 2018). Noble gas solubility in freshwater systems is primarily controlled by temperature (Aeschbach-Hertig et al., 1999; 2000; Kipfer et al., 2002), and water in equilibrium with the atmosphere (i.e., cave dripwater) is often archived in stalagmites as fluid inclusions contemporaneous with the calcite laminae in which they are trapped (e.g. Schwarcz, 1976; Wortham et al. 2019). The abundances of noble gases dissolved in the fluid filling inclusions hosted in stalagmites can yield cave air temperatures in ideal conditions (Kluge et al., 2008; Scheidegger et al., 2010; 2011; Vogel et al., 2013; Meckler et al., 2015; Ghadiri et al., 2018). The process of developing noble gas temperatures is crucial due to the difficulty of determining temperature change, independent of precipitation variability, in many archives (e.g. McDermott 2004; Wong and Breecker, 2015). Studies have noted the ability of noble gas temperatures developed from stalagmites in the Holocene and modern to reflect cave air temperature at the time of growth (Scheidegger et al., 2011; Vogel et al., 2013), which reflects mean annual temperature in the region (e.g. Brennwald et al., 2013). Consequently, noble gas temperatures developed from stalagmites are often considered faithful recorders of mean annual temperature at that site (Kluge et al., 2008; Scheidegger et al., 2010; 2011; Vogel et al., 2013; Meckler et al., 2015; Ghadiri et al., 2018) and can be compared to modern cave air temperature (Kluge et al., 2008; Ghadiri et al., 2018).

In the perfect scenario, researchers would isolate the noble gases solely from the water that was equilibrated with air (air-saturated water; ASW) before being sealed in a stalagmite crystal lattice to develop a noble gas temperature (NGT). Stalagmite inclusions, however, are typically filled with both ASW and air, limiting the ability to develop NGTs on bulk samples (Kluge et al., 2008; Scheidegger et al., 2010; 2011; Vogel et al., 2013). To address this problem,

some studies pre-crush their samples under vacuum (Scheidegger et al., 2010; Vogel et al., 2013) or in a helium atmosphere (Scheidegger et al., 2011) to a grain size of 200-400 μm in order to reduce the influence of trapped air on noble gas concentrations. Previous attempts to crush a sample 2-3 times in vacuum or in helium to isolate the fluid-only inclusions resulted in noble gas concentrations that were sometimes inconsistent with a two-component mixture of ASW and air (Scheidegger et al., 2010). Here, we investigated a different methodology for measuring noble gas abundances in speleothems that involves first identifying the three-dimensional distribution of fluid- and/or air-filled inclusions in the stalagmite (Wortham et al., 2019) and subsequently targeting noble gases measurements in the regions rich in fluid-filled inclusions with a progressive step-crushing technique. The progressive step-crushing technique has been successful in deconvolving air contamination from mantle noble gases in basalts (e.g. Peron and Moreira, 2018; Parai et al., 2019). Our approach allows for the development of a stalagmite-based NGT for the Last Glacial period (LG) in a central Sierra Nevada cave (Fig. 1; Oster et al., 2015). We compare the NGT from this study to an average cave air temperature from a modern 5-year monitoring study of a central Sierra Nevada cave (Oster et al., 2012). The calculated temperature change between the NGT and the modern cave air temperature is consistent with other proxies of Northern Pacific temperature change from the LG to the present-day ("LG-PD temperature differential"). We use the LG-PD temperature differential to assess the magnitude of observed calcite $\delta^{18}O$ variability attributable to temperature and show that the calcite $\delta^{18}O$ time series must additionally record variability in precipitation patterns since the Last Glacial Maximum.

2. Hydrologic context

For this study, we use a previously studied stalagmite (ML-1) from McLean's Cave (Oster et al., 2014; 2015; Wortham et al., 2019). McLean's cave formed in the metamorphosed carbonate (marble) lens of the Calaveras Complex. The entrance to McLean's Cave lies at 300 m above sea level and is currently submerged under the historic height of the New Melones Reservoir (Fig. 1). The average climate over McLean's Cave is characterized by cool, wet winters and warm, dry summers. The majority of the rainfall occurs during the winter months (Oster et al., 2012; 2014; 2015). Complete descriptions of the cave system and local climate can be found in Oster et al. (2014).

The construction of the New Melones Dam and Reservoir completed in 1980 prohibits cave monitoring at McLean's Cave. Here we use a 5-year monitoring study of Black Chasm Cavern (Oster et al., 2012) to calibrate stalagmite records from McLean's Cave given that Black Chasm has a similar geometry and is 45 km to the northwest of McLean's Cave. Black Chasm Cavern ventilates in the cold winter months with a corresponding increase in drip-rate in response to higher precipitation amounts. The cave air temperature in the back-most part of Black Chasm varied from 10.3 to 14.3 °C over the monitoring period, with a mean annual temperature of 12.3 ± 0.4 (2 SE) °C (Oster et al., 2012). The temperatures recorded are for the cooler and wetter months of the year when the stalagmites in California are growing. We use 12.3 °C as the present-day (PD) temperature for comparison in this study.

3. Methods

3.1 Stalagmite ML-1

Stalagmite ML-1 (24.5 cm) was previously sampled for U-Th age dating, development of stable isotope and trace element time series (Oster et al., 2015; Fig. 1), and to assess the 3-Dimensional distribution of fluid inclusions (Wortham et al., 2019). The U-Th ages for ML-1

indicate that it spans 19.4 to 11.6 ka (Fig. 1). The distribution of fluid- and/or air-filled inclusions was determined using coupled x-ray and neutron computed tomography scanning (CT-scanning). Fluid-filled inclusions in ML-1 are micro-inclusions developed along crystal faces. We posit that micro-inclusions along crystal boundaries in ML-1 are likely not diagenetically altered as bands of alternating calcite fabric extend from the growth axis to the edges of the stalagmite. Furthermore, banding is not interrupted by large voids and there are no voids or regions in the stalagmite in which one crystal fabric replaces another (Oster et al., 2015; Wortham et al., 2019). A fluid-rich region capturing the LG (Sample 2A) was identified using x-ray and neutron CT scanning, and has an age of 18.8 ± 0.3 ka. The sample was removed using a razor blade from the back of a thin-section billet and was 0.5 cm long (along the growth axis) by 0.5 cm (depth) by 1 cm (width).

3.2 Noble gas and water measurements in ML-1 stalagmite

A single piece of sample 2A weighing 3.8 grams was enclosed between two tungsten carbide discs and loaded into a crushing chamber in the newly designed sampling line (Fig. 2). The sample and line were pumped under vacuum for 2 days and then baked at 60 °C for 24 hours. Following this, the sample chamber was pumped for two weeks until blanks were low and stable. To release water and noble gases, the sample was progressively step-crushed seven times in-vacuo using a hydraulic ram. The piston on the hydraulic ram pressed down onto the top conflat flange of the crusher, which has a steel rod welded into it, on the ultra-high vacuum side, that in turn pressed down onto the tungsten carbide disc crushing the sample (Table 2, Fig. 2) (e.g., Parai et al., 2019). We performed seven in-vacuo step-crushes on the single piece of speleothem sample, already identified to contain water-filled inclusions (section 3.1), in an attempt to extract the air-, or

fractionated air-contaminated inclusions in the initial steps and increase the relative concentration of noble gases associated with ASW inclusions in the later crushing steps. This progressive step-crushing approach is demonstrably successful in analyses of mantle-derived gases from basaltic glass samples (e.g. Peron and Moreira, 2018; Parai et al., 2019), which contain ubiquitous shallow-level air, or fractionated air components, because the shallow-level air component is preferentially released in the earlier steps when crushing a single piece of glass..

Pressure readings from a manometer exposed to the crusher volume were used to monitor and control the amount of gases released during each step-crush. After the step-crush, the released water vapor is frozen onto the two bare-metal U-shaped cold traps in series by immersing them in a liquid nitrogen-methanol slush that is kept at a temperature of 175-180 K (Fig. 2). The remaining gases are inlet into the noble gas processing line and sequentially exposed to a hot and cold getter to remove the active gases. Ne, Ar, Kr and Xe were subsequently frozen onto a cryogenic cold finger at 32K and He was pumped away. Ne, Ar, Kr and Xe were sequentially released from the cryogenic trap into the mass spectrometer. Ne, Kr, and Xe abundances were measured on the Nu Noblesse mass spectrometer and Ar was measured using a SRS 200 RGA quadrupole mass spectrometer. Abundances in the ML-1 sample were determined with peak height comparisons to air standards (Parai et al., 2019). The procedural blank was 3.5×10^{-12} cc for Ne, 6.7×10^{-9} cc for Ar, 2.9×10^{-13} cc for Kr, and 3.9×10^{-14} cc for Xe. The uncertainty on noble gas abundances are based on the reproducibility of air standards of similar size to the measurements, the uncertainty on the pipetted amount of gases, and the blank measurements for each gas.

The crusher and the liquid nitrogen-methanol slush U-traps were isolated once the noble gases were frozen down onto the cryogenic cold trap in the noble gas processing line. The U-traps were

warmed to ~320 K in order to release water vapor into the 1000 cc expansion volume (Fig. 2; section 3.2) and the water vapor amount was measured manometrically using a 10 Torr MKS Model 626C capacitance manometer, which has an accuracy of 0.25% (Table 1).

3.3 Water Calibration

The amount of water released by crushing the stalagmite sample was measured manometrically in the vacuum line in the UC Davis Noble Gas Laboratory (Fig. 2). A calibration of the stalagmite processing line was originally performed by inserting known amounts of water into copper capsules, which were then cold-sealed by crimping (Sander et al., 2014) and loaded in the crushing chamber. Crushing the copper capsules, produced a linear relationship between the amount of water in the capsule and the manometer reading but with significant scatter, likely reflecting water loss from the capsules resulting from imperfect sealing of the capsule. To reduce uncertainty in the calibration, we changed our approach and sealed known amounts of water in glass capillaries following Kluge et al. (2008), which reduced the uncertainty in the calibration through reduction in scatter of the data points (Fig 3). Uncertainty on the fit between the known amounts of water in the glass capillaries and the manometric reading (Fig. 3) was assessed by bootstrapping the individual measurements and was determined to be 3.0 % (2σ) (Fig. 3), similar to other uncertainties reported in the literature (Kluge et al., 2008). The vapor pressure measured in the stalagmite crushes were converted to μL of water based on the water calibration (Fig. 3) and the uncertainty of 3.0 % (2σ) was applied to all manometric water amount measurements.

4. Results

4.1 Noble Gas Elemental Ratios

The noble gas amounts and elemental ratios are reported in Table 1. In some studies, neon abundances in stalagmites are not used for estimating NGTs (Kluge et al., 2008; Scheidegger et al., 2010; 2011; Brennwald et al., 2013; Vogel et al., 2013). Ne concentrations in these studies leads to spurious results in some cases, most likely due to excess neon trapped in the crystal lattice (e.g., Vogel et al. 2013). In some stalagmite samples, however, neon abundances do place constraints on NGTs (Ghadiri et al., 2018). The Ne/Xe ratios from stalagmite ML-1 do not overlap at the 2σ level with the ASW-Air mixing line and the Ne/Xe ratios are consistent with excess Ne present in the sample (Supp. Fig. 2). Due to the recognized difficulty of interpreting fluid inclusion Ne, and the findings in stalagmite ML-1, Ne is not considered in this study.

Stalagmites include both water-filled and air-filled inclusions; thus, mixing between the ASW endmember and pure air is expected. Furthermore, pure water samples, which are not affected by partial re-equilibration or diffusion, will plot within uncertainty of the calculated ASW endmember for the temperature at which they formed (Brennwald et al., 2013). A reduction of the influence of air during the extraction method or in the final calculation of temperature is necessary to determine an accurate temperature of formation (Kluge et al., 2008; Scheidegger et al., 2010; 2011; Brennwald et al., 2013; Vogel et al., 2013; Kluge et al., 2014). The amount of air per unit mass of water in the different steps ranged from 0.019 to 0.055 cc STP/g, which is within the range of 0.002 to 0.15 cc STP/g in previous studies where NGTs from speleothem could be accurately determined (e.g., Kluge et al., 2008; Scheidegger et al., 2011; Ghadiri et al., 2018; Vogel et al., 2013).

The first two step-crushes (open white circles; Fig 4) clearly do not overlap with the Air-ASW mixing line and are closer to the Air end-member compared to the subsequent step-crushes. Step-

crushing data that fall below the mixing line may potentially result from an excess of grain-surface adsorbed heavy noble gases with preferential excess of Xe over Ar and Kr. The subsequent five step-crushes from the sample produce Ar/Xe and Kr/Xe ratios that all plot together clustering close to the ASW component (filled black circles, Fig. 4).. The range of Kr/Xe and Ar/Xe in the replicate analysis of sample 2A from this study is similar to previous speleothem NGT studies that measure replicate samples (of varying grain size) (Vogel et al., 2013; Ghadiri et al., 2018). Furthermore, samples from another study (Ghadiri et al., 2018) that span the Last Glacial period indicate a similar amount of scatter around the air-saturated water (ASW) endmember as is represented by the noble gas ratios in sample 2A from this study.

4.2 Paleo-temperature from the LG

The noble-gas derived paleotemperature was calculated from the five step crushes that plot close to the ASW component. We rejected step crushes 1 and 2 because of the deviation from the Air-ASW mixing line for these two steps (section 4.1; Fig. 4) and because of their larger atmospheric contributions. To determine the NGT from the speleothem data, we modelled the observed noble-gas data in the five steps as a binary mixture of ASW and air as described by Ghadiri et al. (2018). The model was then fitted to the total amount of noble gases and water extracted from the speleothem sample in crushes 3 through 7 by error-weighted least-squares regression using the NOBLEFIT software (http://brennmat.github.io/noblefit). The inputs to the NOBLEFIT model included the noble gas abundances, the calibrated water amounts, and the associated 1σ uncertainties. This software tool calculates the NGT and also yields the $\chi 2$ statistic of the regression that indicates the goodness of the model fit to the data. The fit results obtained from the measurements of each step-crush are listed in Table 2. We computed an error weighted

mean using a simple bootstrap that yielded a mean temperature estimate of 7.3 ± 2.3 (2σ) °C (Supp. Fig. 1).

The noble-gas derived paleotemperature was also derived by summing the noble gas and water abundances from crush 3 through crush 7 with the uncertainties added in quadrature (Table 1). The rational for summing the abundance data for these five steps are the observations that they overlap with each other in their elemental abundance pattern and plot close to the ASW end-member, suggesting sampling of the same population of inclusions, or sampling similar proportions of ASW inclusions and air-contaminated inclusions (Fig 4). Using NOBLEFIT, we computed a temperature from the summed noble gas and water abundances (Table 2) that yielded a NGT of 7.0 ± 1.7 °C (2σ) (Table 2) at 18.8 ± 0.3 ka for McLean's cave. The temperature from the summed abundance data is identical to the error weighted mean temperature determined above (see also Table 2). For the purposes of this study, we use 7.0 ± 1.7 °C as the temperature at 18.8 ± 0.3 ka in the central Sierra Nevada. The uncertainty of the NGT from the Sierra Nevada is similar to, or slightly reduced, compared to previous NGT determinations from speleothems (e.g. Ghadiri et al., 2018). Although we have studied one speleothem sample, we suggest that mapping out fluid-inclusion rich zones with CT and neutron scans, followed by a sizeable number of progressive in-vacuo step-crushes of a single large fluid inclusion-rich piece, is a promising technique for estimating NGTs.

5. Discussion

We show that combining coupled CT-scans with in-line progressive crushing is a promising technique in producing high precision noble gas temperature estimates from stalagmite fluid inclusions. The NGT of 7.0 ± 1.7 °C (2σ) for the Last Glacial period (LG) represents the mean

annual temperature in the western Sierra Nevada foothills at 18.8 ± 0.3 ka. Moreover, the inclusion-based NGT for the LG period allows for isolation of the temperature influence on stalagmite $\delta^{18}O$ that has confounded the paleoenvironmental interpretation of $\delta^{18}O$ time series in previous studies. The magnitude of $\delta^{18}O$ variability in ML-1 is larger than can be explained by the observed temperature shift, indicating that precipitation variability occurred synchronously with surface air temperature change during the last deglaciation.

5.1 Temperatures during the Last Glacial period

The temperature determined from Sample 2A indicates that the central Sierra Nevada was 7.0 ± 1.7 °C at 18.8 ka during the LG. The NGT from Sample 2A likely represents mean annual temperature in the Sierra Nevada because cave air temperatures, including those for the central Sierra Nevada caves (Oster et al., 2012; 2015), typically reflect mean annual air temperatures above the cave. In turn, the temperature recorded in the amount of noble gases rapidly diffused in cave water and archived as fluid inclusions represent the cave air temperature (Brennwald et al., 2013). In order to calculate a LG-PD temperature differential we compare the NGT from sample 2A to the average measured modern cave air temperature from Black Chasm Cavern of 12.3 ± 0.4 (2 SE) °C (Oster et al., 2012) and determine that the central Sierra Nevada was 5.2 ± 1.7 (2σ) °C colder in the LG than today.

The NGT for stalagmite ML-1 is in agreement with a recent continuous temperature record over the last deglaciation and with snap-shots of temperature change from the LG to PD (Figs. 5 and 6). A series of four pollen records from lakes 2500 km north in Beringia, Alaska (Viau et al., 2008; Shakun et al., 2012) are the most recent continuous record of terrestrial climate change available for Western North America. The Beringia records indicate an average of 3 °C cooler

temperatures at 18.8 ka (Viau et al., 2008). The temperature estimated in Beringia has a wide dispersion from 0.5 to 4.3 °C that, within uncertainty, agrees with the NGT presented here (Fig. 5). We note that the records from Beringia demonstrate a temperature minimum at ~17.5 to 17.9 ka of 4.5 °C, with the four records clustering closely together during this time period (Fig. 5). A temperature minimum in the Beringia record could suggest a similar minimum in central Sierra Nevada at 17.5 to 17.9 ka, such that the maximum LG-PD temperature differential was larger than the 5.2 ± 1.7 °C recorded by the ML-1 speleothem at 18.8 ka. However, three additional records from California suggest that this is an unlikely scenario. A pollen record from Clear Lake, California, ~200 miles NW of McLean's Cave, indicates an inferred temperature change of ~7-8 °C from LG to the present day (Adam and West, 1983). Variability of 7-8 °C is marginally higher than our temperature change of 5.2 ± 1.7 (2σ) °C (Fig. 6). The record from Clear Lake, California (Adam and West, 1983) suggests a constant temperature from the LG period to ~13 ka and does not indicate a temperature minimum between 17 and 18 ka in contrast to the Beringia Lake records from Alaska (Fig. 5). In both the Beringia and Clear Lake studies, the uncertainty for the temperature estimates based on pollen was not stated. In San Diego, California, a temperature time-series was reconstructed using noble gas abundances from groundwater that demonstrates an LG-PD temperature differential of 6.2 ± 1.2 °C (±2 SE) and a constant temperature until ~15 ka (Seltzer et al., 2019) (Fig. 6). Additionally, a clumped isotope temperature from Lake Surprise, California indicates a LG-PD temperature differential of 4.7 ± 2.2 (2σ) °C (Santi et al., 2020) and indicates a consistent temperature through the beginning of the LG with a minimum near 15 ka. Comparison of the timing of temperature variability in pollen records from Alaska and temperature reconstructions from California may indicate that cooling occurred after 18.8 in Alaska but not in California. However, pollen records are interpreted in a framework of both precipitation and

temperature change and this convolved signal could result in apparent variability in the records that is not due to temperature alone. Understanding of the temporal and spatial variability in terrestrial temperature during the deglaciation necessitates further development of stalagmite NGTs from both within stalagmite ML-1 and along the Pacific Coast.

Other regional and global records provide snapshots of inferred and quantitative temperature change from the LG to the PD (Fig. 6). Globally, several studies measuring the noble gas concentrations in groundwater provide temperatures from the LG period in San Diego, California (Selzer et al., 2019), New Mexico (Stute et al., 1995a), Texas (Stute et al., 1992), Michigan (Ma et al., 2004), Brazil (Stute et al., 1995b), northern Africa (Edmunds et al., 2009), Oman (Weyhenmeyer et al., 2000) and Europe (Beyere et al., 1998; Edmunds et al., 2004). The global NGT's indicate cooler terrestrial temperatures of 5-7°C during the LG period. These global and regional temperature estimates are in excellent agreement with the NGT from stalagmite ML-1 (Fig. 6).

Global modeling of temperature variability from the LG to PD (Braconnot et al., 2007) agrees with the NGT determination from this study (Fig. 7). A comparison of temperature variability across models is possible through the Paleoclimate Model Intercomparison Project (PMIP) phase 2 (PMIP2; Braconnot et al., 2007). In this phase of the PMIP project (PMIP2), ocean-atmosphere simulations were run at LG and mid-Holocene benchmarks. The northern hemisphere temperature variability of the PMIP2 models between the LG period and the mid-Holocene ranges from -4 to -7 °C (Braconnot et al., 2007; Fig. 7). The range in the PMIP2 comparison agrees with the NGT from this study of 5.2 ± 1.7 °C (Fig. 7).

5.2 NGT constraints on hydroclimate variability

Estimates of the LG-PD temperature difference provides the opportunity to constrain hydroclimate variability recorded in $\delta^{18}O$ time series from stalagmite ML-1 (Oster et al., 2015). The time-series of $\delta^{18}O$ in stalagmite ML-1 has a minimum value between 19 and 18 ka, increases at the end of the LG period with a maximum value at ~16.3 ka and slowly decreases to 12.7 ka (Oster et al., 2015). Within the stalagmite $\delta^{18}O$ record there are centennial scale cycles in calcite $\delta^{18}O$ with a magnitude of ~2.0 ‰ and a millennial-scale variability of ~1.2 ‰ (Oster et al., 2015). The calcite $\delta^{18}O$ variability was initially interpreted to represent both temperature and precipitation source fluctuations based on five years of precipitation and dripwater monitoring in Black Chasm Cavern (Oster et al., 2012; 2014; 2015). The $\delta^{18}O$ of modern precipitation in the western Sierra Nevada can vary substantially (by up to 10 ‰) due to the differences in precipitation $\delta^{18}O$ between North Pacific-sourced storms (-15.5 ± 0.4 ‰) and subtropical Pacific sourced storms (-6.4 ± 2.5 ‰; Oster et al., 2012). The variability in $\delta^{18}O$ of precipitation is translated quickly (~3 weeks) to the dripwater in Black Chasm Cavern with some mixing in the epikarst (Oster et al., 2012); therefore, interpretation of $\delta^{18}O$ variability in calcite is interpreted to reflect sustained changes in precipitation source. Temperature variability additionally imparts an influence on calcite $\delta^{18}O$ during the fractionation between water and calcite during stalagmite growth (e.g. McDermott, 2004). In order to isolate the signal of precipitation source variability from stalagmite ML-1, the temperature contribution to the $\delta^{18}O$ time series needs to be accounted for.

To estimate a maximum temperature correction for stalagmite $\delta^{18}O$ in central Sierra Nevada Cave, a fractionation factor of -0.177 ‰/°C (Tremaine et al., 2011) is applied to the LG-PD temperature deferential. Experimental (e.g. Kim and O'Neill, 1997) and stalagmite-based empirical (Vacco et al., 2005; Ersek et al., 2012) studies delineate a large range of temperature-

based $\delta^{18}O$ fractionation values. We use the fractionation factor defined by Tremaine et al. (2011) of -0.177 ‰/°C because the value agrees with several published studies in which modern calcite $\delta^{18}O$ and cave air temperature were simultaneously measured in a range of cave environments (Tremaine et al., 2011). We apply the fractionation factor of -0.177 ‰/°C to estimate the magnitude of $\delta^{18}O$ variability in the ML-1 time series that remains once the temperature effect of the LG-PD differential in the Sierra Nevada is accounted for (Fig. 8). The LG-PD temperature differential of 5.2 ± 1.7 (2σ) °C from this study indicates that a maximum of 0.9 ± 0.3 (2σ) ‰ of $\delta^{18}O$ change could occur between the LG and the PD (Fig. 8). The calcite $\delta^{18}O$ record in ML-1 only extends to 11.6 ka; therefore, the LG-PD temperature differential discussed here is not a direct comparison. However, in the Clear Lake, California (Adam and West, 1983) and Beringia, Alaska (Viau et al., 2008) records (Fig. 5) only half of the warming to the present day is completed by the Younger Dryas. Hence, the temperature contribution of 0.9 ± 0.3 (2σ) ‰ to the $\delta^{18}O$ variability in the ML-1 record is a firm upper limit. Consequently, the repeated centennial cycles of ~2.0 ‰ (Fig. 8) cannot be completely accounted for by temperature alone. We posit that the centennial scale variability in the stalagmite $\delta^{18}O$ record is influenced by precipitation source changes through the last deglaciation as well as temperature. Millennial scale variability is within the range of $\delta^{18}O$ variability that can be attributed to temperature but is complex as it does not show a trend consistent with temperature being the only driver (Fig. 8). Additional measurements of NGT's through the last deglaciation are needed to isolate temperature variability in the record.

Beyond temperature, changes in precipitation seasonality, source, and amount may induce a further ~1 ‰ variability in the calcite $\delta^{18}O$ of stalagmites in southwestern U.S. (Asmerom et al., 2010; Wagner et al., 2010; Oster et al., 2009; 2015; Lachniet et al., 2014). A sustained shift between North Pacific-sourced storms (-15.5 ± 0.4 ‰) and subtropical Pacific sourced storms (-

6.4 ± 2.5 ‰; Oster et al., 2012) on a millennial or centennial scale could shift the stalagmite $\delta^{18}O$ record by 1-2 ‰ given the 10 ‰ variability between the two sources. A shift in precipitation source is additionally recognized in stalagmite records from the Leviathan Cave chronology that result in lower stalagmite $\delta^{18}O$ values during periods of strengthening of North Pacific storm tracks (Lachniet et al., 2014). Given the framework of five years of cave monitoring in the central Sierra Nevada (Oster et al., 2012) and the quantitative temperature estimate from stalagmite ML-1, we suggest that there are centennial cycles in precipitation sources effecting California.

6. Conclusion

We present a new methodology of x-ray and neutron CT scanning combined with a progressive step-crushing technique to accurately and precisely measure the noble gas concentrations of fluid inclusions in stalagmites. Application of this method to a western Sierra Nevada stalagmite yields a NGT of 7.0 ± 1.7 °C during LG. The NGT-derived temperature shift is in line with both global and regional estimates of temperature change between the LG and present-day. Our quantitative temperature reconstruction for the western Sierra Nevada reveals that a sustained shift in precipitation patterns over the last deglaciation is necessary to explain the calcite $\delta^{18}O$ record from a stalagmite (ML-1) from a west-central foothill cave of the Sierra Nevada.

7. Figures

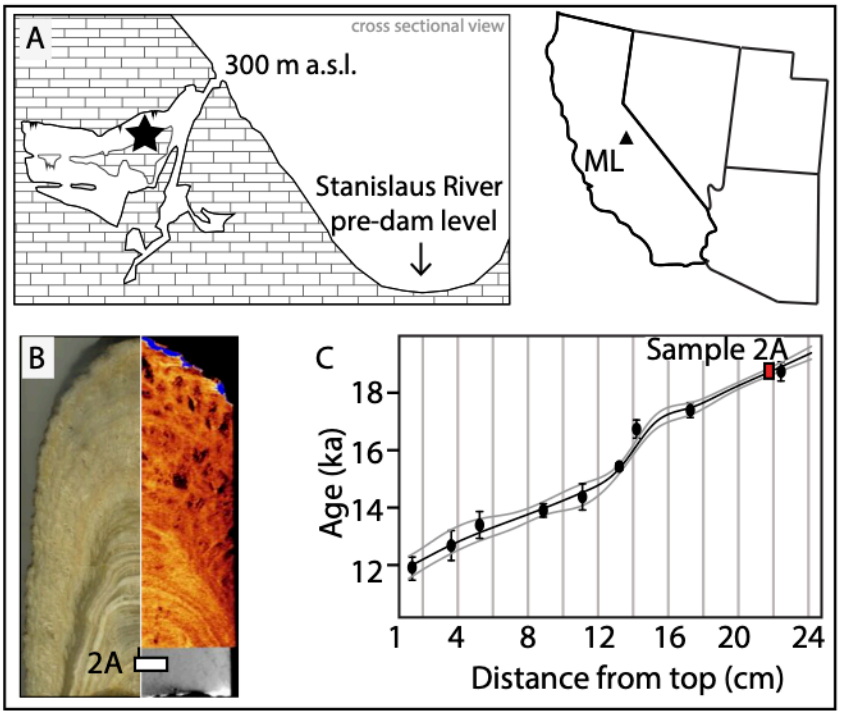

Figure 1: Location and age model for stalagmite ML-1 from McLean's Cave (Oster et al., 2015), west-central foothills of the Sierra Nevada, California. Cross-sectional view of McLean's Cave (A); brick pattern is marble (dolomite and calcite) bedrock and the pre-New Melones Dam level of the Stanislaus River is shown. (B) Stalagmite ML-1 shown in plain light and CT-scanned (Wortham et al., 2019) is 24.5 cm and grew from 19.4 to 11.6 ka based on 10 U/Th dates (C) (adapted from Oster et al., 2015). The sample used in this study (sample 2A) yields an age of 18.8 ± 0.3 ka (red box).

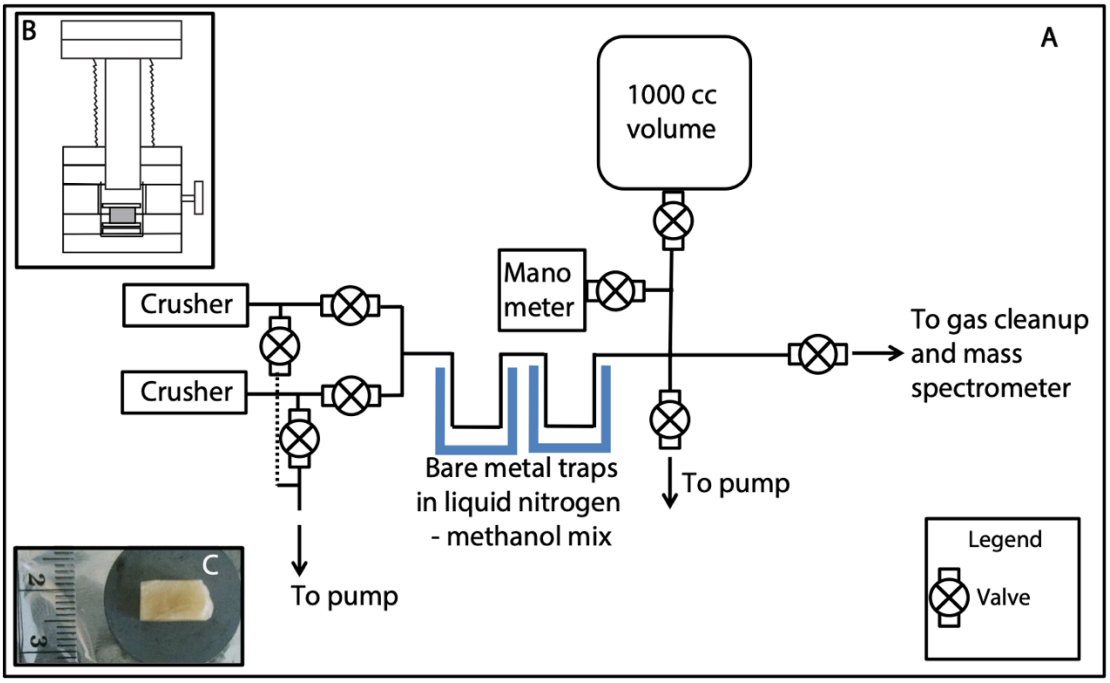

Figure 2: Schematic of the noble gas crushing line (A) that uses a crushing chamber (B) attached to a purification line to systematically crush stalagmite samples (C). Two cryogenic U-traps are used to isolate fluid-inclusion water. After the noble gases have been trapped on a cryogenic cold finger, the U-traps are warmed, releasing the water, which is expanded into the 1000 cc known volume. The water amount is then measured manometrically.

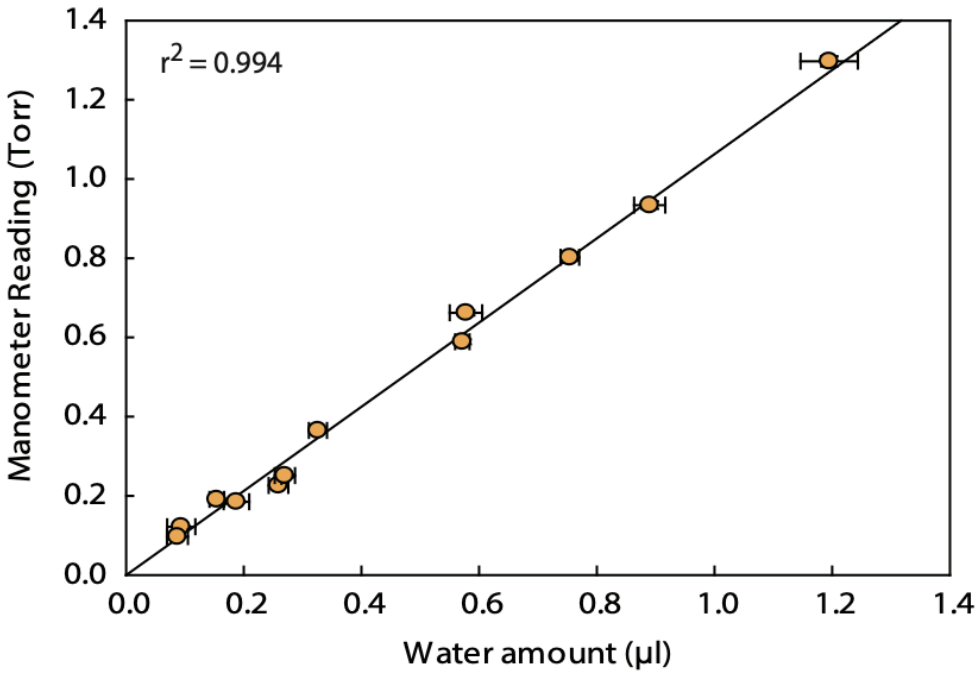

Figure 3: The water calibration for the crushing line system (Fig. 2). Known amounts of water (µL) were enclosed in glass vials, which were snapped open in the crushing line and measured manometrically (Torr). Error bars on yellow filled circles are 2 standard deviation of the average measured amounts of water, which was sealed in each of the glass vials.

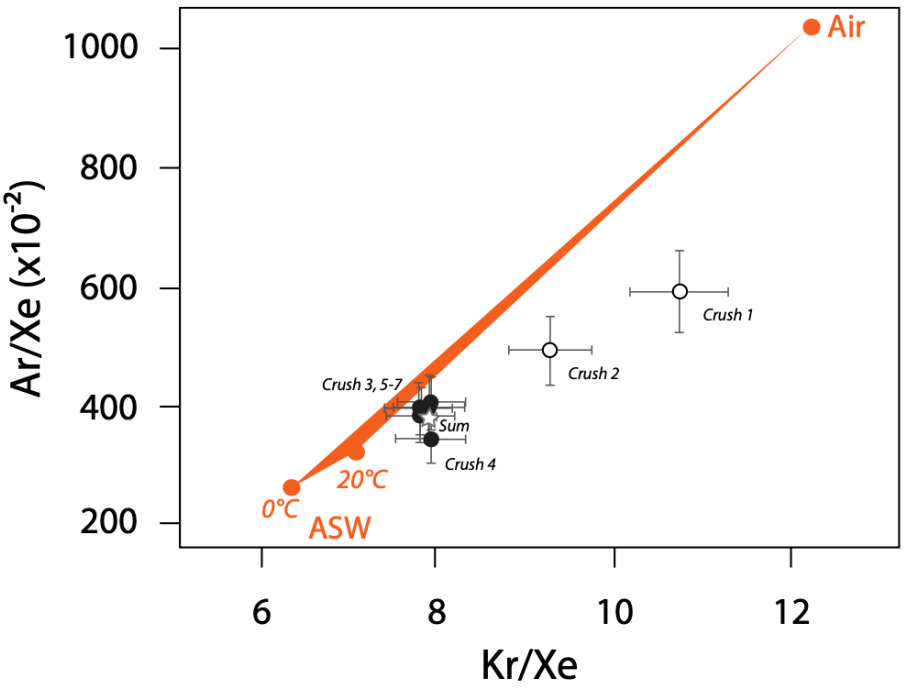

Figure 4. Noble gas elemental ratios (open and solid circles) for the seven step crushes for sample 2A. The sum of the last five step crushes (solid circles) is denoted by a star. Mixing triangle between the theoretical air-saturated water (ASW) values (orange circles) for 0 to 20 °C and air are shown. Three of the data points that do not overlap the mixing lines at the 2σ level (open and filled grey-circles) were not used for temperature reconstruction. Data closer to the ASW endmember indicates less contamination by air-filled inclusions within the stalagmite. ASW endmember calculated using Kipfer et al., 2002.

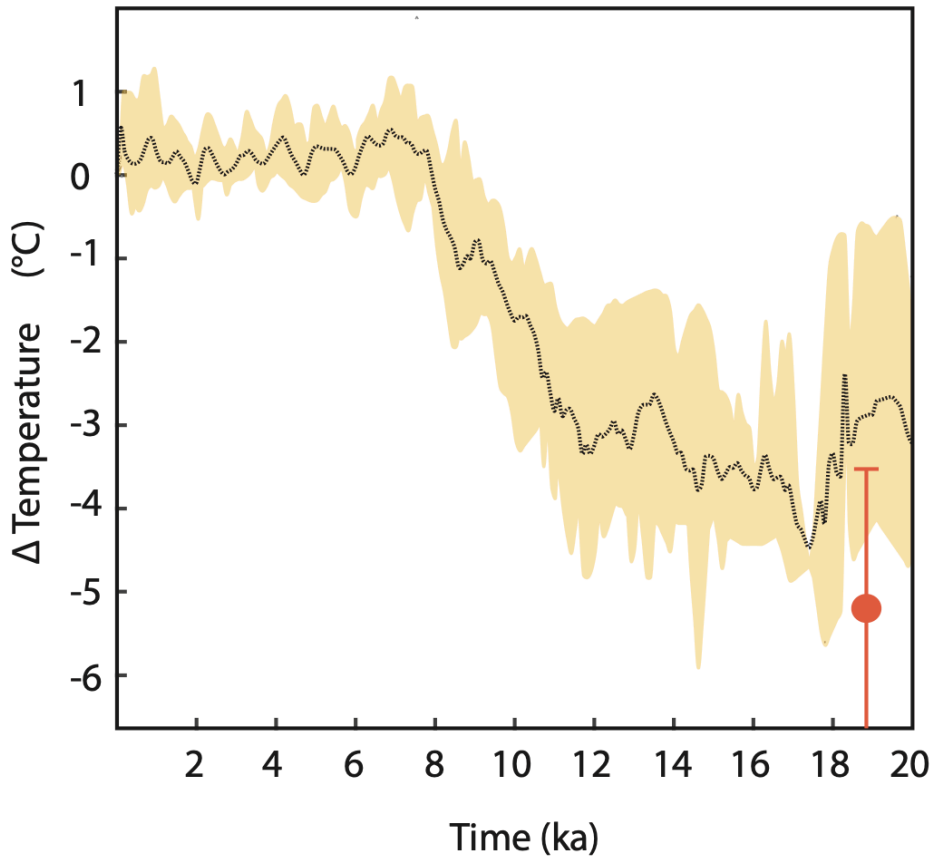

Figure 5: Range of temperature change (ΔTemperature) from the LG through the PD for four lake pollen records in Beringia (yellow shading; Viau et al., 2008) and the average change across the four records (black dashed line) compared to the NGT-computed mean annual surface temperature for stalagmite ML-1 (red symbol). Red-filled circle and vertical line are the average and uncertainty 2σ uncertainty for sample 2A (18.8 ± 0.3 ka) from ML-1, width of red circle represents uncertainty on age estimate.

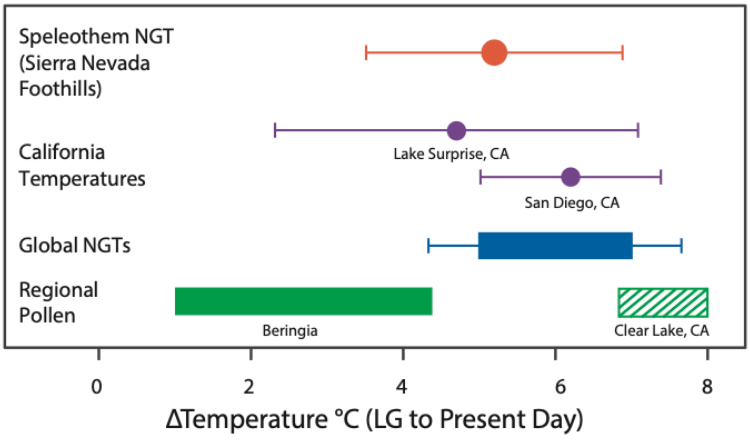

Figure 6: Comparison of the LG-PD temperature differential from this study (red symbol) to regional and global records: California quantitative temperatures (purple circles; Santi et al., 2020; Seltzer et al., 2019), global NGT's (navy blue rectangle; Stute et al., 1992; 1995a; 1995b; Beyere et al., 1998; Weyhenmeyer et al., 2000; Edmunds et al., 2004; 2009; Ma et al., 2004), Beringia Lake pollen records at 18 ka (green rectangle; Viau et al., 2008), Clear Lake (dashed green rectangle; Adam and West, 1983). All uncertainties are 2σ.

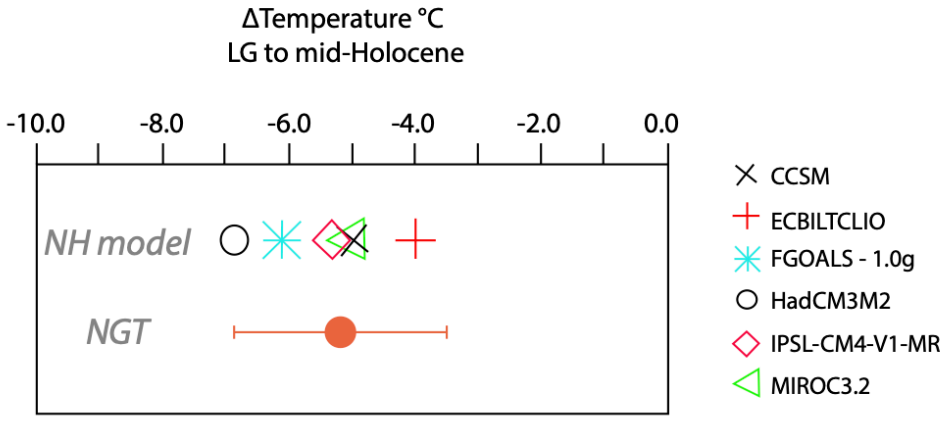

Figure 7: Comparison of model temperature change from the LG period to the mid-Holocene from PMIP2 (Braconnot et al., 2007) to the NGT from this study. The model temperature from 6 individual

models (open symbols; legend) show a range of -4 to -7 °C in the northern hemisphere in agreement with the NGT along with its 2σ uncertainty from this study (red circle). Adapted from Braconnot et al. (2007).

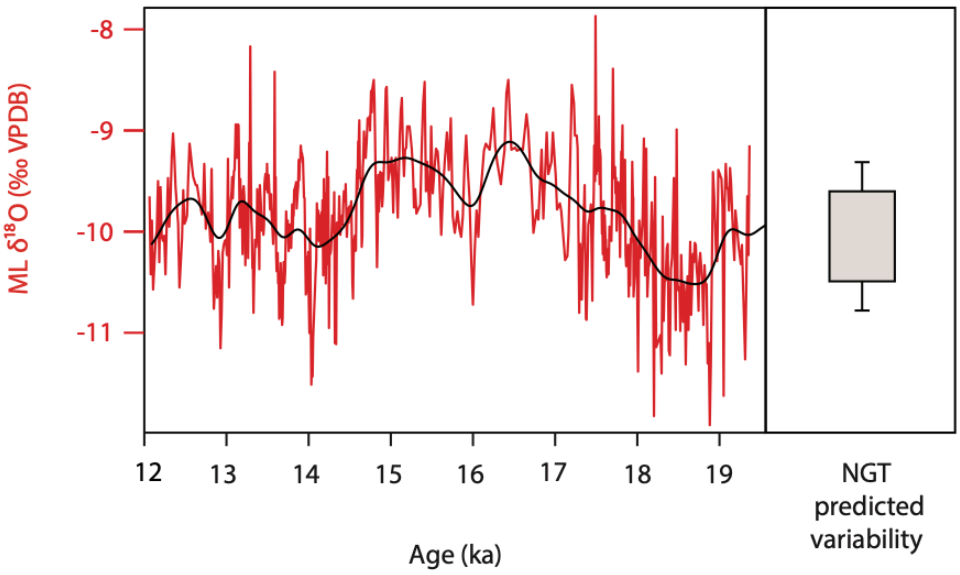

Figure 8: Time series of $\delta^{18}O$ from stalagmite ML-1 (red line) with kernel smoother (black line; Oster et al., 2015). The $\delta^{18}O$ time-series is interpreted to reflect precipitation source region and temperature variability through time (Oster et al., 2015). The temperature determined from this study could account for 0.9 ± 0.3 (2σ) ‰ of $\delta^{18}O$ change (grey bar).

8. *Tables*

Table 1. Noble gas and water abundance data from the step crushes in the ML-1 speleothem sample.

Crush Number	Ne (ccSTP)	± 2σ	Ar (ccSTP)	± 2σ	Kr (ccSTP)	± 2σ	Xe (ccSTP)	± 2σ	Water Mass (g)	± 2σ
1	2.63E-10	5.3E-12	1.01E-07	1.2E-08	1.91E-11	7.9E-13	2.06E-12	6.4E-14	1.6E-04	4.8E-06
2	3.07E-10	5.1E-12	1.04E-07	1.2E-08	1.89E-11	7.9E-13	1.76E-12	5.7E-14	1.6E-04	4.9E-06
3	1.34E-10	4.6E-12	7.83E-08	1.1E-08	1.56E-11	6.6E-13	1.98E-12	6.3E-14	1.5E-04	4.4E-06
4	1.79E-10	5.1E-12	9.63E-08	1.2E-08	2.23E-11	9.5E-13	2.82E-12	8.2E-14	1.8E-04	5.5E-06
5	1.39E-10	4.6E-12	9.59E-08	1.2E-08	1.96E-11	8.2E-13	2.52E-12	7.5E-14	1.6E-04	4.9E-06
6	1.81E-10	5.1E-12	1.18E-07	1.3E-08	2.31E-11	9.5E-13	2.93E-12	8.4E-14	1.6E-04	4.7E-06
7	1.63E-10	4.9E-12	1.14E-07	1.3E-08	2.26E-11	9.4E-13	2.90E-12	8.4E-14	1.7E-04	5.0E-06
Summation*			5.02E-07	2.7E-08	1.03E-10	2.0E-12	1.32E-11	1.7E-13	8.2E-04	1.1E-05

** The summed noble gas and water abundance data are used to calculate a mean NGT recorded by the sample*

Table 2. Temperature estimates from the ML-1 speleothem sample

Crush #	T (°C)	± 2σ	Scaled uncertainty	χ^2	p
step 3	11.7	2.2		0.24	0.62
step 4	7.5	1.8		6.98	0.01
step 5	7.9	1.9		0.73	0.39
step 6	4.1	1.8		0.75	0.39
step 7	5.5	1.8		0.41	0.52
Error weighted temperature using bootstrap	7.3	2.4			
Temperature using integrated noble gas and water abundances (steps 3-7)	7.0	0.8	1.7 *	4.73	0.03

**NGT uncertainty from the summed noble gas and water abundances were scaled by the* $\sqrt{\chi^2}$

9. *Citations*

Aeschbach-Hertig, W., Peeters, F., Beyerle, U., Kipfer, R. 2000. Paleotemperature reconstruction from noble gases in ground water taking into account equilibration with entrapped air. *Nature*. 405: 1040-1044. doi.org/10.1038/35016542

Adam, D.P. and West, G.J. 1983. Temperature and Precipitation Estimates through the Last Glacial Cycle from Clear Lake, California. *Pollen Data*. *Science*. 219(4581): 168-170.

Allen, B.D. and Anderson, R.Y. 2000. A continuous, high-resolution record of late Pleistocene climate variability from the Estancia basin, New Mexico. *GSA Bull*. 112(9): 1444-1458. doi.org/10.1130/0016-7606

Asmerom, Y., Polyak, V.J., Burns, S.J. 2010. Variable winter moisture in the southwestern United States linked to rapid glacial climate shifts. *Nature Geo*. 3: 114-117. doi.org/10.1038/ngeo754

Bacon, S.N., Burke, R.M., Pezzopane, S.K., Jayko, A.S. 2006. Last glacial maximum and Holocene lake levels of Owens Lake, eastern California, USA. *Quat. Sci. Rev*. 25(11-12): 1264-1282. doi.org/10.1016/j.quascirev.2005.10.014

Benson, L.V., Smoot, J.P., Lund, S.P., Mensing, S.A., Foit, F.F. Jr. Rye, R.O. 2013. Insights from a synthesis of and new climate-proxy data from the Pyramid and Winnemucca lake basins for the period 48 to 11.5 cal ka. *Quat. Int*. 310: 62-82. doi.org/10.1016/j.quaint.2012.02.040

Braconnot, P., Otto-Bliesner, B., Harrison, S. Joussaume, S., Peterchmitt, J.-Y., Abe-Ouchi, A., Crucifix, M., Driesschaert, E., Fichefet, Th., Hewitt, C.D., Kageyama, M., Kitoh, A, Laîné, A., Loutre, M.-F., Marti, O., Merkel, U., ramstein, G., Valdes, P., Weber, S.L., Yu, Y., Zhou, Y. 2007. Results of PMIP2 coupled simulations of the Mid-Holocene and Last Glacial Maximum – Part 1: experiments and large-scale features. *Clim. Past*. 3: 261-277.

Brennwald, M.S., Vogel, N., Scheidegger, Y., Tomonaga, Y., Livingstone, D.M., Kipfer, R. 2013. Noble gases as environmental tracers in sediment porewaters and stalagmite fluid inclusions. *The Noble Gases as Geochemical Tracers*. Pp. 123-153. doi.org/10.1007/978-3-642-28836-4_6

Broecker, W. and Putnam, A.E. 2013. Hydrologic impacts of past shifts of Earth's thermal equator offer insight into those to be produced by fossil fuel CO_2. *Proc. Natl. Acad. Sci. USA* 110: 16710- 16715. doi.org/10.1073/pnas.1301855110

Edmunds, W.M., Dodo, A., Djoret, D., Gaye, C.H., Goni, I.B., Travi, Y., Zouari, K., Zuppi, G.-M., Gasse, F. 2004. Groundwater as an archive of climatic and environmental change: Europe to Africa. In: Battarbee R.W., Gasse F., Stickley C.E. (eds) Past Climate Variability through Europe and Africa. Developments in Paleoenvironmental Research, vol 6. Springer, Dordrecht. doi.org/10.1007/978-1-4020-2121-3_14

Edmunds, W.M. 2009 Palaeoclimate and groundwater evolution in Africa—implications for adaptation and management. *Hydro. Sci Jour*. 54(4): 781-792. DOI: 10.1623/hysj.54.4.781

Ersek, V., Clark, P., Mix, A. C., Cheng, H., Edwards, R.L. 2012. Holocene winter climate variability in mid-latitude western North America. *Nature Comms*. 3: 1219. DOI: 10.1038/ncomms2222

Ghadiri, E., Vogel, N., Brennwald, M.S., Maden, C., Häusemannd, A.D., Fleitmann, D., Cheng, H., Kipfer, R. 2018. Noble gas based temperature reconstruction on a Swiss stalagmite from the last glacial–interglacial transition and its comparison with other climate records. *Earth Planet. Sc. Lett*. 495: 192-201. doi.org/10.1016/j.epsl.2018.05.019

Kipfer, R., Aeschbach-Hertig, W., Peeters, F., Stute, M. 2002. Noble gases in lakes and ground waters. *Rev. Mineral. Geochem*. 47: 615-700. doi.org/10.2138/rmg.2002.47.14

Kirby, M.E., Feakins, S.J., Bonuso, N., Fantozzi, J.M., Hiner, C.A. 2013. Latest Pleistocene to Holocene hydroclimates from Lake Elsinore, California. *Quat. Sci. Rev*. 76: 1-15. doi.org/10.1016/j.quascirev.2013.05.023

Kluge, T., Marx, T., Scholz, D., Niggemann, S., Mangini, A., Aeschbach-Hertig, W. 2008. A new tool for paleoclimate reconstruction: noble gas temperatures from fluid inclusion in speleothems. *Earth Planet. Sc. Lett.* 269 (3-4): 408-415. doi.org/10.1016/j.epsl.2008.02.030

Kluge, T., Marx, T., Aeschbach-Hertig, W., Spotl, C., Richter, D.K. 2014. Noble gas concentrations in fluid inclusions as tracer for the origin of coarse-crystalline cryogenic cave carbonates. *Chem. Geo.* 368: 54–62. doi.org/10.1016/j.chemgeo.2014.01.006

Lachniet, M.S., Denniston, R.F., Asmerom, Y., and Polyak, V.J. 2014. Orbital control of western North America atmospheric circulation and climate over two glacial cycles. *Nature Comm.* 5: 380. doi.org/10.1038/ncomms4805.

Ma, L., Castro, M.C., Hall, C.M. 2004. A late Pleistocene–Holocene noble gas paleotemperature record in southern Michigan. *Geophys. Res. Lett.* 31: L23204. doi:10.1029/2004GL021766

McDermott, F. 2004. Palaeo-climate reconstruction from stable isotope variations in speleothems: a review. *Quat. Sci. Rev.* 23(7-8): 908-918. doi.org/10.1016/j.quascirev.2003.06.021

McGee, D., Quade, J., Edwards, R.L., Broecker, W.S., Cheng, H., Reiners, P.W., Evenson, N. 2012. Lacustrine cave carbonates: novel archives of paleohydrologic change in the Bonneville Basin (Utah, USA). *Earth Planet. Sc. Lett.* 351-352: 182-194. doi.org/10.1016/j.epsl.2012.07.019

Meckler, A.N., Affolter, S., Dublyansky, Y.V., Kruger, Y., Vogel, N., Bernasconi, S.M., Frenz, M., Kipfer, R., Leuenberger, M., Spotl, C. 2015. Glacial-interglacial temperature change in the tropical West Pacific: a comparison of stalagmite-based paleo-thermometers. *Quat. Sci. Rev.* 127: 90-116. doi.org/10.1016/j.quascirev.2015.06.015

Munroe, J.S. and Laabs, B.J.C. 2013. Temporal correspondence between pluvial lake highstands in the southwestern US and Heinrich Event 1. *J. Quat. Sci.* 28(1): 49-58. doi.org/10.1002/jqs.2586

Oster, J.L., Montanez, I.P., Kelley, N. 2012. Response of a modern cave system to large seasonal precipitation variability. *Geochim. Cosmochim. Acta.* 92: 91-108. doi.org/10.1016/j.gca.2012.05.027

Oster, J.L., Montanez, I.P., Mertz-Kraus, R., Sharp, W.D., Stock, G.M., Spero, H.J., Tinsley, J., Zachos, J.C. 2014. Millennial-scale variations in western Sierra Nevada precipitation during the last glacial cycle MIS 4/3 transition. *Quat. Res.* 82(1): 236-248. DOI: https://doi.org/10.1016/j.yqres.2014.04.01

Oster, J.L., Montanez, I.P., Santare, L.R., Sharp, W.D., Wong, C., Cooper, K.M. 2015. Stalagmite records of hydroclimate in central California during termination 1. *Quat. Sci. Rev.* 127: 199-214. doi.org/10.1016/j.quascirev.2015.07.027

Owen, L.A., Finkel, R.C., Minnich, R.A., Perez, A.E. 2003. Extreme southwestern margin of late Quaternary glaciation in North America: timing and controls. *Geology*. 31(8): 729-732. doi.org/10.1130/G19561.1

Parai, R., Mukhopadhyay, S., Tucker, J. M., Peto, M.K. 2019. The emerging portrait of an ancient, heterogeneous, and continuously evolving mantle plume source. *Lithos*. 105153; 345-347. doi.org/10.1016/j.lithos.2019.105153

Péron, S., Moreira, M. 2018. Onset of volatile recycling into the mantle determine by Xenon anomalies. *Geochem. Perspect. Let.* 9: 21-25. doi: 10.7185/geochemlet.1833

Quade, J. and Broecker, W.S. 2009. Dryland hydrology in a warmer world: Lessons from the Last Glacial period. *The European Physical Journal Special Topics*. 176(1): 21-36. doi.org/10.1140/epjst/e2009-01146-y

Sander, T., Marx, T., Engel, J., Aeschbach-Hertig, W. 2014. Reproducibility and accuracy of noble gas measurements on water samples in the microlitre range. *Rapid Commun. Mass Spectrom*. 28: 42–48. DOI: 10.1002/rcm.6760

Santi, L.M, Arnold, A.J., Ibarra, D.E., Whicker, C.A., Mering, J.A., Lomarda, R.B., Lora, J.M., Tripati, A. 2020. Clumped isotope constraints on changes in latest Pleistocene hydroclimate in the northwestern Great Basin: Lake Surprise, California. *GSA Bull*. doi/10.1130/B35484.1/4992646/b35484

Scheidegger, Y., Baur, H., Brennwald, S., Fleitmann, D., Wieler, R., Kipfer, R. 2010. Accurate analysis of noble gas concentrations in small water samples and its application to fluid inclusion in stalagmites. *Chem. Geo*. 272: 31-39. doi.org/10.1016/j.chemgeo.2010.01.010

Scheidegger, Y., Brennwald, M.S., Fleitmann, D., Jeannin, P.-Y., Wieler, R., Kipfer, R. 2011. Determination of Holocene cave temperatures from Kr and Xe concentration in stalagmite fluid inclusions. *Chem. Geo*. 288: 61-66. doi.org/10.1016/j.chemgeo.2011.07.002

Schwarcz, H.P., Harmon, R.S. Thompson, P., Ford, D.C. 1976. Stable isotope studies of fluid inclusions in speleothems and their paleoclimate significance. *Geochim. Cosmochim. Acta*. 40(6):657-665. doi.org/10.1016/0016-7037(76)90111-3

Seltzer, A., Ng, J., Danskin, W.R., Kulongoski, J.T., Gannon, R.S., Stute, M., Severinghaus, J.P. 2019. Deglacial water-table decline in Southern California recorded by noble gas isotopes. *Nature Comm*. 10: 5739. doi.org/10.1038/s41467-019-13693-2.

Shakun, J.D., Clark, P.U., He, F., Marcott, S.A., Mix, A.C., Liu, Z., Otto-Bliesner, B., Schmittner A., Bard, E. 2012. Global warming preceded by increasing carbon dioxide concentrations during the last deglaciation. *Nature*. 484: 49–54. doi:10.1038/nature10915

Street, J.H., Anderson, R.S., Paytan, A. 2012. An organic geochemical record of Sierra Nevada climate since the LGM from Swamp Lake, Yosemite. *Quat. Sci. Rev*. 40: 89-106. doi.org/10.1016/j.quascirev.2012.02.017

Stute, M., Schlosser, P., Clark, J.F., Broecker, W.S. 1992. Paleotemperatures in the Southwestern United States derived from noble gases in ground water. *Science*. Vol. 256, Issue 5059, pp. 1000-1003. DOI: 10.1126/science.256.5059.1000

Stute, M., Forster, M., Frischkorn, H., Serejo, A., Clark, J.F., Schlosser, P., Broecker, W.S., Bonani G. 1995. Cooling of tropical Brazil (5 C) during the last glacial maximum. *Science*. 269(5222): 379-383. DOI: 10.1126/science.269.5222.379

Taylor, J. 1997. An introduction to error analysis: the study of uncertainties in physical measurements. Second Edition. University Science Books.

Vacco, D.A., Clark, P.U., Mix, A.C., Cheng, H., Edwards, R.L. 2005. A speleothem record of Younger Dryas cooling, Klamath Mountains, Oregon, USA. *Quat. Res*. 64(2): 249-256. DOI: doi.org/10.1016/j.yqres.2005.06.008

Viau, A. E., Gajewski, K., Sawada, M. C., Bunbury, J. 2008. Low- and high-frequency climate variability in eastern Beringia during the past 25 000 years. *Can. J. Earth Sci.*. 45 (11): 1435–1453. doi.org/10.1139/E08-036

Vogel, N., Brennwald, M.S., Fleitmann, D., Wieler, R., Maden, C., Susli, A., Kipfer, R. 2013. A combined vacuum crushing and sieving (CVCS) system designed to determine noble gas

paleotemperatures from stalagmite samples. *Geochem. Geophys.* 14:2432- 2444. doi.org/10.1002/ggge.20164

Wagner, J.D.M., Cole, J.E., Beck, J.W., Patchett, P.J., Henderson, G.M., Barnet, H.R. 2010. Moisture variability in the southwestern United States linked to abrupt glacial climate change. *Nature Geo.* 3:110-113. doi.org/10.1038/ngeo707

Weyhenmeyer, C.E., Burns, S.J., Waber, H.N., Aeschbach-Hertig, W., Kipfer, R., Loosli, H.H., Matter, A. 2000. Cool Glacial Temperatures and Changes in Moisture Source Recorded in Oman Groundwaters. *Science*. 287(5454): 842-845. DOI: 10.1126/science.287.5454.842

Wortham, B.E., Montanez, I.P., Rowland, D.J., Lerche, M., Browning, A. 2019. Mapping Fluid-Filled Inclusions in Stalagmites Using Coupled X-Ray and Neutron Computed Tomography: Potential as a Water Excess Proxy. *Geochem. Geophys.* 20(6): 2647-2656. doi.org/10.1029/2018GC008140

Supplementary Figures

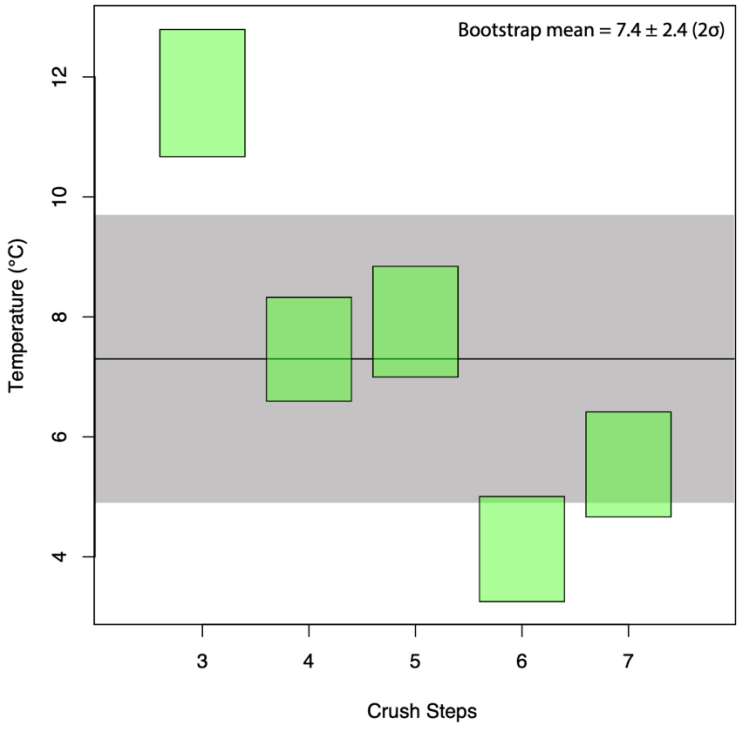

Supp. Fig. 1. Bootstrap mean of temperature results. Individual temperatures with 1 σ range are indicated by green bars. The bootstrap mean and range (7.4 +/- 2.4) are shown by a black line and grey shading.

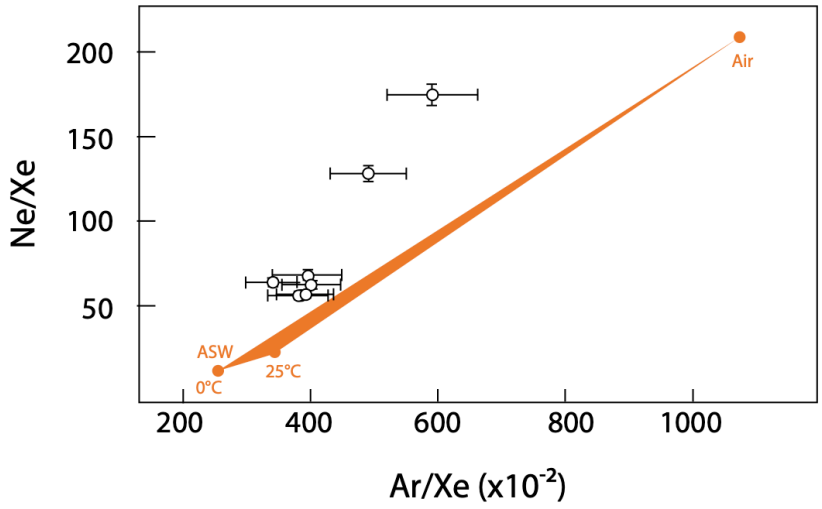

Supp. Fig. 2. Comparison of Ne/Xe to Ar/Xe results from ML-1 to calculated values. Calculated values of ASW for 0 – 25°C and the known value of air are shown as orange circles and the mixing line between them is demonstrated with orange shading. Results from ML-1 (white circles) are shown above the mixing line.

Chapter 3: A record of effective moisture using inclusion fluid $\delta^{18}O$ and $\delta^{2}H$ values in a central Sierra Nevada stalagmite (CA)

Abstract

The oxygen isotopic composition of stalagmites ($\delta^{18}O_{cc}$) is widely used to infer regional changes in terrestrial surface temperatures and precipitation dynamics. The $\delta^{18}O_{cc}$ values, however, record the influence of multiple environmental conditions (e.g. temperature, precipitation source and amount) as well as in-cave physicochemical processes and possible disequilibrium precipitation effects. Conversely, the $\delta^{18}O$ and $\delta^{2}H$ values of fluids entombed in stalagmites ($\delta^{18}O_{fi}$ and $\delta^{2}H_{fi}$) as inclusions have the potential to be robust proxies of the $\delta^{18}O$ and $\delta^{2}H$ compositions of paleo-precipitation. Here we analyze the inclusion fluid $\delta^{18}O_{fi}$ and $\delta^{2}H_{fi}$ values for a stalagmite from a central Sierra Nevada foothill cave, McLean's Cave, in order to reconstruct changes in effective moisture in the region over the last deglaciation (20 to 13 ka). The $\delta^{18}O_{fi}$ values show large increases at 18.0, 15.0, and 13.2 ka, whereas the $\delta^{2}H_{fi}$ value gradually increases throughout the record. Calculations of *d*-excess and $\Delta\delta^{18}O$ based on the $\delta^{18}O_{fi}$ and $\delta^{2}H_{fi}$ values indicate that the temporal shifts to higher $\delta^{18}O_{fi}$ values are associated with decreases in the degree of oxygen isotopic fractionation between the fluid and calcite, reflecting a greater influence of kinetic effects in the cave at those times. The coupling of inclusion fluid and stalagmite calcite stable isotopic compositions provide new constraints on the origin of the stalagmite time series by highlighting periods when effective moisture drove disequilibrium fractionation. In turn, these findings demonstrate that effective moisture (precipitation – evaporation) was lower during warm periods than during colder periods, consistent with other

stalagmite records from the southwestern U.S.

Introduction

Precipitation variability over the last deglaciation (20 to 11 ka) in the southwestern U.S. ('Southwest') has long been linked to changing Northern Hemisphere temperature and continental ice volume (Oster et al. 2009; 2015; Allen and Anderson, 2000; Owen et al., 2003; Quade and Broecker, 2009; McGee et al., 2012; Street et al., 2012; Broecker and Putnam, 2013; Munroe and Laabs, 2013; Oster and Kelley, 2016). In particular for the last deglaciation, stalagmite proxy records from California, and other regions of the Southwest, suggest increased effective moisture during past stadials in comparison to interstadial periods (Asmerom et al., 2010; 2017; Wagner et al., 2010; Lachniet et al., 2014; 2016; Oster et al., 2009; 2014; 2015). This finding corroborates precipitation records for this region developed using independent proxies (Kirby et al., 2013; McGee et al., 2018; Feakins et al., 2019; Santi et al., 2020). This hypothesized hydroclimate regime of wetter stadials and drier interstadials, however, does not conform with all paleoclimate reconstructions for the last deglaciation (Bacon et al., 2006; Benson et al., 2013) and may be an oversimplistic characterization (Hudson et al., 2019; Oster et al., 2020).

Despite a rich proxy archive for the Southwest over the past ~20 ka, our understanding of the sensitivity of the precipitation response in this region to millennial- and centennial-scale climate change, and of the underlying climate dynamics governing the response, remains limited. This incomplete understanding is in part due to the multiple environmental conditions and physicochemical processes, such as temperature (via fluid-calcite oxygen isotope fractionation) and precipitation amount and source as well as in-cave processes that can influence calcite $\delta^{18}O$ values ($\delta^{18}O_{cc}$) (Hendy, 1971; McDermott, 2004; Lachniet, 2009). For example, studies of

California (CA) stalagmites differ in their interpretations of the *primary* driver of temporal changes in $\delta^{18}O_{cc}$ with variability in temperature, precipitation amount or source invoked (Oster et al., 2009; 2014; 2015; 2020; Santi et al., 2020; de Wet et al., 2020). Thus, a proxy independent of $\delta^{18}O_{cc}$ is needed to deconvolve the combined influences of temperature, precipitation parameters (e.g., source, evolution of $\delta^{18}O$ of vapor ($\delta^{18}O_v$) and precipitation ($\delta^{18}O_p$) along the storm track, rainout amount), and in-cave processes (i.e., rapid CO_2 degassing, evaporation).

The $\delta^{18}O$ and $\delta^{2}H$ values of fluids entombed as inclusions in stalagmites (herein referred to as $\delta^{18}O_{fi}$ and $\delta^{2}H_{fi}$) (Table 1) have the potential to deconvolve the aforementioned influences on $\delta^{18}O_{cc}$ values. Previous studies have documented the potential of $\delta^{18}O_{fi}$ and $\delta^{2}H_{fi}$ values as reliable proxies of the $\delta^{18}O$ and $\delta^{2}H$ ($\delta^{18}O_p$ and $\delta^{2}H_p$) values of local paleo-precipitation when a clear relationship between the isotopic compositions of drip-water and local precipitation can be established (Affolter et al., 2015; Dassie et al., 2018; Arienzo et al., 2019). In turn, $\delta^{18}O_{fi}$ and $\delta^{2}H_{fi}$ values have been used to infer variability in moisture-source (Rogerson et al., 2019), precipitation amount (Millo et al., 2017), or mean-annual-temperature (McGarry, 2004; Ayalon et al., 2013; Meckler et al. 2015; Affolter et al., 2015; 2019). Further, many authors have suggested the use of measuring $\delta^{18}O_{fi}$ and $\delta^{2}H_{fi}$ to determine that a stalagmite was precipitated in equilibrium. An underrepresented benefit of $\delta^{18}O_{fi}$ and $\delta^{2}H_{fi}$ measurements is determining to what extent disequilibrium fractionation is influencing a stalagmite record and to develop the temporal variability of these impacts. Disequilibrium fractionation in cave calcite deposits occurs because of low humidity and/or rapid CO_2 degassing (Mickler et al., 2004; Dreybrodt and Deininger, 2014). These processes are driven by climate variability as relative humidity in the cave is frequently lower with less effective moisture (Forbes, 1998; Oster et al., 2012), and CO_2 degassing is linked to the CO_2 composition of the cave, which in turn is related to vegetation

variability and temperature (Banner et al., 2007; Wong et al., 2010; 2011). Environmental monitoring in a Sierran foothill cave (Black Chasm), proximal (~80 km) to McLean's Cave, established a relationship between drip-water $\delta^{18}O$ and $\delta^{2}H$ and precipitation source (Oster et al., 2012). Thus, we propose that the $\delta^{18}O_{fi}$ and $\delta^{2}H_{fi}$ values of stalagmites from caves in the central Sierra Nevada foothills have the potential to place constraints on the relative influence of temperature versus the disequilibrium effects on the stalagmite $\delta^{18}O_{cc}$ values and in turn, to archive variability in effective moisture in this region.

Here we present the first time series of $\delta^{18}O_{fi}$ and $\delta^{2}H_{fi}$ values over the last deglaciation, developed using a central Sierran stalagmite (ML-1 from McLean's Cave), that provides new insight into how precipitation varied between 19 to 13 ka. On the millennial-scale, the new record of $\delta^{18}O_{fi}$ and $\delta^{2}H_{fi}$ values varies in-step with published stalagmite $\delta^{18}O_{cc}$ time series from throughout the Southwest and demonstrates the potential for using stalagmite $\delta^{18}O_{fi}$ and $\delta^{2}H_{fi}$ records to place constraints on regional precipitation history, independent of $\delta^{18}O_{cc}$ values. Furthermore, we evaluate calculated variables, *d*-excess, $\Delta\delta^{18}O$, and temperature, to determine drivers of variability in the $\delta^{18}O_{fi}$ and $\delta^{2}H_{fi}$ record. Finally, we forward model the ML-1 $\delta^{18}O_{cc}$ time-series using Karstolution (Treble et al., 2019), a process-based forward proxy system model that incorporates cave system disequilibrium and equilibrium processes to predict $\delta^{18}O_{cc}$ values based on the $\delta^{18}Op$ and amount, evaporation, and temperature. As far as we are aware, this is the first record developed using both inclusion proxies and forward-modeling techniques to develop constraints on effective moisture through time.

Methods

2.1 Fluid inclusion analysis

Stalagmite ML-1 was previously U-Th dated and analyzed for calcite-based geochemical

and stable isotopic compositions (Santare, 2013; Oster et al., 2015). ML-1 is 22.5 cm long (Fig. 1) and grew between 19.4 ± 0.3 and 11.7 ± 0.4 ka based on 10 U-Th dates. The age/depth model for ML-1 (Fig. 1) was re-evaluated in this study using CoPRA (Breitenbach et al., 2012) in order to incorporate Monte Carlo estimations of age uncertainty (10,000 iterations). The fluid inclusions sampled and analyzed during this study range in age from 19.1 to 12.9 ka. Details on McLean's Cave and the calcite proxy time series can be found in Santare (2013), Oster et al. (2015), and Wortham et al. (2019).

Stalagmite intervals, best suited for inclusion fluid analysis, were identified by coupling neutron and X-ray computed tomography, an approach that has been documented to successfully identify intervals rich in fluid- vs. air-filled inclusions (Wortham et al., 2019). Petrographic study and coupled XCT and NCT scanning reveal distribution and density of fluid-filled inclusions along the growth axis of the stalagmite. Along a growth band there is a consistent distribution of fluid-filled inclusions (Fig. 2A; Wortham et al., 2019). Physically isolating a given growth band from mm-thick wafers of stalagmite (prepared from 2 by 1 inch thin-section billets) for inclusion fluid analysis is challenging due to the sub-mm spatial scale of bands. In this study, when a given wafer was split in half to be analyzed twice for $\delta^{18}O_{fi}$ and $\delta^{2}H_{fi}$ (Fig. 2B), the two analyses are considered duplicates and not true replicates and thus plotted as individual results on all plots and considered as individual data points in statistical analysis.

Fluid-rich regions in ML-1 were sampled as 200 to 500 mg chips (X:Y:Z dimensions of 0.25 to 0.50 cm: 1 cm: 0.25 cm) taken from 0.25 cm thick wafers that were previously cut from thin-section billets. Analysis of the inclusion fluids in 31 chips (n = 41 analyses including duplicates) was performed on a modified 'Miami Device' in the Stable Isotope Laboratory, Rosenstiel School for Marine and Atmospheric Sciences (RSMAS), University of Miami, FL

using a modified version of the methodology of Arienzo et al. (2013) (Supp. Fig. 1). The method was modified in three keys ways:

The H_2O released from the crushed sample was allowed to enter directly into the CRDS, producing a sharp H_2O peak, with the $^{18}O/^{16}O$ ratio being determined by integrating the ^{18}O and ^{16}O peaks. The details on this methodology are including in the Supplementary Material.

In the previous methods an expansion volume was present prior to the gas entering into the CRDS. This allowed a relatively constant signal to be attained and integrated over several minutes. This provided relatively stable $\delta^{18}O$ values at the expensive of sensitivity. As a result, different data reduction and summarization procedures were applied to process the data (Supp. Mat.).

A quartz tube with platinum wire, heated to the crushing line and heating it to 400°C, was added in order to reduce interference in the CRDS created by the presence of organic molecules (Supp. Fig. 1) (cf. Dassie et al., 2018), which are known to deleteriously affect the $\delta^{18}O$ values by interfering at the wavelengths uses.

Based on analyses of repeated standard measurements, the analytical precision (1σ) for the RSMAS Miami Device is 0.2‰ and 1.1‰ for $\delta^{18}O_{fi}$ and $\delta^{2}H_{fi}$, respectively. In addition, a subset of stalagmite chips (duplicates of those run at RSMAS; n = 9) were analyzed on a TC-EA IRMS in the Stable Isotope Laboratory, Max Planck Institute for Chemistry (MPIC), Mainz, Germany (Vonhof et al., 2006; de Graaf et al., 2020) in order to determine the relative offset between CRDS and TC-EA IRMS methods (Supp. Table 2). Analytical precision (1σ) for the TC-EA IRMS at MPIC based on repeated measurements of standard waters and minerals is 0.5‰ and

5.0‰ for $\delta^{18}O_{fi}$ and $\delta^{2}H_{fi}$, respectively.

2.2 Data Analysis

We follow the time-interval differentiation for the last deglaciation proposed by Oster et al. (2020): Late Glacial (LG, 19.3 to 18.0; n=8 samples analyzed), Heinrich Stadial 1a (18.0 to 16.1 ka, n=8 samples analyzed), Heinrich Stadial 1b (16.1 to 14. 6 ka; n=8 samples), the Older Dryas stadial (OD, 14.1 to 13.8 ka; n=5 samples analyzed), and the Bölling and Allerød interstadials (14.6 to 14.1 ka and 13.8 to 12.8 ka, respectively; n=12 samples). Two phases of Heinrich Stadial 1 have been previously denoted as the "Big Dry" and the subsequent "Big Wet" (Broecker et al., 2009). Recently, inconsistencies in effective moisture reconstructions for the Southwest have been documented (cf. Hudson et al., 2019); thus, we refer to the two phases of Heinrich Stadial 1 as HS1a and HS1b. Results for the warmer Bölling and the Allerød interstadials (<1 ky duration each) were combined as they are short and are two warm intervals punctuated by a brief cooling. This inclusive interval is referred to as the B/A (Bölling/Allerød).

In order to assess whether equilibrium oxygen isotope fractionation between drip-water and calcite occurred during stalagmite formation and to assess the potential influence of evaporation on inclusion fluid and stalagmite calcite isotopic compositions, we calculated three variables using the measured inclusion fluid $\delta^{18}O_{fi}$ and $\delta^{2}H_{fi}$ and $\delta^{18}O_{cc}$ values from ML-1 and using the modern precipitation values from the region. The first, $\Delta\delta^{18}O$, is the difference between measured $\delta^{18}O_{cc}$ (converted to VSMOW) and $\delta^{18}O_{fi}$. Given the very different temporal resolutions of the $\delta^{18}O_{cc}$ and $\delta^{18}O_{fi}$ data sets for ML-1, the stalagmite $\delta^{18}O_{cc}$ values (n = 617; Santare 2013; Oster et al., 2015) were bin-averaged to match the temporal resolution (100 to 200 yr) of the $\delta^{18}O_{fi}$ and $\delta^{2}H_{fi}$ analyses before calculating $\Delta\delta^{18}O$ values for each new $\delta^{18}O_{fi}$ datum. To better understand the $\delta^{18}O_{fi}$ results, we calculate $\Delta\delta^{18}O$ using three approaches. In the first

approach, we calculate $\Delta\delta^{18}O$ using the $\delta^{18}O_{fi}$ as was originally measured. In the second approach, we modify the $\delta^{18}O_{fi}$ values by subtracting 1‰ from each measurement (herein referred to as $\delta^{18}O_{fiM}$) and use the modified values as a proxy of fluid $\delta^{18}O$ (see below for rationale). For the third approach, we calculate fluid $\delta^{18}O$ values using the measured $\delta^{2}H_{fi}$ values from stalagmite ML-1 and the Local Meteoric Water Line defined for Black Chasm ($\delta^{2}H = 7.9 \times \delta^{18}O + 9.3$; Oster et al. 2012).

We further compare these calculated $\Delta\delta^{18}O$ values to the predicted values of $\Delta\delta^{18}O$ calculated for 7.0, 10.0, and 12.3 °C, using the equilibrium oxygen isotope fractionation equation of Daëron et al. (2019) and using the in-cave fractionation equation from Tremaine et al. (2011). The Tremaine et al. (2011) oxygen isotope fractionation equation was defined using *in-situ* cave monitoring data, including data from Coplen (2007). The equation from Daëron et al. (2019) is based on two *in-situ* modern carbonates that formed in caves and are believed to represent natural equilibrium fractionation. The low end-member temperature (7°C) is based on a noble gas temperature (7.0 ± 1.7 °C) derived using included fluid noble gas concentrations from an interval of ML-1 stalagmite that grew at 18.8 ka (Wortham et al., *in revision*). The high end-member temperature (12.3 °C) is the present-day mean annual cave air temperature at Black Chasm (Oster et al., 2012).

We further calculated *d*-excess values for each inclusion data point in order to assess the potential influence of evaporation on inclusion-fluid isotopic compositions. We note here that the definition of *d*-excess used in this study is based on previous researchers working in cave and terrestrial environments and is therefore focused on the process of rainwater recycling due to evaporation (Lachniet et al., 2009; Arienzo et al., 2015; Anderson et al., 2016). The *d*-excess, or deuterium excess, is the 'y-intercept' of the best-fit line through the $\delta^{18}O$ and $\delta^{2}H$ values

distributed on a x- and y-plot. We calculate the *d*-excess using the following equation: *d*-excess = δ^2H_{fi} - (7.9 * $\delta^{18}O_{fi}$) as defined by the Local Meteoric Water Line (Oster et al., 2012). Finally, we calculate temperatures of precipitation for each pair of measured $\delta^{18}O_{fi}$ and its corresponding binned $\delta^{18}O_{cc}$ value using the temperature fractionation equations of Tremaine et al. (2011) and Daëron et al. (2019). Both of these temperature equations were defined in part using the calcite that precipitated in equilibrium from Devil's Hole in Nevada Coplen et al. (2007).

We statistically evaluated the covariation between the $\delta^{18}O_{fi}$ and δ^2H_{fi} values and the calcite $\delta^{18}O$ values (Oster et al., 2015a) for ML-1, as well as with two other stalagmite $\delta^{18}O_{cc}$ time series from the Southwest that are continuous through the deglaciation (Fort Stanton Cave, NM, FS; Asmerom et al., 2010 and Cave of the Bells, AZ, COB; Wagner et al., 2010). In order to statistically compare the $\delta^{18}O_{fi}$ results with the three stalagmite $\delta^{18}O_{cc}$ time-series we carried out the following three steps. First, all data were linearly interpolated to a 100-year sampling step for each stadial and interstadial within the overall span of the ML-1 record (19 to 13 ka) in order to ensure consistency between the data sets. Second, the variability within each time-series was assessed using a change point test that uses the adaptive wild binary segmentation approach (Fryzlewicz, 2014) to calculate the variability in the mean values in the data and to segment the data into coherent subsets. This approach is carried out iteratively until all statistically significant segmentations, by mean, are exhausted and demonstrates where, in each time series, the mean of the data significantly varies, therefore identifying statistically robust temporal shifts. Furthermore, the frequency of change through each $\delta^{18}O$ time series was assessed by performing a wavelet coherence and a cross-wavelet transformation using the function 'biwavelet' (Gouhier et al., 2019). We followed a similar approach to compare the ML-1 δ^2H_{fi} values to a biomarker

δ^2H record (32 to 9 ka) from Lake Elsinore (Kirby et al., 2013; Feakins et al., 2019).

Forward Proxy System Modeling

We used the isotope-enabled forward model Karstolution (Treble et al., 2019) to simulate values of stalagmite $\delta^{18}O_{cc}$ values (modeled values herein referred to as $\delta^{18}O_{cc}^{*}$) for a suite of input environmental conditions and processes relevant to McLean's Cave and using the $\delta^{18}O_{fi}$ values as proxies of drip-water in the cave through time. In turn, the Karstolution $\delta^{18}O_{cc}^{*}$ values (Supp. Table 3) are compared to the measured and bin averaged $\delta^{18}O_{cc}$ values for stalagmite ML-1 in order to further interrogate the process-based relationship between measured $\delta^{18}O_{cc}$ and $\delta^{18}O_{fi}$ values and sensitivity to paleo-environmental parameters. Karstolution combines the KarstFor model (Bradley et al., 2010; Baker and Bradley, 2010; Baker et al., 2013; Treble et al., 2013) and the iSOLUTION model (Deininger et al., 2012) to quantify karst processes and in-cave fractionation of ^{18}O. This model inputs monthly precipitation $\delta^{18}O$ values, evaporation (mm), temperature (°C), and precipitation amount (mm) in order to calculate the fluxes of water into, out of, and within a karst reservoir, the variability in fluid $\delta^{18}O$ in the karst system, and the $\delta^{18}O_{cc}$ precipitated under a thin film of water (<100 μm) from that reservoir (Dreybrodt and Deininger, 2014). In addition, the model uses a configuration file for which cave parameters, such as cave-air pCO_2 and relative humidity are prescribed (Supp. Table 3). Karstolution produces one drip-water $\delta^{18}O$ time series and six $\delta^{18}O_{cc}$ time series that in turn provide constraints on water-residence time in the reservoir.

We performed 27 simulations using Karstolution varying the input temperature and precipitation to evaporation ratio (herein referred to as P:E) (Supp. Table 3). The temperature used for each experiment was 7°C or 10°C based on the aforementioned temperature constraints for the LGM and modern cave setting. It is unlikely, however, that temperatures rose during the

deglaciation to that of the modern thus simulations run with 10°C exceed end-member values. For P:E ratios, we used present-day P:E ratios determined using precipitation data collected at New Melones Dam (WRCC, 2019). Additionally, we used 45 years of monthly output from a water isotope-enabled fully coupled Earth system model (iCESM1.3), with LGM boundary conditions, to constrain P:E ratios for the central Sierra Nevada, California region (Tabor et al., *submitted*). The P:E values range from 1:10 to 1000:1 (mm) (Supp. Table 3). Finally, each of the 27 Karstolution simulations were run three times in order to vary the $\delta^{18}O_p$ input values to reflect three scenarios of inclusion-fluid results. The first set of 27 simulations input the measured $\delta^{18}O_{fi}$ values as a proxy of precipitation, the second set used $\delta^{18}O_{fiM}$ values (modified by -1‰), and the third set used $\delta^{18}O_p$ values that were inferred from the LMWL using the $\delta^{2}H_{fi}$ values. These three sets of experiments mirror the $\Delta\delta^{18}O$ calculations as described in Section 2.2. Together the 27 experiments test the sensitivity of $\delta^{18}O_{cc}$ output to the full range of these parameters.

Two additional Karstolution simulations were run using 45 years of monthly output of temperature, precipitation, evaporation, and $\delta^{18}Op$ values from the LGM (21 ka) and pre-industrial (1850 C.E.) simulations run using iCESM-1.3 (Tabor et al., *submitted*; herein referred to as the "fully-tuned" Karstolution simulations). The simulated drip-water $\delta^{18}O$ values from the two 'fully-tuned' simulations are compared to the inclusion-fluid measurements and to the $\Delta\delta^{18}O$ calculations to further understand variability in the measured inclusion fluid values (Supp. Fig. 4).

Results

3.1 Comparison of inclusion fluid and modern meteoric stable isotopic compositions

The measured $\delta^{18}O_{fi}$ and $\delta^{2}H_{fi}$ values range from -11 to -5‰ and -90 to -60‰ (Supp. Table 3), respectively, with the $\delta^{18}O$ values being offset to the right of the local meteoric water line by

~1‰ (Fig. 3A). Notably, the measured $\delta^{18}O_{fi}$ and $\delta^{2}H_{fi}$ values of all duplicates are within 1σ uncertainty of a y = x line indicating minimal offset between the two analytical approaches used (TC-EA and CRDS). In addition, we assess published stable isotope analyses of fluid-filled inclusions in stalagmites (Supp. Fig. 2) (cf. Meckler et al., 2015; de Graaf et al., 2020). A similar finding was found by other fluid inclusion studies that compared results of the two analytical methods. Measured $\delta^{18}O_{fi}$ and $\delta^{2}H_{fi}$ values demonstrate an offset (~1‰) from the LMWL (Fig. 3). Furthermore, the $\delta^{18}O_{fi}$ values are well within the range of $\delta^{18}O_{p}$ values at the Black Chasm locality (Oster et al., 2012) and in Sequoia National Park (McCabe-Glynn et al., 2016) (Fig. 3A). The $\delta^{2}H_{fi}$ values (-60 to -90‰) are 15‰ more variable than those of Black Chasm drip-water (-55 to -80‰), but within the range of $\delta^{2}H_{p}$ values.

3.2 Temporal variability in inclusion-fluid isotopic compositions

Through time, the measured $\delta^{18}O_{fi}$ values of ML-1 initially decrease by ~2‰ from the LG into HS1b after which values increase by 4‰ to a peak at 15 ka (Fig. 4). A subsequent decrease in $\delta^{18}O_{fi}$ (by 2‰) occurs in the OD followed by a rise (by 4‰) to a second peak in the B/A (13.2 ka). Overall, the $\delta^{18}O_{fi}$ and binned $\delta^{18}O_{cc}$values exhibit little correlation.

The average values of $\Delta\delta^{18}O$ in equilibrium at 7 and 10 °C span 33.8 to 31.9‰ (Fig. 4). In contrast, $\Delta\delta^{18}O$ values calculated using the measured $\delta^{18}O_{cc}$ and $\delta^{18}O_{fi}$ values (referred to as 'measured' $\Delta\delta^{18}O$) are lower ranging between 26 and 32‰. At 19 ka (Fig. 4), the 'measured' $\Delta\delta^{18}O$ values are ~30‰ subsequently decreasing to 26‰ at 18 ka after which the values approach near equilibrium values remaining in that range to ~15 ka (late HS1b). The $\Delta\delta^{18}O$ values shift abruptly to lower values (by 4‰) at 15.0 ka and again, albeit more gradually, at 13.2 ka (Fig. 4). $\Delta\delta^{18}O$ values approach predicted equilibrium values (~32‰) at 15.2 ka and during the BO at 14.5 ka. The calculated *d*-excess values range between -10 and 10‰ and covary with

$\delta^{18}O_{fi}$ and 'measured' $\Delta\delta^{18}O$ (Fig. 4). The *d*-excess values trend to negative values at 18.0, 15.0, and 13.2 ka. Temperatures calculated using the $\delta^{18}O_{fi}$ and $\delta^{18}O_{cc}$ values range from 10 to 45°C (Fig. 5), largely higher than modern temperatures in Black Chasm (Oster et al., 2012) and anticipated temperatures for the last deglaciation. Temperatures trend to the highest values at 18.0, 15.0, and 13.2 ka, when *d*-excess values are at their lowest, and temperatures are at their lowest 15.2 and 14.5 ka, when $\Delta\delta^{18}O$ values approach predicted equilibrium values and *d*-excess values are higher. Moreover, estimated temperatures fall within the Black Chasm modern temperatures during parts of the LG (19.3 to 18 ka), throughout much of the later part of HS 1a and lower two-thirds of HS 1b 1 (17 to 15.2 ka), and during the Older Dryas (14.1 to 13.8 ka).

4. Discussion

In order to evaluate the preservation of a primary drip-water signal in the $\delta^{18}O_{fi}$ and $\delta^{2}H_{fi}$ values of stalagmite ML-1, we applied three tests and conclude that the values have recorded in-cave dripwater during stalagmite growth. We subsequently, compare the $\delta^{18}O_{fi}$ and $\delta^{2}H_{fi}$ values with modeled $\delta^{18}O_{cc}$ values made using the forward proxy system model, Karstolution. Based on the results presented in the following sections, we posit that the $\delta^{18}O_{fi}$ and $\delta^{2}H_{fi}$ values record shifts in effective moisture through time. Finally, we compare the inclusion-fluid isotopic trends to published stalagmite and lacustrine proxy records from the US Southwest and to climate simulations for the region. Together these approaches demonstrate that through the last deglaciation (19 to 13 ka recorded in ML-1), the stalagmite $\delta^{18}O_{fi}$ and $\delta^{2}H_{fi}$ time series archive intervals of lower effective moisture in the central Sierra Nevada foothill region that correspond

to synchronous periods of inferred lower effective moisture across the US southwest.

4.1 Reliability of inclusion-fluid $\delta^{18}O_{fi}$ and δH_{fi} values

Previous studies have evaluated the utility of measured $\delta^{18}O_{fi}$ values as a robust proxy of drip-water $\delta^{18}O$ given the potential for post-formation exchange of oxygen between the stalagmite $CaCO_3$ and the inclusion fluids (Schwarcz et al., 1976; Harmon et al., 1979; Genty et al., 2002; Matthews et al., 2000; McGarry et al., 2004; Demeny et al., 2016). Petrographic (transmitted light and epifluorescence; Oster et al., 2015a) and coupled X-ray and neutron activation-computed tomographic study (XCT and NCT) of stalagmite ML-1 (Wortham et al., 2019) document banded growth layers free of dissolution features and with systematic distribution of inclusions. The coupled scanning approach also documents the occurrence of inclusions concentrated between elongate crystals indicating their primary origin and discerns those that are fluid-filled vs. air-filled. The upper 7 cm of stalagmite ML-1 reveals less consistent banding than the rest of the stalagmite and in this portion of the stalagmite, the fluid-filled inclusions occur as either micro-pores or macro-pores (Wortham et al., 2019). For the purposes of this study, we have focused on the fluid-filled micro-pores as XCT and NCT scanning as well as petrographic evidence indicate that micro-pores are isolated along growth bands and are not diagenetically altered by post-formation dissolution.

A second test of the primary nature of the inclusion-fluid compositions is to evaluate the possible temperature range that stalagmite ML-1 has experienced since formation. Although exposure to temperatures of >105°C can promote calcite to re-equilibrate in post-formation fluids (Uemera et al., 2020), stalagmite ML-1 has been exposed to a maximum temperature change since formation of 0.0 to 5.1 ± 1.7 °C (Wortham et al., *in review*). Additionally, several

recent studies (Meckler et al. 2015; Affolter et al., 2015; 2019; Arienzo et al., 2017; Millo et al., 2017; Dassie et al., 2018) have demonstrated that $\delta^{18}O_{fi}$ and $\delta^{2}H_{fi}$ values are well preserved when the inclusion-fluid values generally correspond with the local or global meteoric water lines (Affolter et al., 2015; 2019). As presented in Section 3.1, the $\delta^{18}O_{fi}$ and $\delta^{2}H_{fi}$ values of ML-1 stalagmite generally track the LMWL with an increase to higher $\delta^{18}O$ values (up to ~1‰) for a given $\delta^{2}H$ value. On the basis of these three tests, we conclude that the $\delta^{18}O_{fi}$ and $\delta^{2}H_{fi}$ values in the ML-1 stalagmite are a reliable proxy of paleo-dripwater, although the inclusion-fluid values may have been moderately modified by evaporative processes in the cave prior to their entrapment as inclusions.

4.2 Interpreting $\delta^{18}O_{fiM}$ and $\delta^{2}H_{fi}$ compositions as a record of effective moisture

The offset of ML-1 inclusion fluids from the LMWL (Fig. 3B) of -1‰ is similar for measurements made using either the TC-EA or CRDS, indicating a lack of an analytical bias for one system over the other that might impact the measured $\delta^{18}O_{fi}$ values. Notably, the observed offset is comparable to that for CRDS measurements of inclusion fluids made by others (Meckler et al. 2015). Stalagmite $\delta^{18}O_{fi}$ values that are consistently more positive than modern drip-water and/or measured $\delta^{18}O$ values are observed in other fluid-inclusion datasets from subtropical Brazil (Millo et al., 2017), southwest France (Labuhn et al., 2015), and Indonesia (Griffiths et al., 2010). This suggests that the offset observed for ML-1 is consistent with observations from other locations. We accommodate this observation in inclusion-fluid datasets by providing a 'modified' $\delta^{18}O_{fi}$ variable ($\delta^{18}O_{fiM}$) that is the measured $\delta^{18}O_{fi}$ values with a subtraction of 1‰. This modification is used to assess temporal trends in the data, which are not impacted by modifying the values. It is important to note, however, that we do not use these modified values alone to suggest evaporative enrichment and instead rely on the modeled and calculated variables

presented in this section to discuss process.

In order to better understand the potential for disequilibrium isotopic fractionation, we calculated $\Delta\delta^{18}O$ values for ML-1 using measured stalagmite calcite and inclusion-fluid $\delta^{18}O$ values, which record equilibrium or disequilibrium fractionation processes. These $\Delta\delta^{18}O$ values are compared to those calculated using modeled (Karstolution) drip-water $\delta^{18}O$ and calcite $\delta^{18}O_{cc}{}^{*}$ values ($\Delta\delta^{18}O^{*}$), Sr/Ca and d13C values from ML-1 calcite, and δ^{18}Occ values from stalagmite across the Southwest. The $\Delta\delta^{18}O$ values shift away from predicted equilibrium values at 18.0, 15.0, and 13.2 ka, but trend toward predicted equilibrium values at 15.2 and 14.5 ka. Deviation of the calculated $\Delta\delta^{18}O$ from predicted values suggest disequilibrium fractionation, regardless of driving mechanism.

The mechanics of calcite-fluid isotopic disequilibrium fractionation in cave environments and the influence on the direction of the resulting $\Delta\delta^{18}O$ shift (higher or lower) remain debated. For example, cave monitoring studies demonstrate that $\Delta\delta^{18}O$ values increase during periods of disequilibrium fractionation driven by rapid CO_2 degassing (independent of relative humidity) that leads to Rayleigh distillation and progressive increase in $\delta^{18}O$ value of dissolved inorganic carbon (DIC) in the thin-film fluids from which the stalagmite calcite precipitates (Mickler et al., 2004; Dreybrodt and Deininger, 2013; Carlson et al., 2020). A model designed to evaluate disequilibrium fractionation during stalagmite formation (Dreybrodt and Deininger, 2013) assumes that the calcite inherits the $\delta^{18}O$ value of the DIC from which it precipitates without further modification, leading to increasing $\Delta\delta^{18}O$ with increasing degree of calcite-fluid isotopic fractionation disequilibrium. Conversely, an ion-by-ion-based model demonstrates that pH and growth rate can change the kink mechanisms in calcite growth, which impacts the precipitating $\delta^{18}O_{cc}$ values, ultimately driving a $\Delta\delta^{18}O$ *decrease* with disequilibrium fractionation (Watkins et

al., 2013; 2014). This model for vadose unsaturated systems, however, is based on saturated phreatic system processes in which $\Delta\delta^{18}O$ decreases with increasing precipitation rate (Degens, 1981) and may not be applicable to vadose karst systems. A shift in ML-1 $\Delta\delta^{18}O$ values away from predicted equilibrium fractionation values observed for the three intervals 18.0, 15.0, and 13.2 ka (Fig. 4; Supp. Fig. 4), indicates that the observed variability in $\Delta\delta^{18}O$ values records shifts from (near) equilibrium to non-equilibrium isotopic fractionation repeatedly throughout the growth of stalagmite ML-1.

In-situ studies evaluating disequilibrium fractionation during stalagmite growth have further shown that for caves characterized by seasonal variability in cave relative humidity and CO_2 degassing, both processes can drive $\Delta\delta^{18}O$ values away from predicted values for equilibrium fractionation (e.g. Carlson et al., 2020). For the Sierra Nevada caves, increased CO_2 degassing occurs during the wet season due to increased cave ventilation driven by colder surface air temperatures (Oster et al. 2012). For the ML-1 stalagmite, low *d*-excess values (lower cave humidity) during the three intervals 18.0, 15.0, and 13.2 ka that are characterized by a shift to lower $\Delta\delta^{18}O$ values and away from predicted equilibrium fractionation values (and vice-versa for the periods at 15.2 and 14.5 ka, when $\Delta\delta^{18}O$ values approach predicted equilibrium values) (Fig. 4)) suggests that centennial to millennial-scale decreases (increases) in relative humidity played a role in driving hypothesized oxygen isotope disequilibrium fractionation during low-humidity periods. In the modern, low *d*-excess values are associated with evaporative environments (Rozanski et al., 1993; Clark and Fritz, 1997; Lachniet, 2009; Anderson et al., 2016). Low *d*-excess values have been documented in drip-waters of tropical (Onac et al., 2008; Polk et al., 2012), Mediterranean (Moreno et al., 2014) and semi-arid cave environments (Bar-Matthews and Ayalon, 2004), attributed to seasonal fluctuations in P:E that can lead to 10 to 30% variability in

d-excess values of karst reservoir fluids. Similarly, we suggest that lower *d*-excess values for ML-1 argue for increased evaporation within McLean's Cave, during the aforementioned three intervals (18.0, 15.0, and 13.2 ka). Collectively, these findings suggest that periods of lower effective moisture in the region promoted drip-water evaporation and disequilibrium oxygen isotopic fractionation during precipitation of stalagmite calcite in McLean's Cave. Conversely, periods of inferred higher effective moisture (15.2 and 14.5 ka) dampened evaporation of drip-waters and favored equilibrium isotopic fractionation.

Variability in the amount of moisture would also impact calcite proxies that are sensitive to prior calcite precipitation and CO_2 degassing, such as the Sr/Ca ratio and $\delta^{13}C$ value, as these processes are influenced by the amount of rainfall above McLean's Cave (Oster et al., 2012; 2015a). The records of 2015). For the three intervals characterized by lower $\Delta\delta^{18}O$ values and inferred disequilibrium isotopic fractionation, the ML-1 Sr/Ca ratios and $\delta^{13}C$ values from ML-1 demonstrate sub-centennial scale variability at 18 ka (0.2 log units and ~1‰, respectively) and centennial shifts to higher Sr/Ca ratios and $\delta^{13}C$ values (0.2 log units and 2‰, respectively) at 15.0 and 13.2 ka (Fig. 6). Visually, Sr/Ca and $\delta^{13}C$ begin to increase from trends of decreasing values at each of these three times. There are periods, however, of much higher Sr/Ca and $\delta^{13}C$ values throughout the record that do not correspond to the variability in the inclusion-fluid results. Considering that higher values indicate greater prior calcite precipitation and CO_2 degassing (Oster et al., 2012; Oster et al., 2015) the weak relationship between the fluid inclusion results and the Sr/Ca and $\delta^{13}C$ could indicate a weak control of CO_2 degassing and/or prior calcite precipitation on disequilibrium in stalagmite ML-1. Conversely, the lack of strong relationship between these proxies may suggest that low humidity in the cave system alone is driving disequilibrium fractionation at the aforementioned periods (18.0, 15.0, and 13.2 ka),

consistent with less effective moisture at these times. Further work that evaluates where in the drip-water system (vadose zone storage, stalactite and/or soda straw ceiling vs. conduit flow through fissures in cave ceiling, drip-water flow in the cave) disequilibrium fractionation is occurring and how this impacts the inclusion-fluid proxies and the Sr/Ca and $\delta^{13}C$ proxies, respectively, is needed to better understand this relationship.

In order to further examine the oxygen isotopic variability in the ML-1 record, we used Karstolution forward proxy modeling (Treble et al., 2019) to produce simulated calcite $\delta^{18}O$ time series ($\delta^{18}O_{cc}^{*}$). The forward modeling approach includes 80 Karstolution experiments (Section 3.4). Of the 80 experiments, the best agreement between measured $\delta^{18}O_{cc}$ and modeled $\delta^{18}O_{cc}^{*}$ is found when the $\delta^{18}O_{fi}$ values, which were input as a proxy of precipitation $\delta^{18}O$, were modified by -1‰ ($\delta^{18}O_{fiM}$) to account for the observation that inclusion-fluid datasets are offset by 1‰. We present here comparisons between modeled $\delta^{18}O_{cc}^{*}$ and measured $\delta^{18}O_{cc}$ from stalagmite ML-1 using the measured $\delta^{18}O_{fi}$, the modified $\delta^{18}O_{fi}$ values ($\delta^{18}O_{fiM}$) values, and the calculated $\delta^{18}O_{fi}$ values to better understand the source(s) and origin of the variability in the ML-1$\delta^{18}O_{cc}$, $\delta^{18}O_{fi}$, and $\Delta\delta^{18}O$ values (Fig. 7).

The Karstolution experiments yield modeled stalagmite $\delta^{18}O_{cc}^{*}$ values that range between -5 to -9.5‰ which overlap in some intervals but are overall higher than the measured ML-1 values ($\delta^{18}O_{cc}$ of -8 to -12‰; Fig. 6). The simulated $\delta^{18}O_{cc}^{*}$ values using 7°C as the in-cave temperature do not overlap with measured $\delta^{18}O_{cc}$ values when the precipitation input is constrained by the unmodified $\delta^{18}O_{fi}$ values. The experiments that were parameterized using an in-cave temperature of 10°C and $\delta^{18}O_{fiM}$ or calculated $\delta^{18}O_{fi}$ lead to greater overlap between modeled and measured stalagmite $\delta^{18}O_{cc}$ values. Conversely, there is no overlap between the

measured $\delta^{18}O_{cc}$ and modeled $\delta^{18}O_{cc}$ values for the 10°C experiments that used the measured $\delta^{18}O_{fi}$ values for input (Fig. 6). Overall, the best agreement between all modeled and measured $\delta^{18}O_{cc}$ time series occurs when P:E ratios are ≥ 100:1 further supporting the hypothesis of low effective moisture driving drip-water evaporation and disequilibrium oxygen isotope fractionation, in particular during specific intervals of stalagmite growth over the last deglaciation.

The 'fully-tuned' model runs of Karstolution yield drip-water $\delta^{18}O$ values of -10.5‰ for the pre-industrial period and -11.0‰ for the LGM (Supp. Fig. 4). These values overlap the majority of the ML-1 inclusion fluid values when modified (likely to account for evaporation) or calculated using the measured $\delta^{2}H_{fi}$ values and the LMWL (Supp. Fig. 4). Notably, both the calculated $\delta^{18}O_{FI}$ and $\delta^{18}O_{fiM}$ values are higher than the modeled drip-water values for the periods of 18.0, 15.0, and 13.2 k (periods of inferred oxygen isotopic disequilibrium) and lower than the modeled drip-water at 15.2 and 14.5 ka (periods of (near) equilibrium oxygen isotopic fractionation) (Supp. Fig. 4). The Karstolution findings thus further support the hypothesis that intervals of ML-1 stalagmite growth occurred during lower effective moisture that in turn drove drip-water evaporation and disequilibrium oxygen isotope fractionation. In addition to the above analysis, we calculated the $\Delta\delta^{18}O$ values from the synthetic drip-water and calcite values from Karstolution (Supp. Fig. 5). It is important to note that the modeled $\Delta\delta^{18}O$ values use the measured $\delta^{18}O_{fi}$ values as an input for $\delta^{18}O_{p}$ and thus may already account for any evaporation effects on measured $\delta^{18}O_{fi}$ values. This comparison evaluated the influence of disequilibrium fractionation on ML-1 $\delta^{18}O_{cc}$ values that if present may or may not have been driven by decreases in cave humidity. We found that the synthetic $\Delta\delta^{18}O$ agrees with predicted values of

$\Delta\delta^{18}O$ when the P:E ratio is 100:1 and the cave temperature is a constant 10 °C (Supp. Mat.)

The observed temporal variability in the oxygen isotopic values of the ML-1 inclusion fluids, the Karstolution $\delta^{18}O_{cc}{}^{*}$ results (Fig. 7), the higher than anticipated temperatures calculated from these results (Fig. 5), and the variability in $\Delta\delta^{18}O$ and *d*-excess indicates that the ML-1 record was influenced by calcite-fluid oxygen isotope disequilibrium fractionation during three intervals of the last deglaciation (18.0, 15.0, and 13.2 ka). This does not preclude shifts to disequilibrium precipitation during other periods of growth of the ML-1 stalagmite as most calculated $\Delta\delta^{18}O$ are lower than predicted equilibrium values, but rather it indicates the three intervals that are characterized by notable changes in effective moisture. Disequilibrium (i.e., kinetic) fractionation has been identified in stalagmites and cave monitoring studies where kinetic processes are attributed to rapid CO_2 degassing and drip-water supersaturation (Baker et al., 1997; Mickler et al., 2004; Reynard et al., 2011; Kluge and Affek, 2012; Millo et al., 2017) and has been argued as a reason to rule out certain stalagmites as paleoclimatic archives. We demonstrate here that inferred disequilibrium fractionation can in itself be a useful paleoclimate indicator as it suggests rapid CO_2 degassing, drip-water supersaturation, and slower drip rates, which in turn are commonly driven by changes in regional effective moisture (e.g. Fairchild et al., 2000; Wong et al., 2011; Oster et al., 2015). In the context of disequilibrium fractionation in ML-1, we note that the shifts in $\Delta\delta^{18}O$ to lower (than predicted) values at 18.0, 15.0, and 13.2 ka occur contemporaneously with the greatest disagreement between modeled $\delta^{18}O_{cc}{}^{*}$ and measured $\delta^{18}O_{cc}$ values (Fig. 7). We thus hypothesize that the observed variability in $\Delta\delta^{18}O$ values for the ML-1 record indicates that kinetic fractionation occurred during stalagmite growth driven by

lower effective moisture in the region during specific intervals of time.

4.3 Comparison to published records and model results

The observed long-term variability in ML-1 $\delta^{18}O_{fi}$ values is broadly similar to the $\delta^{18}O_{cc}$ values measured in a that observed in a stalagmite from Cave of the Bells (COB; Wagner et al., 2010), and to a lesser extent the time-series of $\delta^{18}O_{cc}$ values in a stalagmite from Fort Stanton, NM (Figs. 8 and 9). Moreover, a change-point test for the ML-1 $\delta^{18}O_{fiM}$ and COB $\delta^{18}O_{cc}$ records indicates a pronounced shift to higher values at ~15.1 ka in both records (Fig. 9). A cross wavelet analysis of the two records further documents multiple scales of statistically significant covariation on the centennial to millennial scales (Fig. 9A and B). Both the ML-1 $\delta^{2}H_{fi}$ and the Lake Elsinore leaf wax $\delta^{2}H$ records (Kirby et al., 2013; Feakins et al., 2019) demonstrate an increase to more positive values between 14 and 15 ka, similar to that observed in the leaf wax record of $\delta^{2}H$ values from Lake Elsinore (Kirby et al., (Figs. 8 and 9B). The visual comparison is confirmed by a change-point calculated for the ML-1 $\delta^{2}H_{fi}$ values that reveals this shift is statistically significant (Fig. 9D and 9F). This change in the $\delta^{2}H_{fi}$ values in the ML-1 stalagmite coincides with the first of a two-step shift to higher $\delta^{2}H$ values in the Lake Elsinore leaf wax record (Feakins et al., 2019) (Fig. 9E). These visual relationships, albeit not strong, coupled with the statistical correspondence between the records, centered around circa 15 ka, suggests that a common regional driver impacted all three records on a millennial scale and led to a major shift in regional hydroclimate around this time.

Taken as a whole, we interpret the findings of this study to indicate temporal variability in regional effective moisture including three periods of decreased effective moisture (18.0, 15.0, and 13.2 ka) and high effective moisture at 15.2 and 14.5 ka. This interpretation is in agreement with recordstwo of maximum effective moisture (15.2 and 14.5 ka) throughout the last

deglaciation. Stalagmite-independent evidence for intervals of decreased effective moisture in the US Southwest during the last deglaciation exists in several lake-level reconstructions (Lake Bonneville, Oviatt et al., 1999; Lake Chewaucan, Cohen et al., 2000; Lake Franklin, Munroe and Laabs, 2013; Lakes Jakes, Clover, and Waring, Garcia and Stokes, 2006; Lake Lahontan, Adams and Wesnousky, 1998; Lake Panamint, Smith et al., 2009; Lake Russell, Benson et al., 2003; Lake Surprise, Ibarra et al., 2014; comparisons presented in Reheis et al., 2014). A regional compilation of lake highstands in the region demonstrate that the location of highest lake levels in the US Southwest migrated from southeast to northwest over the deglaciation (McGee et al., 2018). This comparison further documents a rapid shift to decreased moisture delivery to the southern and central part of the Southwest between 16 and 15 ka (McGee et al., 2018), overlapping with the inferred major shift in regional hydroclimate archived in the stalagmite records, including on shift in the record of ML-1. This hypothesized pronounced decrease in effective moisture in the region around 15 ka is further validated by transient model simulations that indicate a reduced moisture budget in the coastal southwestern US (precipitation – evaporation (mm/d)) after 15 ka (Lora and Ibarra, 2019). We propose that the inferred decrease in effective moisture at this time is archived in all regional paleoclimate records ranging from reconstructed lake highstands and lacustrine δ^2H values (Kirby et al., 2013; Feakins et al., 2019), speleothem $\delta^{18}O_{cc}$ values (Wagner et al., 2010) as well as the δ^2H and the δ^2H_{fi} values in the ML-1 record from Lake Elsinore (Fig.), and inclusion fluid $\delta^{18}O_{fi}$ and δ^2H_{FI} records (Fig. 9B). For ML-1 specifically, the inclusion fluid isotopic values, stalagmite $\delta^{18}O_{ccc}$ and *d*-excess, $\Delta\delta^{18}O$ and cave temperatures estimated from these values further document repeated intervals of lower effective moisture in the central Sierra Nevada (18.0, 15.0, and 13.2 ka) that occurred during the turnover from the LG to HS1a (18 ka), within Heinrich 1b (15 ka), and during the warm Allerød

stadial. Intervals of inferred highest effective moisture (two pronounced at 15.2 and 14.5 ka) occurred between drier periods. The combination of these proxies and the comparison to regional records demonstrates that drying in the central Sierra Nevada did not occur at one step-change, unlike in many other records across the Southwest (i.e. McGee et al., 2018). Instead decreases in effective moisture in the central Sierra Nevada occurred in intermittent phases with periods of increased effective moisture interspersed. The difference between the regional trend in the Southwest and the record in stalagmite ML-1 may be due to the Sierra Nevada, which acts as a rain shadow in the modern climate of the Southwest (Crowley et al., 2008). Future modeling efforts with sufficient spatial resolution should be used to better understand the impact of topography on the regional drying in the Southwest.

Summary

The inclusion-fluid and calcite stable isotopic records of a stalagmite (ML-1) from the central Sierra Nevada foothills (McLean's Cave) and calculated environmentally sensitive values ($\Delta\delta^{18}O$ and *d*-excess) document repeated periods of disequilibrium calcite-water oxygen isotopic fractionation in McLean's Cave (18.0, 15.0, and 13.2 ka). Contemporaneous decreases in calculated environmentally sensitive values ($\Delta\delta^{18}O$ values and *d*-excess) argue for substantial decreases in regional effective moisture. We demonstrate the preservation of primary drip-water values, albeit evaporatively enriched in the soil, epikarst, or cave environment, in stalagmite ML-1, through petrographic and scanning analyses and by assessing a range of temperatures at which stalagmite ML-1 would be altered. We further apply the ML-1 $\delta^{18}O_{fi}$, $\delta^{2}H_{fi}$, and $\delta^{18}O_{cc}$ values to a proxy forward model (Karstolution) to document disequilibrium effects in the calcite precipitation process. To our knowledge, this is the first record of effective moisture, and its impact on in-cave fractionation, through the application of inclusion fluid isotopic measurements

and forward proxy modeling. The timing of decreased effective moisture, in one period from the ML-1 record, is contemporaneous with observed shifts in cave $\delta^{18}O_{cc}$, decreased reconstructed lake levels, and decreased lake $\delta^{2}H$ values from sites of comparable latitude range in the Southwest. The ML-1 record, however, demonstrates changes in effective moisture in three distinct phases, which suggests that effective moisture in the central Sierra Nevada is occurring in phases instead of as one step-change as is apparent throughout the Southwest.

Tables

Table 1. Notation and definitions of terms

Notation	Definition
$\delta^{18}O_{fi}$ and $\delta^{2}H_{fi}$	The $\delta^{18}O/\delta^{2}H$ values of fluid inclusions
$\delta^{18}O_{p}$ and $\delta^{2}H_{p}$	The $\delta^{18}O/\delta^{2}H$ values of precipitation
$\delta^{18}O_{cc}$	The $\delta^{18}O$ values of stalagmite calcite
$\Delta^{18}O$	Calculated difference between $\delta^{18}O_{fi}$ and $\delta^{18}O_{cc}$
$\delta^{18}O_{fiM}$	The modified $\delta^{18}O_{fi}$ value

Table 2. Inclusion δ18O and δ2H results from CRDS and TC/EA

Age (ka)	depth cm	$\delta^{18}O$	1σ	$\delta^{2}H$	1σ
11.5	0.5	-9.5	0.2	-73.8	0.8
12.9	4.3	-9.4	0.1	-77.4	1.3
13.2	4.8	-5.5	0.2	-59.9	1.9
13.2	4.8	-7.2	0.3	-70.0	1.7
13.4	5.3	-9.0	0.2	-72.5	3.6
13.4	5.3	-7.2	0.1	-64.8	2.2
13.5	5.8	-9.3	0.3	-74.4	0.8
13.8	7.8	-8.7	0.4	-73.5	0.6
13.8	*7.8*	*-8.5*	*0.5*	*-65.8*	*5.0*
13.8	8.3	-9.9	0.2	-74.5	0.5
13.9	8.8	-10.7	0.2	-79.1	1.4
14.1	9.8	-10.0	0.1	-78.5	0.5
14.1	*9.8*	*-9.1*	*0.5*	*-68.9*	*5.0*
14.5	11.0	-11.0	0.1	-88.7	0.5
14.5	*11.0*	*-10.1*	*0.5*	*-84.7*	*5.0*
14.6	11.3	-9.7	0.1	-74.5	1.6
14.6	*11.3*	*-8.7*	*0.5*	*-71.0*	*5.0*
14.7	11.8	-9.4	0.3	-75.6	0.2
14.8	11.8	-8.7	0.2	-72.1	0.9
15.0	12.3	-8.8	0.3	-78.0	1.0
15.0	12.3	-6.8	0.2	-68.9	1.4
15.2	12.8	-8.1	0.1	-72.4	0.5
15.2	12.8	-10.9	0.2	-78.7	0.7
15.2	*12.8*	*-10.7*	*0.5*	*-83.2*	*5.0*
15.4	13.0	-11.0	0.1	-82.4	0.5
16.3	13.8	-10.0	0.1	-78.4	1.0
17.1	15.3	-10.3	0.2	-77.5	0.4
17.2	16.0	-8.8	0.3	-71.5	0.9
17.5	17.3	-9.2	0.1	-71.5	0.6
17.6	17.8	-9.5	0.2	-74.4	1.1
17.7	18.3	-9.5	0.2	-75.4	1.0
17.9	18.8	-8.8	0.2	-74.8	0.9
17.9	18.8	-10.3	0.3	-76.8	2.5
18.0	19.2	-9.6	0.7	-78.9	0.4
18.0	19.2	-8.6	0.1	-74.0	0.8
18.0	*19.2*	*-6.7*	*0.5*	*-60.0*	*5.0*
18.2	19.8	-9.2	0.2	-75.9	0.6
18.2	*19.8*	*-10.6*	*0.5*	*-83.8*	*5.0*
18.9	22.0	-9.6	0.1	-74.0	1.1
19.0	*22.3*	*-9.0*	*0.5*	*-76.7*	*5.0*
19.1	*22.5*	*-9.7*	*0.5*	*-74.7*	*5.0*

**italicized indicates that the sample was measured using TCEA*

Figures

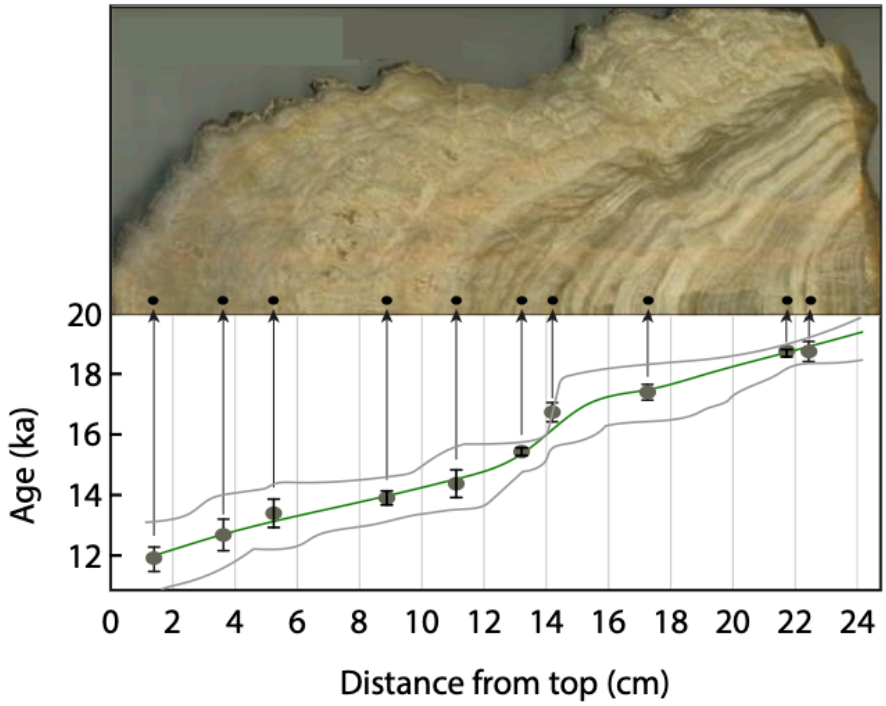

Figure 1: **U-Th calibrated age-depth model for stalagmite ML-1.** Ten U-Th ages indicate that ML-1 stalagmite (top: photograph of polished slab) exhibits relatively continuous growth between 19.4 ± 0.3 to 11.7 ± 0.4 ka. The age-depth model (green line) recalculated from Oster et al. 2015, and 95% confidence interval (gray lines) was calculated using CoPRA (Brietenbach et al., 2012). The uncertainty on the corrected age associated with the U-series dating is shown by the error bars on each value.

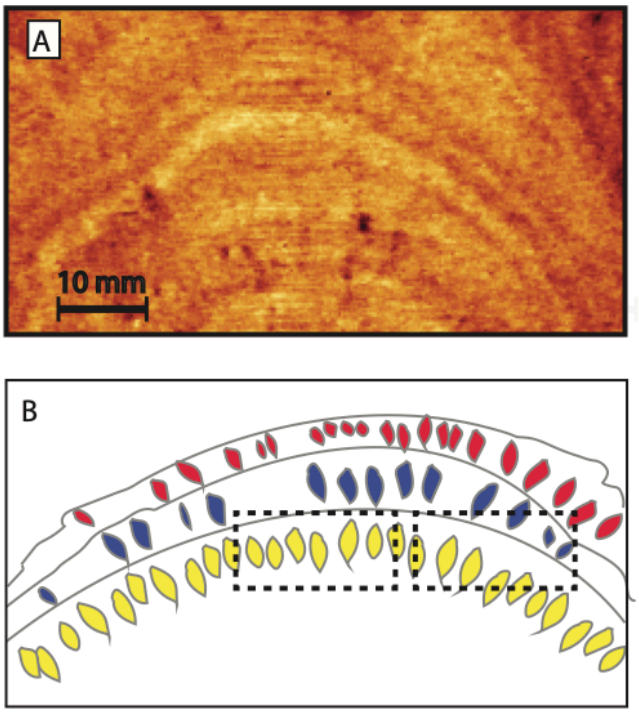

Figure 2: **Coupled NCT and XCT scan and schematic of fluid inclusion distribution in ML-1 growth bands.** (A) Coupled CT image exhibits fluid-filled inclusion-rich bands (light yellow) alternating with bands of inclusion-poor bands (darker orange; modified from Wortham et al., 2019). Photo resolution is limited by the voxel size in the scans. (B) Schematic of the fluid inclusion distribution illustrates how adjacent duplicate samples (dashed boxes) required for analytical 'replicates' can sample variable proportions of discrete generations (indicated by colors) of included fluids.

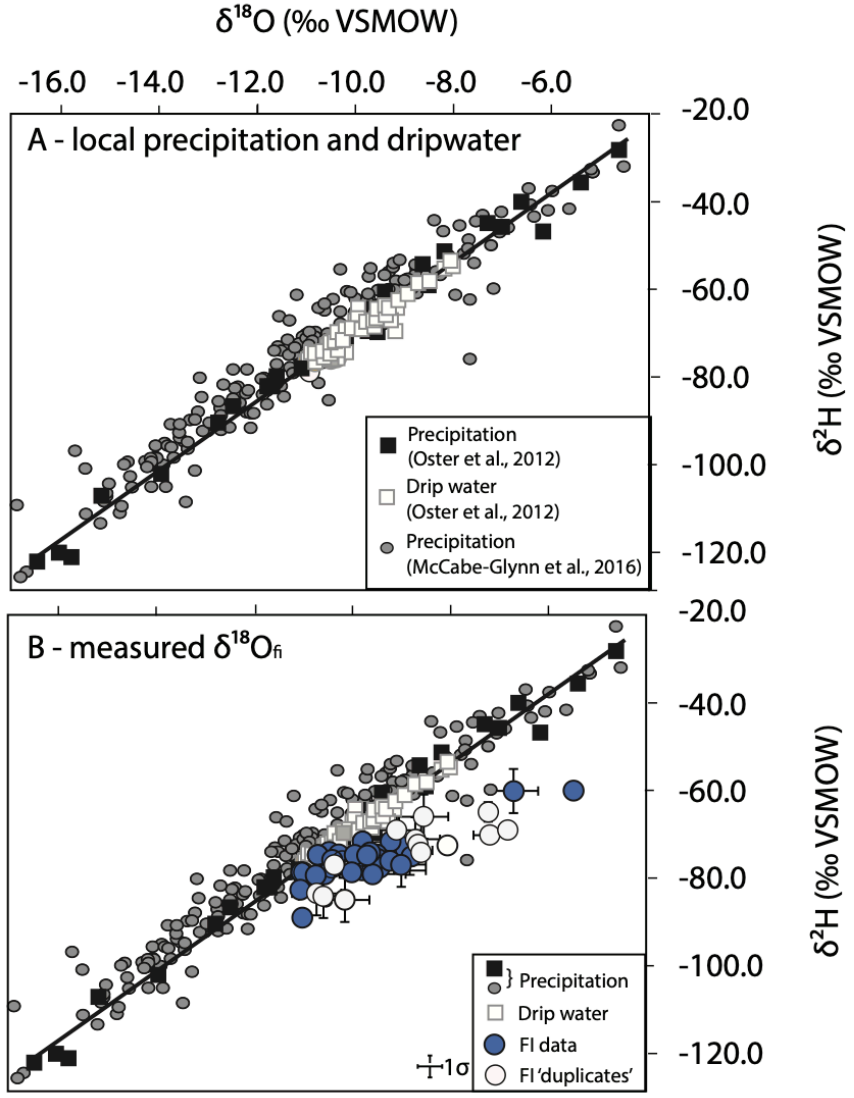

Figure 3: **Precipitation and drip-water $\delta^{18}O$ and $\delta^{2}H$ from CA and comparison to ML-1 $\delta^{18}O_{fi}$ and $\delta^{2}H_{fi}$ values.** (A) Local Meteoric Water line (black) defined using Black Chasm (~ 80 km from McLean's Cave) precipitation data (black squares; Oster et al., 2012). Measured Black Chasm (Oster et al. 2012) drip-water (white boxes) and precipitation isotopic compositions (black boxes=Black Chasm; gray circles= Sequoia National Park; elevation 1921 m (McCabe-Glynn et al., 2016;) plot along the local meteoric water line. (B) Measured (unmodified) $\delta^{18}O_{fi}$ and $\delta^{2}H_{fi}$ values for ML-1 (blue-filled circles) and duplicates (open circles) superimposed on precipitation and drip-water data.

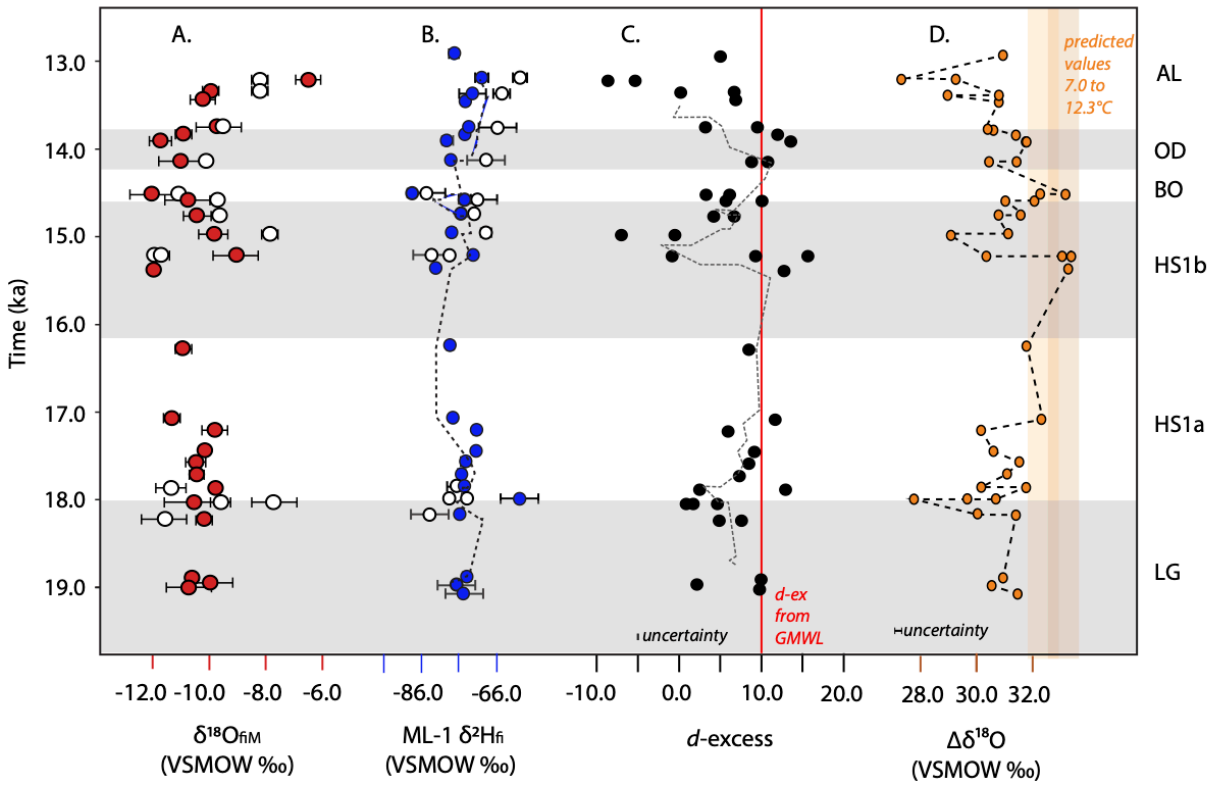

Figure 4: **Time series of inclusion-fluid isotopic compositions and calculated variables for stalagmite ML-1.** (A) The $\delta^{18}O_{fi}$ (red and white (duplicates) circles) and (B) $\delta^{2}H_{fi}$ (blue) values. Note order of magnitude scale shift between tick marks on A and B. (C) *d*-excess values (black circles) and comparison to the *d*-excess defined by the Global Meteoric Water Line (GMWL; red line). (D) Calculated $\Delta\delta^{18}O$ values based on measured $\delta^{18}O_{fi}$ values (orange circles) and the range of predicted values (orange vertical bands) defined using 7.0 and 12.3°C and the calcite-water oxygen isotope fractionation equation of Tremaine et al. (2011) (light orange) and Daeron et al. (2019) (darker orange). Time increments shown by alternating horizontal gray shading and white intervals.

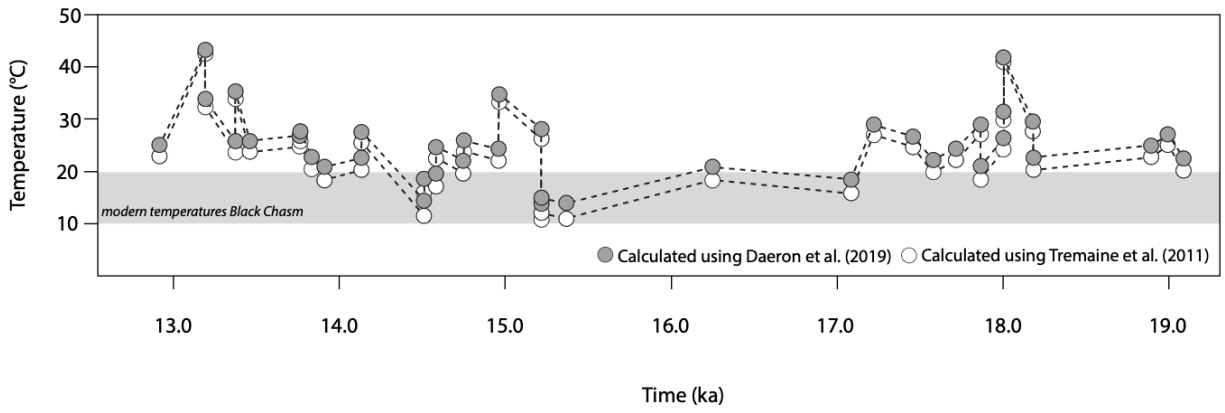

Figure 5: **Temporal trend in calculated temperatures.** Temperatures calculated using the measured $\delta^{18}O_{fi}$ and $\delta^{18}O_{cc}$ values from stalagmite ML-1 and the temperature equation of Tremaine et al. (2011) (white circles) and Daëron et al. (2019) (gray circles). The modern range in temperatures for Black Chasm (10 to 20°C) is shown by the gray bar.

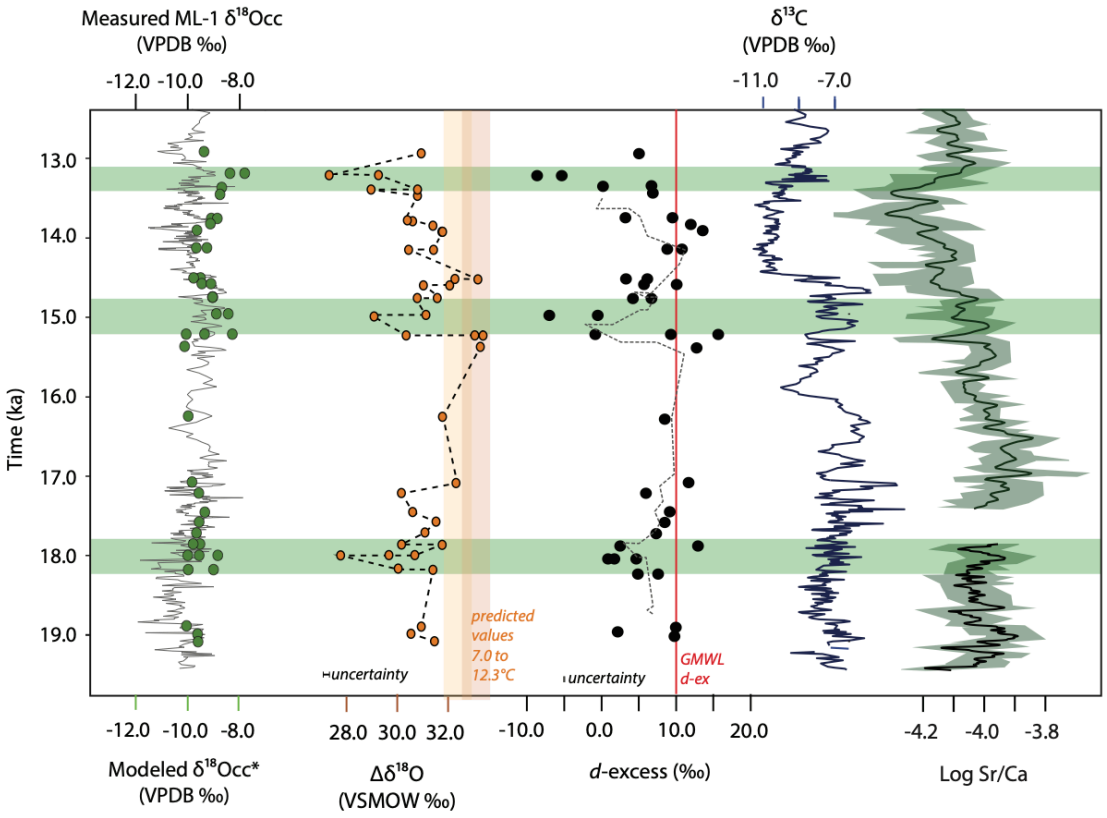

Figure 6: **Comparison of ML-1 stable isotope trends to independent proxies of effective moisture.** (Left) Measured $\delta^{18}O_{cc}$ (black line) with modeled $\delta^{18}O_{cc}$* (green dots) values superimposed. Calculated variables $\Delta\delta^{18}O$ (orange circles) and *d*-excess (black circles) are shown relative to predicted values based on equilibrium and modern conditions, respectively (see Fig. 5 for details). (Right) ML-1 $\delta^{13}C$ (blue line) values and Sr/Ca ratios time series (black line is kernel smoothing; green shading is measured variability) provided for comparison. The three periods (18.0, 15.0, and 13.2 ka) of low *d*-excess and $\Delta\delta^{18}O$ values are noted by the green shading.

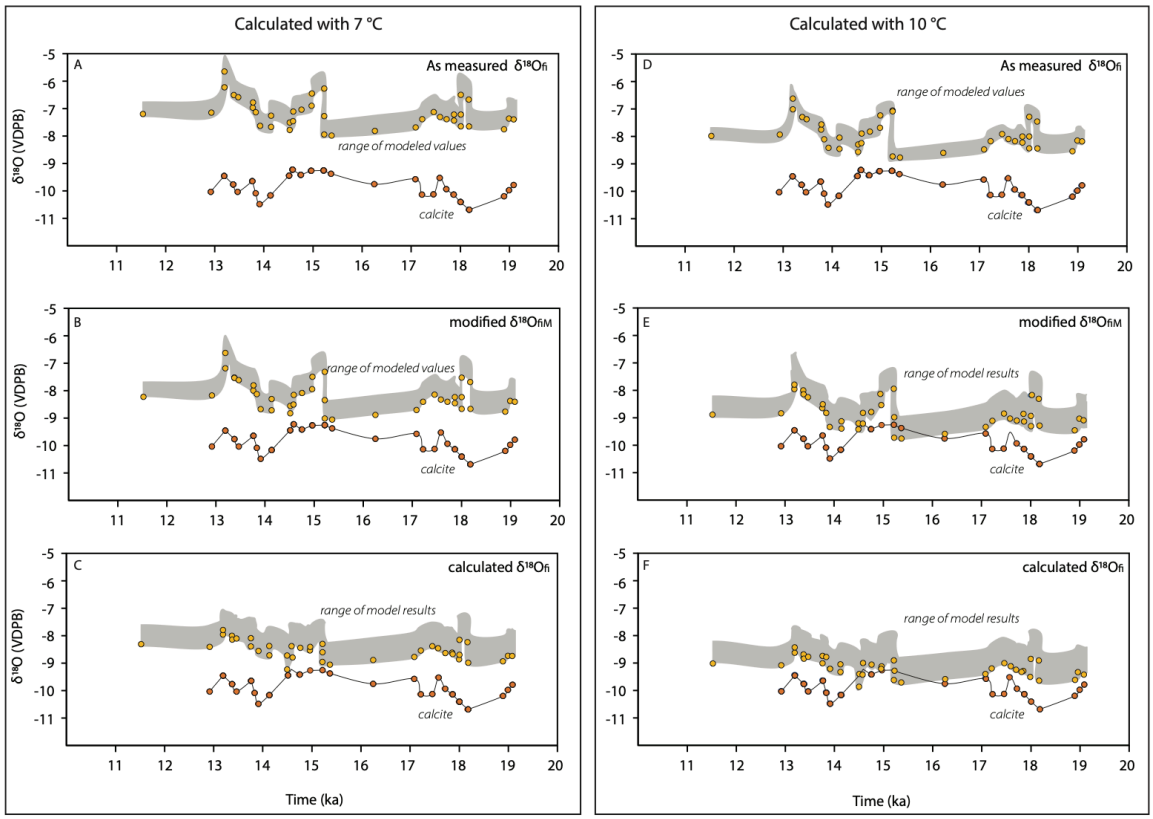

Figure 7: **Time series comparison of modeled $\delta^{18}O_{cc}$ and measured $\delta^{18}O_{cc}$ (ML-1) values.** Gray bands indicate full range of results for the Karstolution experiments. Yellow circles are experiments run using P:E ratios of 100:1. $\delta^{18}O_{cc}$ values (orange circles) are bin-averaged to the same temporal resolution as the fluid inclusion results. The experiments are parameterized with an in-cave temperature of either 7 °C (A-C) or

10 °C (D-F) and $\delta^{18}Op$ values using measured $\delta^{18}O_{fi}$ (A, D) and modified $\delta^{18}O_{fi}$ ($\delta^{18}O_{fiM}$) (B, E) values , and $\delta^{18}O_{fi}$ values that are 'calculated $\delta^{18}O_{fi}$', which is estimated using the $\delta^{2}H_{fi}$ values and the LMWL (C, F).

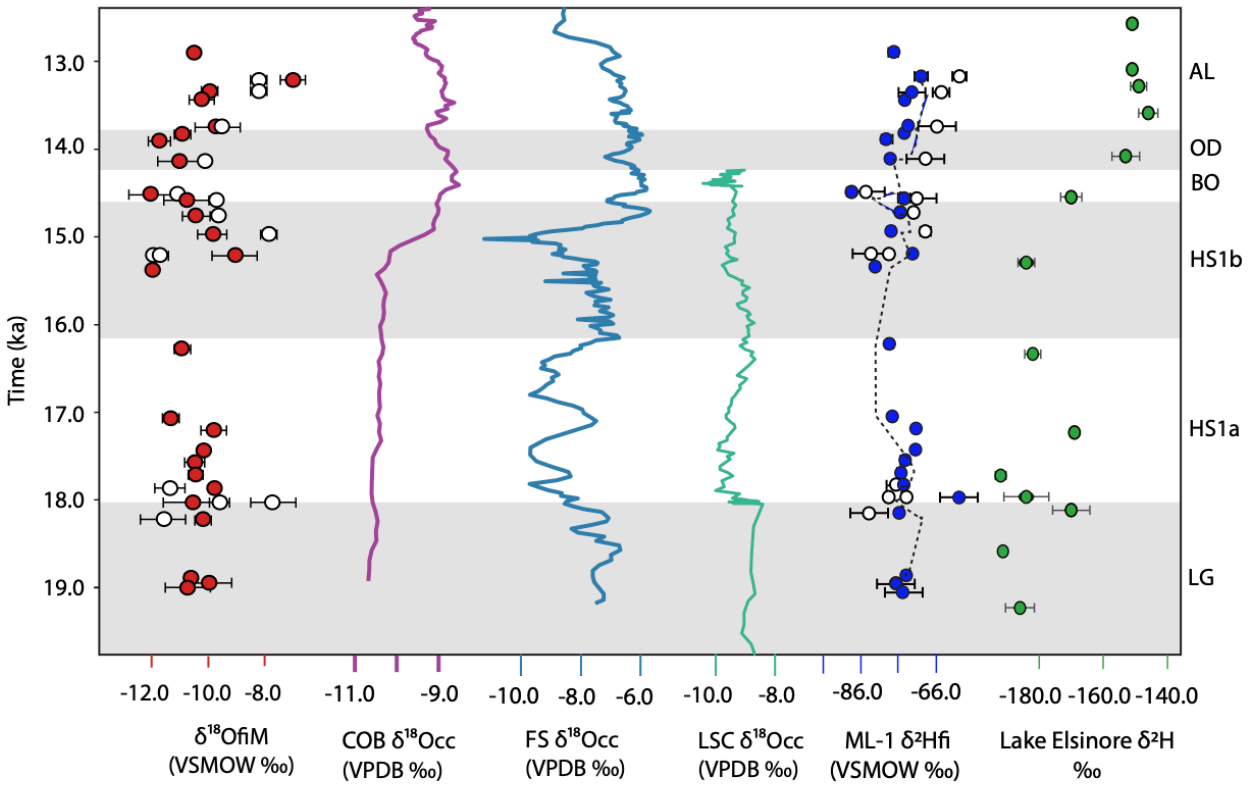

Figure 8: **$\delta^{18}O_{fiM}$ and $\delta^{2}H_{fi}$ time-series for the ML-1 stalagmite compared to published contemporaneous records.** (Left) ML-1 $\delta^{18}O_{fiM}$ values (red circles, with duplicates in white).To the right, $\delta^{18}O_{cc}$ time series for three southwestern stalagmites: purple — Cave of the Bells (COB; Wagner et al., 2010); blue — Fort Stanton (FS; Asmerom et al., 2010); green — Lake Shasta Cave (LSC; Oster et al., 2020). Second from the right: inclusion-fluid $\delta^{2}H$ time-series for ML-1 (blue circles, with duplicates in white) and Lake Elsinore leaf-wax $\delta^{2}H$ record (green circles; Kirby et al., 2013; Feakins et al., 2019). Time intervals are noted as alternating horizontal gray shading and white intervals. Uncertainty on isotopic measurements is indicated by capped lines.

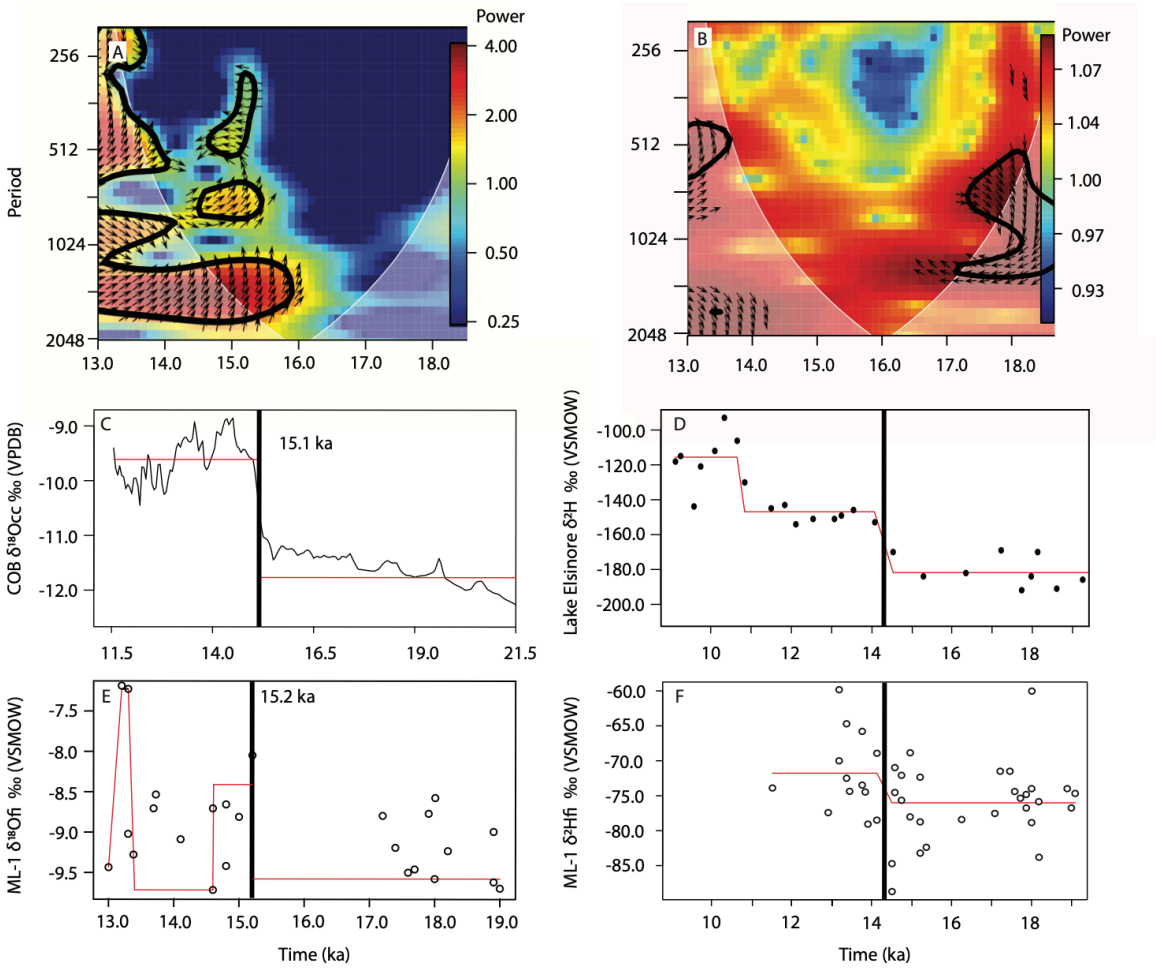

Figure 9: **Statistical tests of correspondence between the ML1 $\delta^{18}O_{fiM}$ and $\delta^{2}H_{fi}$ and published stalagmite records from the Southwest.** Cross-wavelet transforms exhibiting, by color, the power of coherency between (A) Cave of the Bells $\delta^{18}O_{cc}$ and ML-1 $\delta^{18}O_{fi}$ values, and (B) Lake Elsinore $\delta^{2}H$ and ML-1 $\delta^{2}H_{fi}$ values. Arrows indicate phase relationships (rightward pointing = in-phase, leftward pointing = out-of-phase). Warmer colors (red and orange) indicate greater synchronicity between the two data sets. Intervals of greatest correlation suggest that the change at ~15 ka is significant on both the 100- and 1000-yr scales. Change point analyses (red line) for (C) Cave of the Bells $\delta^{18}O_{cc}$ (black line), (D) Lake Elsinore $\delta^{2}H$, (E) ML-1 $\delta^{18}O_{fi}$, and (F) ML-1 $\delta^{2}H_{fi}$. Red lines in C—F indicate the 'wild binary' average through time and are generated using the R package wild binary segmentation (see Methods). Black bars are the mid-point of the change point for each record.

Citations

Affolter, S., Hauselmann, A.D., Fleitmann, D., Hauselmann, P., Leuenberger, M. 2015. Triple isotope (δD, $\delta^{17}O$, $\delta^{18}O$) study on precipitation, drip water and speleothem fluid inclusions for a Western Central European cave (NW Switzerland). *Quaternary Science Reviews*. 127: 73-89.

Affolter, S., Hauselmann, A., Fleitmann, D., Edwards, R.L., Cheng, H., Leuenberger, M. 2019. Central Europe temperature constrained by speleothem fluid inclusion water isotopes over the past 14000 years. *Science Advances*. 5(6): eaav3809.

Allen, B.D. and Anderson, R.Y. 2000. A continuous, high-resolution record of late Pleistocene climate variability from the Estancia basin, New Mexico. *GSA Bulletin*. 112(9): 1444-1458.

Anderson, L., Berkelhammer, M., Mast, M.A. 2016. Isotopes in North American Rocky Mountain Snowpack 1993-2014. *Quaternary Science Reviews*. 131(B): 262-273.

Asmerom, Y ., Polyak, V .J., Burns, S.J. 2010. V ariable winter moisture in the southwestern United States linked to rapid glacial climate shifts. *Nature geoscience*. 3: 114-117.

Asmerom, Y., Polyak, V.J., Lachniet, M. S. 2017. Extrapolar climate reversal during the last deglaciation. *Scientific Reports*. 7: 7157.

Ayalon, A., Bar-Matthews, M., Frumkin, A., Matthews, A. 2013. Last Glacial warm events on Mount Hermon: the southern extension of the Alpine karst range of the east Mediterranean. *Quaternary Science Reviews*. 59: 43-56.

Baker, A., Barnes, W.L., Smart, P.L. 1997. Variations in the discharge and organic matter content of stalagmite drip waters in Lower Cave, Bristol. *Hydrological Processes*. 11(11): 1541-1555.

Baker, A., and C. Bradley (2010), Modern stalagmite $\delta^{18}O$: Instrumental calibration and forward modelling, *Global and Planetary Change*, *71*(3-4), 201-206.

Baker, A. J., D. P. Mattey, and J. U. L. Baldini (2014), Reconstructing modern stalagmite growth from cave monitoring, local meteorology, and experimental measurements of dripwater films, *Earth and Planetary Science Letters*, *392*, 239-249.

Bar-Matthews M., Ayalon A. (2004) Speleothems as palaeoclimate indicators, a case study from Soreq Cave located in the Eastern Mediterranean Region, Israel. In: Battarbee R.W., Gasse F., Stickley C.E. (eds) Past Climate Variability through Europe and Africa. Developments in Paleoenvironmental Research, vol 6. Springer, Dordrecht. https://doi.org/10.1007/978-1-4020-2121-3_18

Benson, L., Lund, S., Negrini, R., Linsley, B., Zic, M. 2003. Response of North American Great Basin lakes to Dansgaard-Oeschger oscillations. *Quaternary Science Reviews*. 22(21-22): 2239- 2251.

Bradley, C., A. Baker, C. N. Jex, and M. J. Leng (2010), Hydrological uncertainties in the modelling of cave drip-water $\delta^{18}O$ and the implications for stalagmite palaeoclimate reconstructions, *Quaternary Science Reviews*, *29*(17-18), 2201-2214.

Bacon, S.N., Burke, R.M., Pezzopane, S.K., Jayko, A.S. 2006. Last glacial maximum and Holocene lake levels of Owens Lake, eastern California, USA. *Quanternary Science Reviews*. 25(11-12): 1264-1282.

Brietenbach, S.F.M., Rehfeld, K., Goswami, B., Baldini, J.U.L., Ridley, H.E., Kennett, D.J., Prufer, K.M., Aquino, V.V., Asmerom, Y., Polyak, V.J., Cheng, H., Kurths, J., Marwan, N. 2012 . Constructing Proxy Records from Age models (COPRA). *Clim. Past*. 8: 1765-1779.

Broecker, W. and Putnam, A.E. 2013. Hydrologic impacts of past shifts of Earth's thermal equator offer insight into those to be produced by fossil fuel CO_2. *Proc. Natl. Acad. Sci. USA* 110: 16710- 16715.

Broecker, W.S., McGee, D., Adams, K.D., Cheng, H., Edwards, R.L., Oviatt, C.G., Quade, J. 2009. A Great Basin-wide dry episode during the first half of the Mystery Interval? *Quaternary Science Reviews*. 28(25-26): 2557-2563.

Carlson, P.E., Noronha, A.L., Banner, J.L., Jenson, J.W., Moore, M.W., Partin, J.W., Deininger, M., Breecker, D.O., Bautista, K.K. 2020. *Geochimica et Cosmochimica Acta*. 284: 222-238.

Clark, I.D., & Fritz, P. (1997). Environmental Isotopes in Hydrogeology (1st ed.). CRC Press. https://doi.org/10.1201/9781482242911

Daeron, M., Drysdale, R.N., Peral, M., Huyghe, D., Blamart, D., Coplen, T.B., Lartaud, F., Zanchetta, G. 2019. Most Earth-surface calcites precipitate out of isotopic equilibrium. *Nature Comms*. 10: 429.

Dassie, E.P., Genty, D., Noret, A., Mengenot, X., Massault, M., Lebas, N., Duhamel, M., Bonifacie, M., Gasparrini, M., Minster, B., Michelot, J.-L. 2018. A newly designed analytical line to examine fluid inclusion isotopic compositions in a variety of carbonate samples. *Geochemistry, Geophysics, Geosystems*. 19(4): 1107-1122.

De Graaf, S., Vonhof, H.B., Weissbach, T., Wassenburg, J.A., Levy, E.J., Kluge, T., Haug, G.H. 2020. A comparison of isotope ratio mass spectrometry and cavity ring-down spectroscopy techniques for isotope analysis of fluid inclusion water. *Rapid Communications in Mass Spectormetry*. 34(16): e8837.

Deininger, M., & Scholz, D. (2019). ISOLUTION 1.0: an ISOtope evoLUTION model describing the stable oxygen (δ18O) and carbon (δ13C) isotope values of speleothems. *International Journal of Speleology, 48*, 3. doi:https://doi.org/10.5038/1827-806X.48.1.2219

Demeny, A., Czuppon, G., Kern, Z., Leel-Ossy, S., Nemeth, A., Szabo, M., Toth, M., Wu, C.-C., Shen, C.-C., Molnar, M., Nemeth, T., Nemeth, P., Ovari, M. 2016. Recrystallization-induced oxygen isotope changes in inclusion-hosted water of speleothems- Paleoclimatological implications. *Quaternary International*. 415: 25-32.

Dreybrodt, W., and M. Deininger (2014), The impact of evaporation to the isotope composition of DIC in calcite precipitating water films in equilibrium and kinetic fractionation models, *Geochimica et Cosmochimica Acta*, *125*, 433-439.

I.J. Fairchild, A. Borsato, A.F. Tooth, S. Frisia, C.J. Hawkesworth, Y. Huang, F. McDermott, B. Sprio. 2000. Controls on trace element (Sr-Mg) compositions of carbonate cave waters: implications for speleothem climatic records Chem. Geol., 166: 255-269

Feakins, S.J., Wu, M.S., Ponton, C., Tierney, J.E. 2019. Biomarkers reveal abrupt switches in hydroclimate during the last glacial in southern California. *Earth and Planetary Science Letters*. 515: 164-172.

Fryzlewicz, P. 2014. Wild binary segmentation for multiple change-point detection. *Ann. Statist.* 42(6): 2243-2281.

Genty, D., Baker, A., Vokal, B. 2001. Intra- and inter-annual growth rate of modern stalagmites. *Chemical Geology*. 176: 191-212.

Gouhier, T.C., Grinsted, A., Simko, V. (2019). R package biwavelet: Conduct univariate and bivariate wavelet analyses (Version 0.20.19). Available from https://github.com/tgouhier/biwavelet

Griffiths, M.L., Drysdale, R.N., Vonhof, H.B., Gagan, M.K., Zhao, J.-x., Ayliffe, L.K., Hantoro, W.S., Hellstrom, J.C., Cartwright, I., Frisia, S., Suwargadi, B.W. 2010. Younger Dryas-Holocene temperature and rainfall history of southern Indonesia from d18O in speleothem calcite and fluid inclusions. *Earth and Planetary Science Letters*. 295: 30-36.

Harmon, R.S., Schwarcz, H.P., O'Neil, J.R. 1979. D/H ratios in speleothem fluid inclusions: A guide to variations in the isotopic composition of meteoric precipitation? *Earth and Planetary Science Letters*. 42: 254-266.

Hendy, C.H. 1971. The isotopic geochemistry of speleothems-I. The calculation of the effects of different modes of formation on the isotopic composition of speleothem and their applicability as paleoclimatic indicators. *Geochimica et Cosmochimica Acta*. 35(8): 801-824.

Hudson, A.M., Hatchett, B.J., Quade, J., Boyle, D.P., Bassett, S.D., Ali, G., Marie, G. 2019. North-south dipole in winter hydroclimate in the western United States during the last deglaciation. *Scientific Reports*. 9(1): 1-12.

Kirby, M.E., Feakins, S.J., Bonuso, N., Fantozzi, J.M., Hiner, C.A. 2013. Latest Pleistocene to Holocene hydroclimates from Lake Elsinore, California. *Quaternary Science Reviews*. 76: 1-15.

Kirby, M.E., Feakins, S.J., Hiner, C.A., Fantozzi, J, Zimmerman, S.R.H., Dingemans, T., Mensing, S. 2014. Tropical Pacific forcing of Late-Holocene hydrologic variability in the coastal southwest United States. *Quaternary Science Reviews*. 102: 27–38.

Kluge, T., Affek, H.P. 2012. Quantifying kinetic fractionation in Bunker Cave speleothems using Δ_{47}. *Quaternary Science Reviews*. 49: 82-94.

Labuhn, I., Genty, D., Vonhof, H., Bourdin, C., Blamart, D., Douville, E., Ruan, J., Cheng, H., Edwards, R.L., Pons-Branchu, E., Pierre, M. 2015. A high-resolution fluid inclusion d18O record from a stalagmite in SW France: modern calibration and comparison with multiple proxies. *Quaternary Science Reviews*. 110: 152-265.

Lachniet, M.S. 2009. Climatic and environmental controls on speleothem oxygen-isotope values. *Quaternary Science Reviews*. 28: 412-432.

Lachniet, M.S., Denniston, R.F., Asmerom, Y., and Polyak, V.J. 2014. Orbital control of western North America atmospheric circulation and climate over two glacial cycles. *Nature Comm*. 5: 3805

Lachniet, M.S. 2016. A speleothem record of Great Basin paleoclimate: The Leviathan chronology, Nevada, Chapter 20. *In* Shroder, J.F., Jr., Ed., Lake Bonneville: A Scientific Update, *Developments In Earth Surface Processes*. 20: 551-569.

McCabe-Glynn, S., Johnson, K, Strong, C., Zou, Y., Yu, J.-Y., Sellars, S., Welker, J.M. 2016. Isotopic signature of extreme precipitation events in the western U.S. and associated phases of Arctic and tropical climate modes. *Journal of Geophysical Research: Atmospheres*. 121(15): 8913- 8924.

Matthews, A., Ayalon, A., Bar-Matthews, M. 2000. D/H ratios of fluid inclusions of Soreq cave (Israel) speleothem as a guide to the Eastern Mediterranean meteoric line relationships in the last 120 ky. *Chemical Geology*. 166 (3-4): 183-191.

McDermott, F. 2004. Palaeo-climate reconstruction from stable isotope variations in speleothems: a review. *Quaternary Science Reviews*. 23(7-8): 908-918.

McGarry, S., Bar-Matthews, M., Matthews, A., Vaks, A., Schilman, B., Ayalon, A. 2004. Constraints on hydrological and paleotemperature variations in the Eastern Mediterannean region in the last 140 ka given by the dD values of speleothem fluid inclusions. *Quaternary Science Reviews* 23(7-8): 919-934.

McGee, D., Quade, J., Edwards, R.L., Broecker, W.S., Cheng, H., Reiners, P.W., Evenson, N. 2012. Lacustrine cave carbonates: novel archives of paleohydrologic change in the Bonneville Basin (Utah, USA). *Earth and Planetary Science Letters*. 351-352: 182-194.

Meckler, A.N., Affolter, S., Dublyansky, Y.V., Kruger, Y., Vogel, N., Bernasconi, S.M., Frenz, M., Kipfer, R., Leuenberger, M., Spotl, C. 2015. Glacial-interglacial temperature change in the tropical West Pacific: a comparison of stalagmite-based paleo-thermometers. *Quaternary Science Reviews*. 127: 90-116.

Mickler, P.J., Banner, J.L., Stern, L., Asmerom Y., Edwards, R.L., Ito, E. 2004. Stable isotope variations in modern tropical speleothem: evaluating equilibrium vs. kinetic isotope effects. *Geochimica et Cosmochimica Acta*. 68:4381-4393.

Millo, C., Strikis, N.M., Vonhof, H.B., Deininger, M., Cruz, F.W., Wang, X., Cheng, H., Edwards, R.L. 2017. Last glacial and Holocene stable isotope record of fossil dripwater from subtropical Brazil based on analysis of fluid inclusions in stalagmites. *Chemical Geology*. 468: 84-96.

Moreno, A., Sancho, C., Barolome, M., Oliva-Urcia, B., Delgado-Huertas, A., Estrela, M. J., Corell, D., Lopez-Moreno, J.I., Cacho, I. 2014. Climate controls on rainfall isotopes and their effects on cave drip water and speleothem growth: the case of Molinos cave (Teruel, NE Spain). *Clim. Dyn*. 43: 221-241.

Onac, B.P., Pace- Graczyk, K., Atudirei, V. 2008. Stable isotope study of precipitation and cave drip water in Florida (USA): implications for speleothem based paleoclimate studies. Isotopes in Environmental and Health Studies. 44(2): 149-161.

Oster, J.L., Montanez, I.P., Santare, L.R., Sharp, W.D., Wong, C., Cooper, K.M. 2015. Stalagmite records of hydroclimate in central California during termination 1. *Quaternary Science Reviews*. 127: 199-214.

Oster, J.L., Montanez, I.P., Mertz-Kraus, R., Sharp, W.D., Stock, G.M., Spero, H.J., Tinsley, J., Zachos, J.C. 2014. Millennial-scale variations in western Sierra Nevada precipitation during the last glacial cycle MIS 4/3 transition. *Quaternary Research*. 82(1): 236-248.

Oster, J.L., Weisman, I.E., Sharp, W.D. 2020. Multi-proxy stalagmite records from northern California reveal dynamic patterns of regional hydroclimate over the last glacial cycle. *Quaternary Science Reviews*. 241: 106411.

Owen, L.A., Finkel, R.C., Minnich, R.A., Perez, A.E. 2003. Extreme southwestern margin of late Quaternary glaciation in North America: timing and controls. *Geology*. 31(8): 729-732.

Polk, J.S., van Beynen, P., Wynn, J. 2012. An isotopic calibration study of precipitation, cave dripwater, and climate in west-central Florida. *Hydrological Processes*. 26(5): 652-662.

Quade, J. and Broecker, W.S. 2009. Dryland hydrology in a warmer world: Lessons from the Last Glacial period. *The European Physical Journal Special Topics*. 176(1): 21-36.

Reynard, L.M., Day, C.C., Henderson, G.M. 2011. Large fractionation of calcium isotopes during cave-analogue calcium carbonate growth. *Geochimica et Cosmochimica Acta*. 75(13): 3726-3740.

K. Rozanski, L. Araguas-Araguas, R. Gonfiantini. 1993. Isotopic patterns in modern global precipitation. P.K. Swart, K.C. Lohman, J. McKenzie, S. Savin (Eds.), Climate Change in

Continental Isotopic Records, Geophysical Monograph, vol. 78, American Geophysical Union, Washington, DC. 1-36.

Santare, L.R. 2013. A multi-proxy stalagmite reconstruction of climate in the central Sierra Nevada during the last deglaciation. University of California, Davis Thesis. 1548292.

Santi, L.M., Arnold, A.J., Ibarra, D.E., Whicker, C.A., Mering, J.A., Lomarda, R.B., Lora, J.M., Tripati, A. 2020. Clumped isotope constraints on changes in latest Pleistocene hydroclimate in the northwestern Great Basin: Lake Surprise, California. *GSA Bulletin*. 132(11-12): 2669-2683.

Schwarcz, H.P., Harmon, R.S. Thompson, P., Ford, D.C. 1976. Stable isotope studies of fluid inclusions in speleothems and their paleoclimate significance. *Geochimica et Cosmochimica Acta*. 40(6):657-665

Street, J.H., Anderson, R.S., Paytan, A. 2012. An organic geochemical record of Sierra Nevada climate since the LGM from Swamp Lake, Yosemite. *Quaternary Science Reviews*. 40: 89-106.

Treble, P., Mah, M., Griffiths, A.D., Baker, A., Deininger, M., Kelly, B., Scholz, D., Hankin, S. 2019. Separating isotopic impacts of karst and in-cave processes from climate variability using an integrated speleothem isotope-enabled forward model. *Earth ArXiv*.

Tremaine, D.M., Froelich, P.N., Wang, Y. 2011. Speleothem calcite farmed *in situ*: modern calibration of $\delta^{18}O$ and $\delta^{13}C$ paleoclimate proxies in a continuously-monitored natural cave system. *Geochimica et Cosmochimica Acta*. 75(17): 4929-4950.

Vonhof, H.B., van Breukelen, M.R., Pstma, O., Rowe, P.J., Atkinson, T.C., Kroon, D. 2006. A continuous-flow crushing device for on-line d2H analysis of fluid inclusion water in speleothems. *Rapid communications in Mass Spectrometry*. 20(17): 2553-2558.

Wagner, J.D.M., Cole, J.E., Beck, J.W., Patchett, P.J., Henderson, G.M., Barnet, H.R. 2010. Moisture variability in the southwestern United States linked to abrupt glacial climate change. *Nature geoscience*. 3:110-113.

J.M. Watkins, L.C. Nielsen, F.J. Ryerson, D.J. DePaolo. 2013. The influence of kinetics on the oxygen isotope composition of calcium carbonate. Earth Planet. Sci. Lett., 375: 349-360

Watkins, J.M., Hunt, J.D., Ryerson, F.J., DePaulo, D.J. 2013. The influence of temperature, pH, and growth rate on the d18O composition of inorganically precipitated calcite. *Earth and Planetary Science Letters*. 404: 332-343.

Wong, C.I., Banner, J.L., Musgrove, M. 2011. Seasonal dripwater Mg/Ca and Sr/Ca variations driven by cave ventilation: implications for and modeling of speleothem paleoclimate records. *Geochimica et Cosmochimica Acta*. 75(12): 3514-3529.

Western Regional Climate Center. Evaporation Stations: California, New Melones Dam. Accessed on Aug. 31, 2019. https://wrcc.dri.edu/Climate/comp_table_show.php?stype=pan_evap_avg

Supplementary Material

A record of effective moisture using $\delta^{18}O$ and $\delta^{2}H$ of stalagmite inclusions from the central Sierra Nevada, CA.

Introduction

Here we present additional figures and tables to describe modifications to the devise used to measure the $\delta^{18}O_{fi}$ values and the interpretations the Karstolution results.

Methodology

Changes to the original design of the Miami Deice were made in order to improve the sensitivity and to eliminate possible contaminations from organic molecules present in the fluid inclusions.

Improvements in Sensitivity: In the original 'Miami' device described by Arienzo et al. (2013), the minimum amount of water, needed to produce reliable $\delta^{18}O$ and $\delta^{2}H$ values was approximately 2 ul. For many samples this necessitated an amount of carbonate material that was physically too large for the dimension of the crusher. In order to produce a more sensitive system, we eliminated the expansion chamber in the original design and instead allowed the gas in nitrogen carrier stream to deliver the H_2O from the crusher directly to the CRDS. This system produces a signal similar to that observed using a gas chromatograph connected to a conventional isotope ratio mass spectrometer, with the isotope ratios of the species being determined by integrating the areas producing from the signals on the minor and major isotopes of oxygen and hydrogen. This allowed the amount of water to be reduced by approximately an order of magnitude.

A typical sample trace is shown in Supp. Fig. 2. A weighted average $\delta^{18}O$ and $\delta^{2}H$ value was calculated every second for signals yielding H_2O concentrations greater than 500 ppm. We tested this new method by analyzing the injections of two standard waters (LS3 and OH-16) and one standard rock (Scladina) >20 times before beginning analysis (Supp. Table 1). Additionally, two stalagmite samples that are treated as standards (Arienzo et al., 2013) analyzed as unknowns 18 times over the course of the analyses (Supp. Table 2). Injections of standard waters ranged from 0.2 to 1.0 μL. At the beginning of each day of analyses standard waters were measured three times to begin the day, five times in a range of sizes to understand the daily change in size effect, and six times (three times for OH-16 and LS3, respectively) to understand the daily change in memory effect. Finally, three analyses of LS3 were performed before and after each sample crush when an unknown was being analyzed.

Removal of Organic Contamination: It is well established that trace amounts of organic molecules can lead to erroneous $\delta^{18}O$ values in water extracted from plant materials (Ref). Such organic material can be eliminated by passing the sample over a platinum catalysts held at ~ 400°C. Such a catalyst can be coiled platinum wire or material taken from the catalytic converter of a motor vehicle. Although this produces a small amount of H_2O, its effect on the $\delta^{18}O$ of the H_2O samples is minimal (ref). The addition of such as

catalytic converter to the 'Miami Device' was deemed necessary after analyses without the catalyst led to an extremely high variability between duplicates.

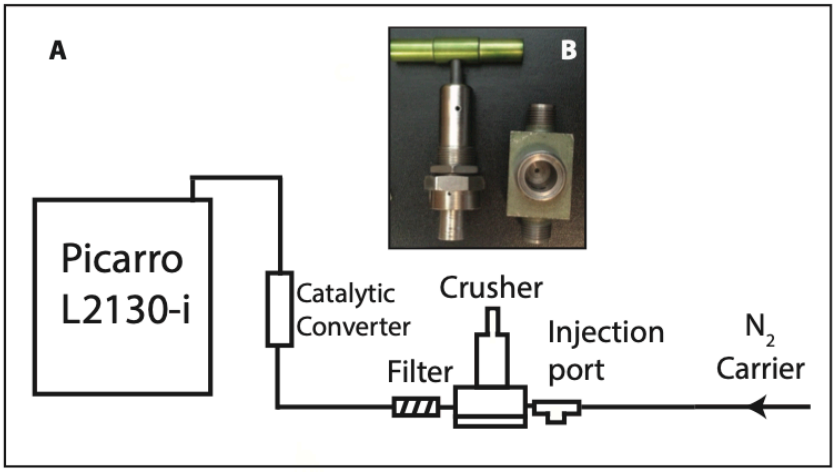

Supp. Fig. 1: **Schematic of the modified 'Miami Device' (diagram modified after Arienzo et al., 2013) for extraction and measurement of inclusion fluids.** (A) Stalagmite chips are crushed in a modified Swagelok valve (B) to release trapped water, which in turn is carried by N_2 gas through the extraction line and measured on a Picarro L2130-i Cavity Ring Down spectrometer. The catalytic converter was added between the crusher and the CRDS to reduce potential variability of fluid isotopic values due to dissolved organics.

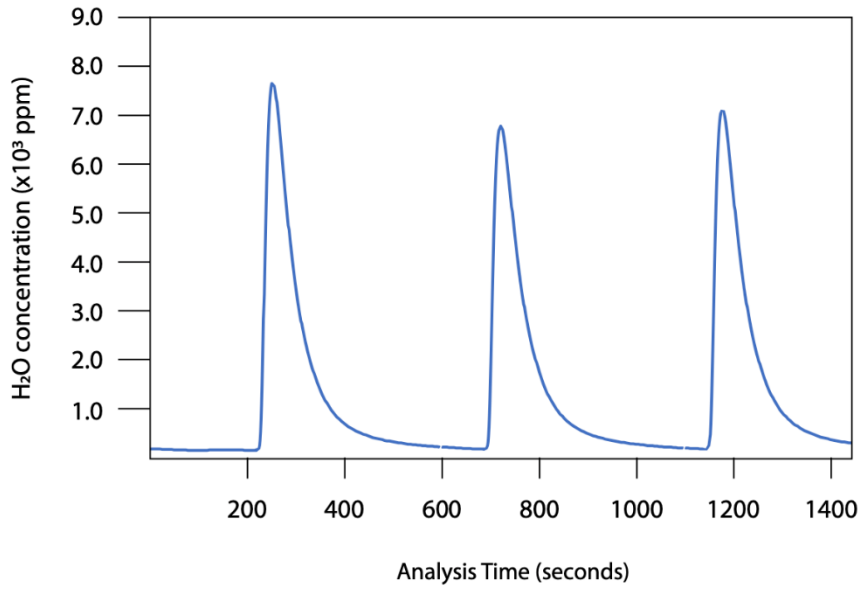

Supp. Fig. 2. A typical analysis curve of analysis time in seconds vs. the concentration of H_2O in ppm for the CRDS. Each analysis had a pulse of H_2O move through the CRDS. Stable isotope values were derived by taking the weighted average of the $\delta^{18}O$ values below the curves shown here.

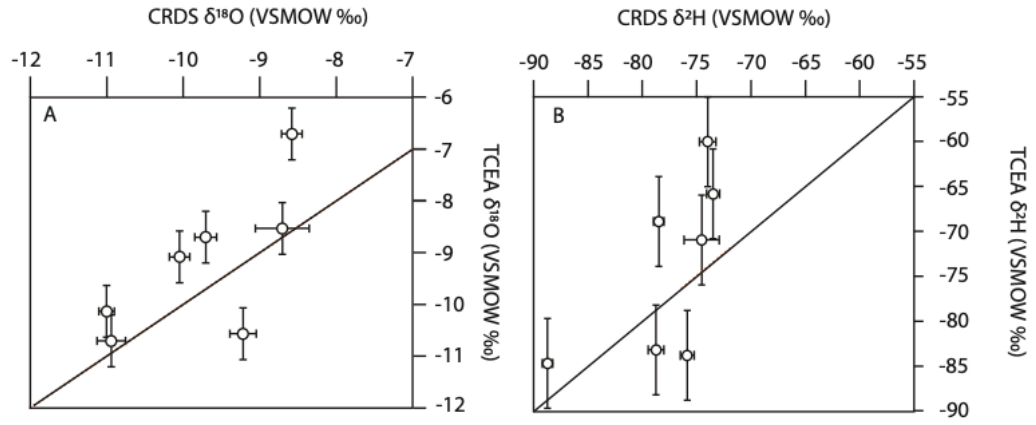

Supp Fig. 3: **Comparison of duplicate inclusion values measured with TC-EA and CRDS.** (A) $\delta^{18}O_{fi}$ values and B) $\delta^{2}H_{fi}$ values of samples measured by both CRDS and TCEA in VSMOW. Black lines indicate a y = x relationship of 1, error bars represent 1σ uncertainty.

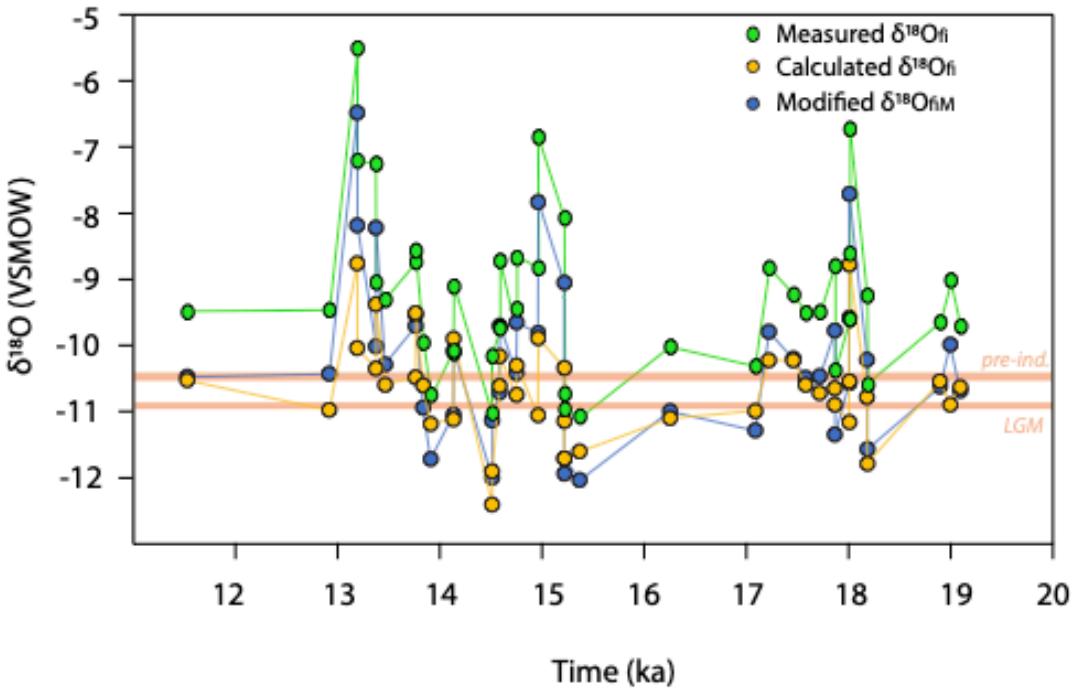

Supp. Fig. 4: **Time series of inclusion results as compared to the 'fully-tuned' Karstolution model.** Calculated $\delta^{18}O_{fi}$ (yellow), modified $\delta^{18}O_{fiM}$ (blue) values are comparable in range of data, and the as measured $\delta^{18}O_{fi}$ values (green) are higher. The orange bars represent simulated drip-water $\delta^{18}O$ using Karstolution forced with 45 years of iCESM1.3 output from the LGM (bottom orange bar) and the pre-industrial (top orange bar). The range of dripwater $\delta^{18}O$ results from the Karstolution runs are indicated by the thickness of the bar.

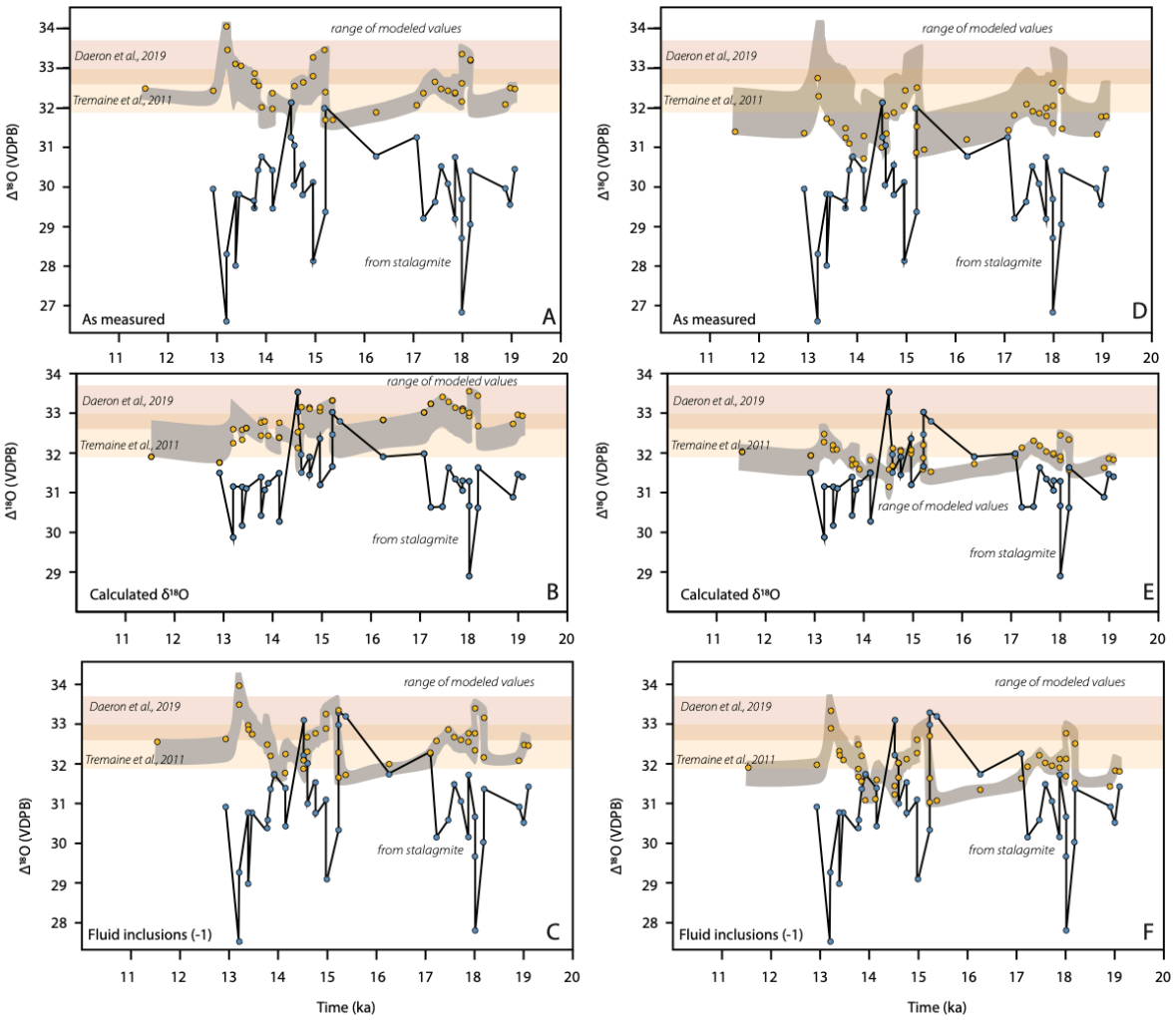

Supp. Fig. 5: Time series of $\Delta\delta^{18}O$ calculated using Karstolution results vs $\Delta\delta^{18}O$ calculated using the measured inclusion fluid and calcite $\delta^{18}O$ values. The Karstolution $\Delta\delta^{18}O$ values presented here are calculated using the simulated dripwater $\delta^{18}O$ and the simulated calcite $\delta^{18}O$ from the Karstolution results. The range of Karstolution results are indicated by the gray band; yellow circles are values based on one Karstolution experiment using a P:E ratio of 100:1. $\Delta\delta^{18}O$ calculations from the inclusion values are noted with blue circles. Calculated values for $\Delta\delta^{18}O$ used the equations of Daëron et al. (2019) (orange bar) and Tremaine et al. (2011) (yellow bar) and 7 and 10 °C. T An in-cave temperature of 7°C (A-C) or 10°C (D-F) was used as input for Karstolution. The comparisons are best when using the modified and calculated $\delta^{18}O_{fi}$ values.

Supp. Table 1 Standardization runs for new method

Run #	Name	Size	$\delta^{18}O$	$\delta^{2}H$
1	LS3	0.5 uL	-10.7	-89.7
2	LS3	0.5 uL	-10.9	-89.3
3	LS3	0.5 uL	-11.0	-89.5
4	LS3	0.5 uL	-10.8	-88.8
5	LS3	0.2 uL	-10.4	-88.9
6	LS3	0.4 uL	-10.6	-89.0
7	LS3	0.6 uL	-11.1	-89.2
8	LS3	0.8 uL	-11.2	-89.9
9	LS3	1.0 uL	-11.2	-90.0
10	OH-16	0.5 uL	-14.8	-110.8
11	OH-16	0.5 uL	-15.3	-117.9
12	OH-16	0.5 uL	-15.0	-119.9
13	OH-16	0.2 uL	-14.3	-116.7
14	OH-16	0.4 uL	-15.3	-121.9
15	OH-16	0.6 uL	-16.0	-125.2
16	OH-16	0.8 uL	-16.3	-127.9
17	OH-16	1.0 uL	-16.6	-130.3
18	Scladina		-10.5	-82.7
19	Scladina		-10.7	-83.3
20	LS3	0.5 uL	-10.3	-83.0
21	LS3	0.5 uL	-10.2	-82.8
22	LS3	0.5 uL	-10.6	-89.5
23	LS3	0.5 uL	-10.5	-88.7
24	LS3	0.5 uL	-10.7	-88.8

Supp.Table 2. Standards analyzed as unknowns

Standard Name	Date analyzed	$\delta^{18}O$ ‰ VSMOW	$\delta^{2}H$ ‰ VSMOW
HBC-F	11/18/19	-5.89	-51.17
HBC-F	11/18/19	-5.42	-41.67
HBC-F	11/18/19	-5.03	-37.50
HBC-F	11/19/19	-6.52	-50.79
HBC-F	11/20/19	-6.61	-43.94
HBC-F	12/3/19	-7.19	-50.61
average		*-6.11*	*-45.95*
standard deviation		*0.81*	*5.76*
Standard Name	Date analyzed	$\delta^{18}O$ ‰ VSMOW	$\delta^{2}H$ ‰ VSMOW
Huagapo	11/15/19	-15.03	-112.47
Huagapo	11/15/19	-15.35	-99.62
Huagapo	11/18/19	-14.33	-97.46
Huagapo	11/18/19	-14.60	-94.67
Huagapo	11/18/19	-13.96	-102.21
Huagapo	11/18/19	-13.81	-101.55
Huagapo	11/21/19	-15.18	-110.48
Huagapo	12/5/19	-11.87	-95.52
Huagapo	11/22/19	-12.91	-84.60
Huagapo	12/4/19	-12.38	-106.75
Huagapo	12/6/19	-13.37	-100.40
average		*-13.89*	*-100.52*
standard deviation		*1.16*	*7.79*